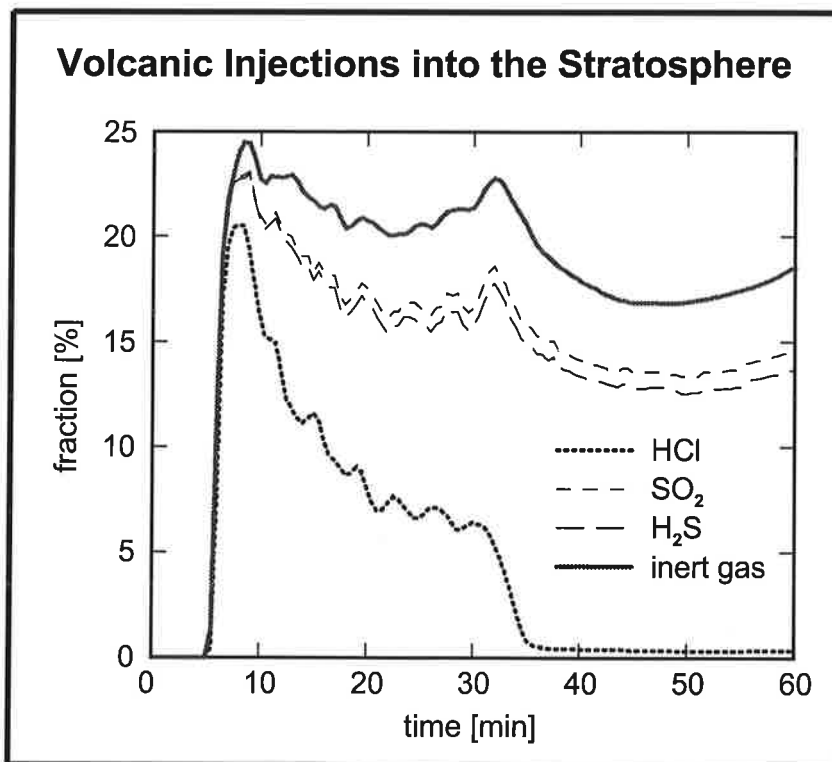




Max-Planck-Institut für Meteorologie

EXAMENSARBEIT Nr. 65



NUMERICAL SIMULATION OF SCAVENGING PROCESSES IN EXPLOSIVE VOLCANIC ERUPTION CLOUDS

von
Christiane Textor

HAMBURG, Juli 1999

Dissertation zur Erlangung des Doktorgrades

Autorin:

Christiane Textor

Max-Planck-Institut
für Meteorologie

MAX-PLANCK-INSTITUT
FÜR METEOROLOGIE
BUNDESSTRASSE 55
D - 20146 HAMBURG
GERMANY

Tel.: +49-(0)40-4 11 73-0
Telefax: +49-(0)40-4 11 73-298
E-Mail: <name> @ dkrz.de

**Numerical Simulation
of Scavenging Processes in Explosive
Volcanic Eruption Clouds**

Dissertation
zur Erlangung des Doktorgrades
der Naturwissenschaften
im Fachbereich Geowissenschaften
der Universität Hamburg

vorgelegt von

Christiane Textor
aus Kassel

Hamburg

1999

ISSN 0938 - 5177

Als Dissertation angenommen vom Fachbereich Geowissenschaften
der Universität Hamburg

aufgrund der Gutachten von Herrn Prof. Dr. H.Graßl
und Herrn Priv. Doz. Dr. H.-F. Graf

Hamburg, den 13. 07.1999

Prof. Dr. J.O. Backhaus
Prodekan des Fachbereichs Geowissenschaften

Abstract

The scavenging of gases and particles in an explosive volcanic eruption plume has been studied by numerical simulations with the plume model ATHAM (Active Tracer High Resolution Atmospheric Model). We identified relevant factors that determine the fraction of volcanic material eventually being injected into the stratosphere. An extended version of the microphysics has been formulated: predicting both the specific mass content and the number concentration it describes the interaction of hydrometeors and volcanic ash in the plume, which leads to particle growth and efficient sedimentation. In addition, we developed a module for the calculation of volcanic gas scavenging by liquid and solid hydrometeors in the plume.

This study reveals the dominant role of hydrometeors in controlling many processes in the plume. The coating of volcanic ash with liquid water or ice results in highly efficient growth of particles, which strongly enhances the fallout velocity of ash. Precipitation of aggregates results in efficient gas-particle separation, which increases the injection of volcanic gases into the stratosphere. In addition, it strongly influences the stream pattern, which in turn influences the microphysics in the plume by lowering the supersaturation in the ascent zone. By far the highest portion of condensed water freezes to ice in the eruption column. The fast plume rise to regions, which are too cold for even supercooled liquid water to exist causes most particles to occur as ice-ash aggregates.

We examined the scavenging of the most important volcanic gases, HCl, SO₂ and H₂S, by liquid and solid hydrometeors and by aggregates in the plume. The scavenging efficiency is determined by the amount of condensed water or ice. HCl is almost completely removed from the gas phase by dissolution in liquid water occurring in the lower central plume. These ash-containing drops quickly freeze to graupel aggregates that precipitate efficiently, thus also removing HCl from higher altitudes. On the other hand, a large extent of SO₂ and H₂S stays at high levels in the umbrella region. The sulphur species are only slightly soluble in liquid water, hence, they are not removed by liquid water drops. However, they are scavenged by frozen hydrometeors via direct gas incorporation during diffusional growth of ice. This causes a reduction by ~25% of the potential input of an inert volcanic gas, indicating the great relevance of gas trapping in ice.

Low relative humidity in the troposphere in our simulations caused precipitation to reevaporate before it could reach the ground. As a consequence, no evidence of hydrometeor-ash interaction or gas scavenging could be found in the fallout of the eruption simulated here, although these processes occurred to a significant degree in upper parts of the plume.

Contents

1	Introduction	1
1.1	Composition of Volcanic Gases at the Vent	2
1.2	Microphysical and Chemical Processes in a Volcanic Plume	3
1.3	Observations of Volcanic Eruption Clouds	4
1.4	Numerical Simulations of Explosive Volcanic Plumes	6
2	Volcanic Particles	9
2.1	Properties of Volcanic Particles	9
2.2	Aggregates	10
2.3	Particle Size Distributions	12
3	Microphysics of Hydrometeors and Particles in the Plume	15
3.1	Two-moment Scheme	15
3.2	Categories of Hydrometeors and Volcanic Ashes	18
3.3	Microphysical Processes Considered in the Model	20
3.4	Generalised Gamma Function	21
3.5	Terminal Fall Velocities	24
3.6	Nucleation Processes	25
3.7	Diffusional Growth by Water Vapour Transfer	28
3.8	Autoconversion	30
3.9	Accretion	34
3.10	Melting and Freezing	38
3.11	Thermodynamic Effects of Phase Changes	41
3.12	Salinity Effects	42

4	Scavenging of Volcanic Gases	45
4.1	Scavenging by Liquid Droplets	45
4.1.1	Phase Equilibrium	45
4.1.2	Kinetics of the Phase Transfer	46
4.1.3	Numerical Treatment of Gas Scavenging by Liquid Drops	49
4.2	Scavenging by Ice Particles	50
4.2.1	Incorporation of Gases into Ice	50
4.2.2	Release of Gases from Ice	53
4.3	Transfer of Solutes during Microphysical Processes	53
4.3.1	Limit Solubility	54
5	The Plume Model ATHAM	57
6	Numerical Simulations with ATHAM	61
6.1	Conditions of the Simulation	61
6.2	Reference Experiment	63
6.2.1	Plume Characteristics	64
6.2.2	Hydrometeors	71
6.2.3	Number Concentration	75
6.2.4	Aggregate Qualities	76
6.3	Microphysical Sensitivity Studies	79
6.3.1	Particle-Hydrometeor Interactions	79
6.3.2	Size Distributions of Volcanic Particles	84
6.4	Scavenging of Volcanic Gases in the Plume	88
6.4.1	Behaviour of Volcanic Gases in the Plume	89
6.4.2	Salinity Effect	100

6.4.3	Effect of Ash Particle Growth on the Scavenging Ratio . . .	102
6.4.4	Incorporation of Volcanic Gases into Ice	105
6.4.5	Résumé: Scavenging of Volcanic Gases in the Plume	107
7	Conclusions and Outlook	109
7.1	Particles and Hydrometeors in the Plume	109
7.2	Scavenging of Volcanic Gases in the Plume	111
7.3	Future Plans	113
8	Appendix	117
	References	119

1 Introduction

Explosive volcanic eruptions reach the stratosphere in general at least once every 2 years (*Simkin, 1993*). The injection of large quantities of gases and particles can have an important impact on the atmosphere. Major volcanic events, like the eruption of Mt. Pinatubo in 1991, affect the global climate on time scales of months to years. The additional aerosol loading increases the temperature in the lower stratosphere through the absorption of near infrared and long wave radiation, and also leads to a global cooling of the lower troposphere due to reflection of solar radiation. Fine volcanic ashes – mainly silicate particles – injected into the stratosphere are characterized by grain sizes in the micrometer range. They are efficiently removed by sedimentation from the stratosphere within about a month after the eruption (*Pinto et al., 1989*). Rather sulphur containing volcanic gases than ash are responsible for the climatic effects of explosive volcanic eruptions: the conversion of sulphur dioxide (SO_2) and hydrogen sulphide (H_2S) gases generates sub-micron sulphate particles with life times of several years that are radiatively active (*McCormick et al., 1995*). In addition, volcanic hydrated sulphate aerosols can serve as sites for heterogeneous reactions which deplete ozone (*Hofmann and Solomon, 1989; Michelangeli et al., 1989*, among others). The direct injection of water vapour (H_2O) and halogen compounds like hydrogen chloride (HCl) combined with the effects of sulphate aerosols also modifies microphysical and chemical processes in the stratosphere.

However, little is known about the proportion of volcanic material erupted at the vent that finally reaches the stratosphere. The determination of gas and particle concentrations in the plume is extremely difficult because of the cloud's opaqueness and the inherent risks of directly observing and sampling the volcanic cloud. Volcanic emissions can also be studied remotely by airborne and ground-based instruments and by satellite observations. The petrological method can be employed to estimate the magmatic gas content by comparing pre- and post-eruptive volatile concentrations trapped in ash deposits. The results obtained using different measurement methods, especially for volatile components, often diverge by orders of magnitude. The enormous differences in the observational data are due to uncertainties in each individual measuring technique, but they also result from the fact that the plume is investigated at different distances from the crater and during different states of the eruption: it is not surprising that data obtained in the ascending plume deviate from those measured in the stratosphere. The properties of volcanic ash may be changed by aggregate formation and gases may be chemically altered or scavenged by hydrometeors and volcanic particles.

The goal of this study is to investigate the processes occurring in the eruption column using the plume model ATHAM (**A**ctive **T**racer **H**igh Resolution **A**tmospheric Model). We focus on the scavenging processes during the plume

rise from the lithosphere to the stratosphere, illustrated by the magnifying glass in Fig. (1). The model simulations include spatial scales from about 100 meters to several hundreds of kilometers and time periods from seconds to some hours. We want to analyse the various factors that determine the fraction of volcanic products originally erupted at the vent, which are eventually injected into the stratosphere.

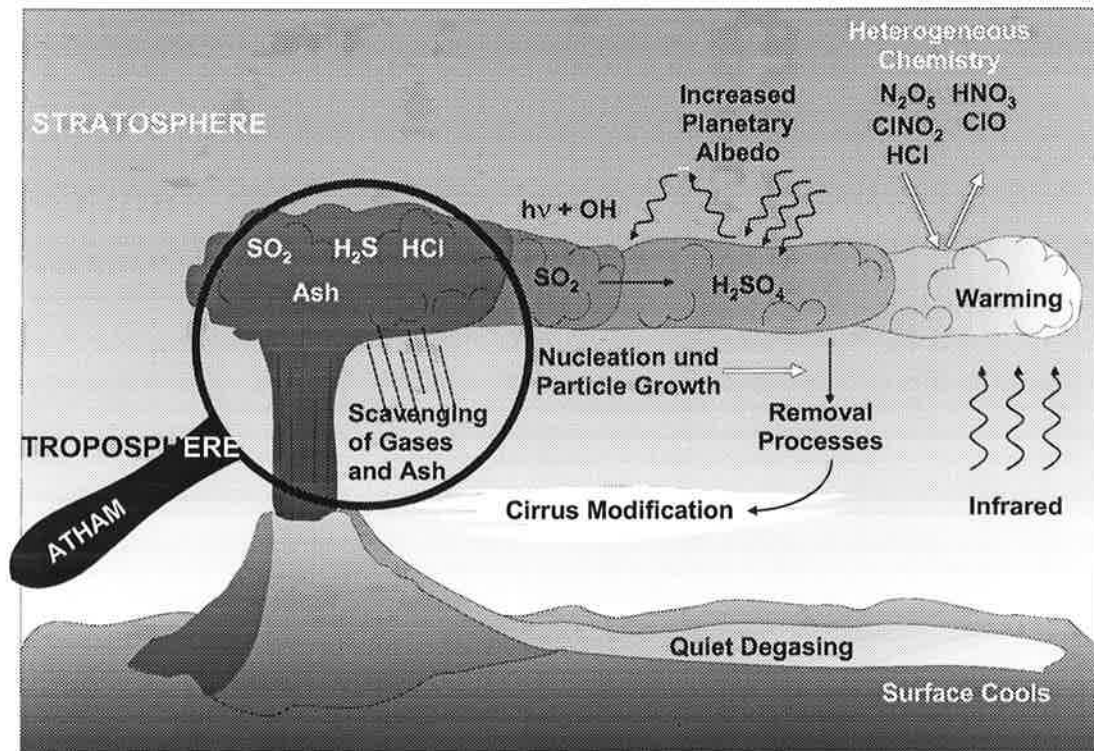


Figure 1: Atmospheric effects of explosive volcanic eruptions: schematic representation after *McCormick et al. (1995)*

1.1 Composition of Volcanic Gases at the Vent

The composition of volcanic gases at the crater varies widely between volcanoes and is also dependent on the individual volcano's state of activity. A comprehensive review about volatiles in magma can be found in *Symonds et al. (1994)*. Water vapour (H_2O) is the most prevalent volcanic gas contributing between 50 and 90 Vol.%. Water in volcanic eruption clouds may result from magmatic sources, steam from ground- or surface waters and entrainment of ambient humidity. The contribution of volcanoes to the tropospheric water burden is negligible, but the injection into the stratosphere can lead to a significant increase in water vapour content. H_2O and the OH radical, which is derived from water vapour

affect a variety of chemical reaction cycles in the stratosphere among which the oxidation of methane and sulphur species.

The second important volcanic gas is carbon dioxide (CO₂) which ranges from 1 to 40 Vol.%. Volcanic CO₂ influences the greenhouse effect on geological time scales, however, the signal of an individual volcanic eruption is small compared to the total CO₂ burden of the atmosphere. In addition, anthropogenic emissions are about 100 times higher than the total natural degassing of the earth per year (*Schmincke, 1993*).

Sulphur gases contribute a smaller portion to the total gaseous volcanic eruptions, typically in the order of 1 to 25 Vol.%, but they are the most relevant species concerning the climatic impact of explosive volcanic events. The dominant sulphur components are SO₂ and H₂S. The H₂S fraction increases with increasing pressure – i.e. depth of the magma chamber – and with decreasing temperature and oxygen concentration of the magma (*Gerlach and Casadevall, 1986*).

The main halogen component is HCl (*Symonds et al., 1988*) with 1 to 10 Vol.%. A variety of other gaseous components are erupted by volcanoes, however, they are only of minor importance on larger scales in time and space. Characteristic gas fractions at the volcanic vent are given in Tab. (1).

Species	H ₂ O	CO ₂	SO ₂	H ₂ S	HCl
Volume %	50 – 90	1 – 40	1 – 25	1 – 10	1 – 10

Table 1: Characteristic composition of volcanic gases at the vent.

1.2 Microphysical and Chemical Processes in a Volcanic Plume

A typical gas-particle-mixture erupted at the volcanic vent is characterised by gas fractions of 3 - 5 wt.% and temperatures between 1000 and 1400 K. The exit velocity is determined by the speed of sound of the mixture, and ranges between 250 - 300 m/s (*Woods, 1995*). The ejecta experience a shock-like temperature decrease leading to crystallisation of microscopic salt particles (primarily chlorides, fluorides, and sulphates of alkali metals and calcium) (*Óskarsson, 1978*). The salt crystals form either homogeneously or on surfaces of preexisting ash particles. The ejecta come into contact with ambient air for the first time and may be oxidised. An upper limit of salt crystallisation is set by the melting point

of the salts being formed. In the study presented here, these initial phenomena are not considered, since we do not resolve small-scale processes near to the vent in our simulations.

In the outer regions of the plume, the entrainment of surrounding air supplies a higher concentration of oxidising species, possibly leading to enhanced oxidation of volcanic material. Preceding sensitivity studies with a chemistry box model, which includes reactions in the gas phase and in the liquid phase under volcanic conditions, indicate that radical chemistry is not significant inside an ascending explosive eruption column. The rising time of an air parcel from the crater to the stratosphere is less than 10 min. This is shorter than the involved characteristic times of chemical radical reactions. The strong surplus of reduced species like SO₂ or H₂S depletes the amount of oxidising species even in the outer plume zones. Due to the opaqueness of the ash cloud, photochemistry is suppressed. Thus, the changes of the volcanic gas concentrations are not controlled by chemical reactions.

Temperature decrease in the rising plume allows for condensation of water vapour; the amount of water determines the microphysical processes. Numerical simulations have shown that the amount of entrained water in the plume is about 3 times that of the volcanic source, dependent on the specific volcanic and environmental conditions (*Herzog, 1998; Graf et al., 1999*). Latent heat release from the condensation of water vapour is essential for the plume dynamics during the eruption (*Herzog et al., 1999*).

The interaction between hydrometeors and volcanic ash leads to coagulation of moist particles. Larger aggregates exhibit an increased fall speed, thus influencing the height and shape of the plume. Hydrometeors and ash-hydrometeor aggregates are able to remove volcanic volatiles from the gas phase. Scavenging processes are most important to prevent volcanic volatiles and ash from being injected into the stratosphere.

1.3 Observations of Volcanic Eruption Clouds

The employment of satellite sensors is the most comprehensive way to measure volcanic eruption clouds for the time being. However, the results are affected by the high optical depth of the plume and the reflectivity of the underlying surface. In addition, the errors vary with cloud mass and area, and they depend on the quality of the estimation of the plume's trajectory and dilution. For example, the error of the total SO₂ mass retrieved from TOMS¹ data ranges from 15 to 30 % (*Krueger et al., 1995*).

¹ TOMS: Total Ozone Mapping Spectrometer.

For the strong eruption of Mt. Pinatubo in 1991, the total mass of SO₂ was 14-26 Mt obtained from TOMS data, 12-15 Mt from SBUV², 14 Mt from AVHRR³ as reported in a paper of *Krueger et al.* (1995). The petrological method predicts a stratospheric injection of only 0.22 Mt SO₂ (*Westrich and Gerlach*, 1992), but the authors doubted that the determined quantity of SO₂ reflects the total amount of that gas.

The contribution of H₂S to the volcanic sulphur content in the stratosphere is highly uncertain. It was discussed for the eruption of El Chichón in 1982 by *McKeen et al.* (1984): H₂S is oxidised to SO₂ with an average lifetime of three days in the stratosphere. An enhanced H₂S concentration means an additional stratospheric source of water vapour. It influences the oxidising capacity of the stratosphere, thereby possibly altering the SO₂ life time. Petrological studies suggest that most of the sulphur gas at the El Chichón eruption was in the form of H₂S (*Rye et al.*, 1984; *Luhr et al.*, 1984), and direct measurements of the post-eruptive fumarolic activity taken by *Kotra et al.* (1993) seven months after the main eruption indicated a H₂S to total gaseous sulphur mass ratio of 80 %. Satellite data of H₂S during explosive eruptions are not available, because it can not be detected by the systems in use at the moment. A secondary increase in the SO₂ concentration – expected to occur because of the 3-day life time of H₂S – was detected by TOMS after El Chichón as reported by *Schneider et al.* (1999), *Hudson* (1996) and *Ahn* (1997) who found evidence for H₂S employing a new retrieval algorithm. For the main eruption of Mt. Pinatubo, thermodynamic calculations indicated that the H₂S concentration was negligible compared to SO₂ (*Westrich and Gerlach*, 1992) and no secondary maximum in the SO₂ concentration was retrieved in TOMS data (*Bluth et al.*, 1992; *Hudson*, 1996; *Ahn*, 1997).

The eruption of El Chichón in 1982 released approximately 1.8 Mt HCl as derived from the petrological method (*Varekamp et al.*, 1984). Three months after the main eruption *Mankin and Coffey* (1984) determined the HCl total column content in the region covered by the volcanic cloud to be approximately 40 % higher than the background value. The increase in HCl may be due to direct injection of chlorine into the stratosphere. This assumption is supported by observations of halite (NaCl) particles in the aerosol cloud (*Woods et al.*, 1985), which could later be converted to HCl.

During the eruption of Mt. Pinatubo, *Westrich and Gerlach* (1992) estimated an emission of about 4.5 Mt HCl derived from the petrological method. However, this substantial additional chlorine loading was not detected in the stratosphere in the weeks that followed the eruption (*Mankin et al.*, 1992; *Wallace and Livingston*, 1992). An increase in the stratospheric chlorine dioxide (OCIO) associated with

² SBUV: Solar Backscatter Ultra Violet instrument.

³ AVHRR: Advanced Very High Resolution Radiometer.

the aerosol cloud has been detected after the Mt. Pinatubo eruption by several authors, see for example *Solomon et al.* (1993); *Waters et al.* (1993); *Toohey et al.* (1993). This enhancement was explained by the transformation of non-volcanic HCl to active chlorine species through heterogeneous reactions on volcanic sulphate aerosols, which might subsequently lead to ozone destruction. Even after the biggest volcanic events which were accompanied by a strong signal in the SO₂ concentration, no HCl increase could be found in ice core data (*Delmas, 1986; Holdsworth et al., 1986*).

The observation of volcanic ash in the plume is a problematic issue due to the opaqueness and the inhomogeneity of the plume. The estimates for the total erupted ash mass on the basis of ash deposit data are rather uncertain and depend on the number and location of the sampling sites. In addition, fallout happens in large areas that cannot be completely covered by observation. The physical properties of particles found at the ground might not reflect those occurring during the transport in the atmosphere. Weather satellites have been used to track drifting volcanic clouds. The use of two-band data in thermal infrared allows for the discrimination of volcanic and meteorologic clouds, for references see *Wen and Rose* (1994). However, significant characteristics of the particles in the plume are not known at present. For example, the shape of individual particles and the grain size distribution have to be presupposed in order to retrieve total mass estimates. Hence, the information about both the total mass and the individual properties of volcanic particles are rather incomplete for the time being.

1.4 Numerical Simulations of Explosive Volcanic Plumes

Obviously, it is rather difficult to obtain consistent observations of emissions from explosive volcanic events. Hence, numerical simulations are an ideal tool to further scrutinize the processes occurring in the eruption column. There are only a few numerical models available at the moment. A highly accurate description of the dynamics is realized in the models of *Wohletz et al.* (1984), *Valentine and Wohletz* (1989), *Dobran and Neri* (1993) and *Neri and Macedonio* (1996). They solve the full set of dynamic equations for each component in a cylindrical geometry. However, this concept is much too extensive in terms of computer time and memory and forbids to consider a higher number of grid points or components, which would be necessary for the investigation of scavenging processes in the plume. The relatively simple models of *Wilson* (1976) and *Woods* (1988, 1993) allow for the consideration of a higher number of transported quantities, but they are only one dimensional top-hat models with a rather coarse description of the dynamics; the mixing of ambient air into the eruption column is determined by an arbitrary entrainment parameter. Nevertheless, the Woods-model and extended

versions of it have been used to simulate the injection of volcanic gases and water vapour into the stratosphere.

Tabazadeh and Turco (1993) investigated the scavenging of HCl and SO₂ in an explosive volcanic plume on the basis of the Woods-model. The simulated temperature in the plume was not lower than -20 °C, hence, the existence of supercooled droplets was favoured compared to ice formation. The scavenging of chemical species in the eruption column was parameterised by assuming solubility equilibrium in supercooled droplets, and the concentration of HCl remaining in the gas phase was derived from rather sophisticated thermodynamical phase diagrams. The authors pointed out that HCl was almost completely transferred into supercooled droplets, resulting in an HCl vapour pressure reduction of up to four orders of magnitude. On the other hand, it was speculated that SO₂ was almost not scavenged in the eruption column: due to its low solubility in liquid water it reaches the stratosphere unaffected by any scavenging in the plume.

Glaze et al. (1997) employed an extended version of the Woods-model (*Glaze and Baloga*, 1996) to study the transport of water vapour by volcanic eruption columns. However, their model formulation did not include any microphysics apart from pure condensation of water vapour, without considering precipitation processes. They obtained a huge injection of water vapour into the stratosphere, which is comparable to the annual input from methane oxidation or 100 mid-latitude thunderstorms.

The simple formulation of the dynamics, especially the representation of entrainment of ambient air in the Woods-model is not sufficient to describe an explosive volcanic plume. The representation of cloud microphysics is necessary to account for a more realistic determination of latent heat release. The plume model ATHAM – being developed in recent years – is especially designed to simulate the mesoscale evolution of an explosive volcanic eruption cloud. The model concept, which is described in Chap. (5), enables a careful representation of the dynamics of the gas-particle-mixture and allows for the consideration of a large number of tracers. ATHAM has been successfully used to simulate the dynamics of an explosive volcanic eruption (*Oberhuber et al.*, 1999). The model has been employed to examine the effects of different environmental conditions (*Herzog et al.*, 1999; *Graf et al.*, 1999) and grain sizes (*Seyfried*, 1999) on the mesoscale plume development.

Within the framework of this thesis, the representation of cloud microphysics in the model has been improved. The interaction between hydrometeors and volcanic ash has been implemented taking into account the formation of hydrometeor-ash-aggregates that lead to more realistic sedimentation features. In addition, the eruption of volcanic gases at the vent and their scavenging by liquid and solid hydrometeors and aggregates has been included.

In the first chapter of this study we illustrate the properties of volcanic ash particles. Thereafter, the two-moment scheme describing the microphysics including the interaction between hydrometeors and ash particles is introduced. The next chapter deals with the parameterisation for scavenging of volcanic gases by liquid water and ice. We will then explain the concept of the plume model ATHAM. In the following, the results from numerical simulations will be presented. The experiments focus on scavenging processes of ash and the most important volcanic gases, HCl, SO₂ and H₂S, in the eruption column. This thesis ends with conclusions and an outlook.

2 Volcanic Particles

2.1 Properties of Volcanic Particles

The highest portion of explosive volcanic emissions in terms of mass is solid matter; in general the solid fraction exceeds 95 wt.% (e.g. *Sparks et al.*, 1997). However, little is known about the initial particle properties when they are erupted at the vent. The particles undergo a variety of modification processes in the plume, most of which are not even qualitatively understood. Magma can reach the earth's surface as a continuous melt (lava) or as a mixture of gases and solid matter. Volcanic particles of all types and sizes that are ejected from the vent into the atmosphere and deposited to the ground are called 'tephra'. These particles result when gases expand due to decompression as the magma moves towards the surface. This gas release causes the magma to explosively disintegrate and produces the volcanic particles. A coarse particle classification is based on the particle diameter (*Schmincke*, 1993): volcanic ash is characterised by a diameter smaller than 2 mm. Particles between 2 and 64 mm are called 'lapilli'. The latter may be formed of single particles or a conglomeration of particles of different sizes. These two particle classes are transported to high altitudes within the convective plume. Larger eruption products which fall ballistically are named 'blocks' or 'bombs'. These are not considered by ATHAM, since they leave the plume very quickly, thus in no way influencing the large scale plume development.

An overview of the qualities of volcanic eruption products is given in *Fisher* (1999) and references therein. The bulk density of tephra is rather variable depending on the composition and the porosity of the material, with bulk densities of about 2000 kg/m³ for magmas with high SiO₂ contents. In general, the density of juvenile particles – derived directly from erupting magma – decreases with the particle size, because larger particles are often built of coagulated, smaller particles or consist of a highly vesicular glass foam. Violent degassing during the magma rise may result in low density material that is called 'pumice' with a density less than 1000 kg/m³. Particles resulting from the sub-volcano basement rocks – contributing about 1-10 wt.% to the total tephra mass with less amounts in the finer particles – are called 'lithic'. These particles can be of any composition and exhibit a rather high density (> 2000 kg/m³).

Basaltic magmas, which have a low viscosity due to their low SiO₂ contents (between 40 - 50 wt.%) are the most common magmas on earth and are the least explosive. Magmas with higher viscosity due to higher SiO₂-contents and higher fractions of volatiles (andesitic or rhyolitic) lead to more explosive volcanic events. One such eruption type called 'plinian' is characterised by high mass eruption rates and eruption columns that may penetrate into the stratosphere.

The composition of volcanic particles is highly variable for different volcanoes. By far the highest fraction of tephra is built of aluminosilicate glass shards formed from gas bubbles bursting in liquid magma. Besides silicon and aluminium, particles contain different amounts of oxides, halides and sulphates of Mg, Ca, Fe, Na, K, Zn and Cu, and a variety of trace elements (*Hobbs et al.*, 1982; *Smith et al.*, 1982; *Rose et al.*, 1982; *Varekamp et al.*, 1986). Salt crystals independent of ash as well as coating of ash particles (sometimes as aerosol droplets) have been observed for different eruptions during in-situ aerial sampling of volcanic plumes (e.g. *Smith et al.* (1982), *Chuan* (1994)).

Particle aggregates have been found in many volcanic deposits (e.g. *Sorem* (1982); *Carey and Sigurdsson* (1982) at Mt. St. Helens, *Mackinnon et al.* (1984) at El Chichón or *Wiesner et al.* (1995) at Mt. Pinatubo). The particle density and shape strongly influence the aerodynamic behaviour of falling tephra. Ash clusters are often porous and probably non-spherical in shape (*Rose et al.*, 1982; *Varekamp et al.*, 1986). Some of the aggregates are rather fragile and thus are often not preserved in deposits. The formation processes of ash clusters in the eruption column are in general not well understood. The next section deals with the description of the principal morphological types and aggregation mechanisms.

2.2 Aggregates

Aggregates can be divided in three main classes: dry aggregates, accretionary lapilli and mud rain. The occurrence of a specific type is determined by the amount of liquid available during aggregation. *Sparks et al.* (1997) give an overview of formation mechanisms in the eruption column.

Collision Mechanisms

Collisions of particles and hydrometeors are caused by turbulent motions in the plume, differences in terminal fall velocities and electrostatic forces.

Particles of different size and density have different fall velocities which result in gravitational or inertial collisions, this process is referred to as accretion in cloud microphysics. In addition, turbulent motions in the plume may result in particle collisions. The efficiency of this process depends on the intensity and the characteristic length scale of the turbulence and on the concentration, size and shape of the particles. The efficiency of collisions is a complex subject: small particles may follow streamlines around larger particles therefore not colliding. Larger particles with larger inertia will not follow the streamlines but will collide. However, particles may rebound after collision if the relative momentum of the particles is too large or if the binding forces are too weak, thus leading to no par-

ticle growth. In comparatively dry environments, electrostatic forces may cause attraction and collision, or repulsion of particles. Electrostatic attractions are effective in bringing small charged particles built of dry, non-conductive material into contact. Considerable electrostatic charge in volcanic plumes had been observed by several authors (see *Schumacher (1994)*; *Sparks et al. (1997)* and references therein). Electrostatic forces work over distances that are large compared to the particle diameter, hence, they are most important for fine, dry ash particles in the early phase of an eruption. They are stronger than gravitational forces for a distance of 30 particle diameters for ash of $1\mu\text{m}$ size, for example. *Schumacher (1994)* verified experimentally the effectiveness of electrostatic ash clustering leading to grain-size characteristics which were similar to those found in Mt. St. Helens distal ash deposits. Quantitative observations about the role of electrostatic forces in particle coagulation processes are rather incomplete at the moment.

Binding Mechanisms

Once ash particles have collided, van-der-Waals-forces lead to successful coalescence of dry particles. If dry particles are charged, electrostatic attraction can act as additional bonding force. The strongest particle bonds result from strong short-range surface tension forces when the particles are moist. Volcanic particles initially become moist by water vapour condensation on their surfaces. This is promoted by the presence of (hygroscopic) salts: coating of particles with salt crystals and aqueous solutions was observed for example in the distal deposits of Mt. St. Helens (*Rose et al., 1982*). The investigation of Guatemalan volcanoes by *Smith et al. (1982)* proved that some of the elements contained in ash are highly water soluble. The forces described so far are reversible, impact on the surface may lead to aggregate breakup. A more durable contact of moist particles can be established if the water layer that coats the particle contains dissolved matter. Evaporation leads to enhanced concentration of the dissolved species finally resulting in crystal bridges which greatly increase the strength of the inter-particle bonds. This process is referred to as 'cementation'. In addition to the clustering mechanisms mentioned above, *Sorem (1982)* has suggested that mechanical interlocking of dry particles of irregular shape might be responsible for particle coagulation.

Post-eruptive processes might alter particle aggregates: ash deposits or rain-falls often accompanying the eruption will destroy a large number of aggregates. On the other hand, formation of ash clusters can also take place on the ground: rain drops, volcanic particles or aggregates falling on fresh ash beds can collect the deposited material, thereby increasing their size after they have already left the atmosphere.

2.3 Particle Size Distributions

The eruption of Mt. St. Helens in May 1980 is one of the most thoroughly studied eruptions that has been investigated with advanced methods of observation. Most of the deposits fell on land in contrast to the more recent Mt. Pinatubo ejecta of 1991, which mainly disappeared into the ocean. The column height of Mt. St. Helens exceeded 14 km for more than 9 hours with a peak height of 24 km, the plume penetrating well into the stratosphere (*Harris et al.*, 1981). The total ash fall mass during the main eruption was estimated to be about $6.3 \cdot 10^{11} \text{kg}$, see the citations in *Carey and Sigurdsson* (1982). The particle concentration in the Mt. St. Helens plume was found to be between $0.2 - 9 \text{g/m}^3$ (*Hobbs et al.*, 1982; *Harris and Rose*, 1983). The estimated total grain size distribution of the Mt. St. Helens ash deposit within an area of 50-500 km around the volcano is illustrated in Fig. (2) (*Carey and Sigurdsson*, 1982). Neither the largest particles that fell within 50 km around the crater nor the smallest that are quasi suspended in the air are included in this representation.

In the volcanological literature, the tephra size distributions are often shown as a function of ϕ -classes with $\phi = -\log_2 d$, where d is the particle diameter in mm. This means, that the interval width increases with increasing radius, leading to relatively larger contributions of bigger particles than in a representation with equal radius interval width. The bimodal structure of tephra particle size distributions observed at several volcanoes (for references see *Sparks et al.* (1997)) is much less pronounced or even vanishes, when referred to equal size intervals rather than to ϕ -classes. Here, we show the relative mass in [%] per radius interval $\Delta r = 1 \mu\text{m}$ in relation to the total mass m_{tot} .

The size distribution determined with radar measurement by *Harris et al.* (1981) was slightly different from that of *Carey and Sigurdsson* (1982) with a shift to bigger particles. The authors suggest that the results are influenced by particle coagulation or breakup of aggregates. The size distribution shown in Fig. (2) monitored by *Carey and Sigurdsson* (1982) might not reflect the real particle distribution that occurred during the transport in the atmosphere. However, does it give information about the original size distribution of the particles entering the atmosphere at the vent? That would imply that all particles that aggregated in the plume collapsed either by the impact at the ground or during the sampling procedure. The samples were treated differently, including wet and dry sieving, depending on their size. It is not possible to determine to what extent the particles erupted at the vent might have altered during the eruption, on landing on the ground or through the sampling techniques. We have employed a fit with two particle modes to represent the size distribution observed by *Carey and Sigurdsson* (1982). The specific size distributions of volcanic particles erupted at the vent are investigated through simulations with ATHAM and presented in

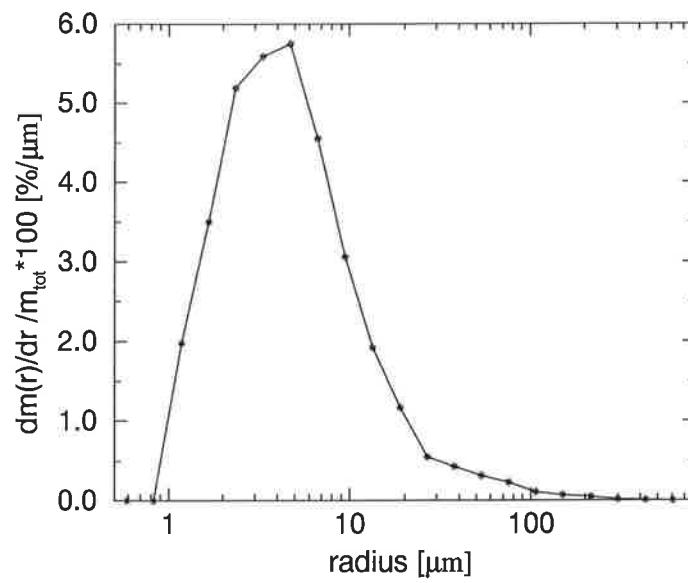


Figure 2: Estimated total grain size distribution of the 18th May 1980 eruption of Mt. St. Helens. Ash deposit within an area 50-500 km from the source, after *Carey and Sigurdsson (1982)*.

Sect. (6.2) and Sect. (6.3.2).

3 Microphysics of Hydrometeors and Particles in the Plume

A complete description of all microphysical processes in a volcanic eruption plume is rather complex. Ash particles as well as volcanic gases should be included: water vapour can condense or deposit on ash surfaces. Volcanic particles can interact with hydrometeors and form clusters with an increased fall speed compared to that of its constituents. Volcanic gases like HCl can be dissolved in liquid drops and thus influence their thermodynamic behaviour.

In the framework of this study, an extended version of the bulk concept which has been previously employed in this model (*Müller, 1997; Herzog et al., 1999; Graf et al., 1999*) has been developed. The earlier scheme considered the processes to be dependent only on the mass concentration of hydrometeors per unit volume. Number concentrations or constant radii of the particles had to be prescribed. The scheme was similar to the parameterisations applied by *Kessler (1969)*, *Wisner et al. (1972)*, *Rutledge and Hobbs (1983)*, and *Lin et al. (1983)*. These rather simple formulations are based on observations under ‘regular conditions’⁴ and produce reasonable results when applied to simulations of the ambient atmosphere. However, they may not be suitable to describe microphysical processes in a volcanic plume. The strong vertical velocities result in large supersaturations. The number concentration belonging to a certain mass content is no longer known and some parameterisations are no longer valid. The environmental conditions in the eruption column are definitely different from those prevailing in the average atmosphere, but there is no data available on volcanic plume microphysics.

3.1 Two-moment Scheme

In order to improve the representation of microphysical behaviour we employed a two-moment scheme following the approach of *Walko et al. (1995)* and *Meyers et al. (1997)*. The particles in the plume are no longer only described by their specific mass, but we also introduced the number concentration – the second moment of the size distribution – as a prognostic variable. In a volcanic plume, the particle history absolutely determines the size distribution of aggregates formed of ash and hydrometeors, especially for high ash contents. We assume that all size distributions follow generalised gamma functions, as proposed by *Flatau et al. (1989)*. The hydrometeors are described by liquid and ice classes, each of which is subdivided into two categories depending on the particle radius. In addition

⁴ In the context of this work ‘regular conditions’ refers to meteorological clouds in an atmosphere which is not influenced by a volcanic eruption.

to the microphysics of hydrometeors, we also consider the interaction with volcanic particles in ATHAM. All classes of hydrometeors are allowed to contain ash, thereby forming larger aggregates. All possible interactions between pure ash, hydrometeors and hydrometeor-ash aggregates are accounted for. The parameterisation of interaction processes for volcanic particles and hydrometeors is based on the assumption that the ash particles are always active as cloud condensation nuclei for liquid as well as for ice clouds. Silicate particles from surface soils have generally been observed to exhibit a large nucleating ability, for an overview see *Pruppacher and Klett (1997)*. In addition, volcanic ash particles are mostly of super-micron size and have been found to be often coated with a layer of soluble salts that lowers the saturation vapour pressure of water, see Chap. (2). Hence, the microphysical formulation is based on the concept of pure water with the volcanic particles acting like hydrometeors as soon as they are coated with water. The processes depend on mass content, radius and number concentration of particles that can be pure hydrometeors, pure volcanic particles or mixed aggregates. The ash mass fraction in the aggregates influences the coagulation efficiencies in the accretion processes. A schematic representation of the two-moment microphysical framework is illustrated in Fig. (3) and will be explained in the following sections.

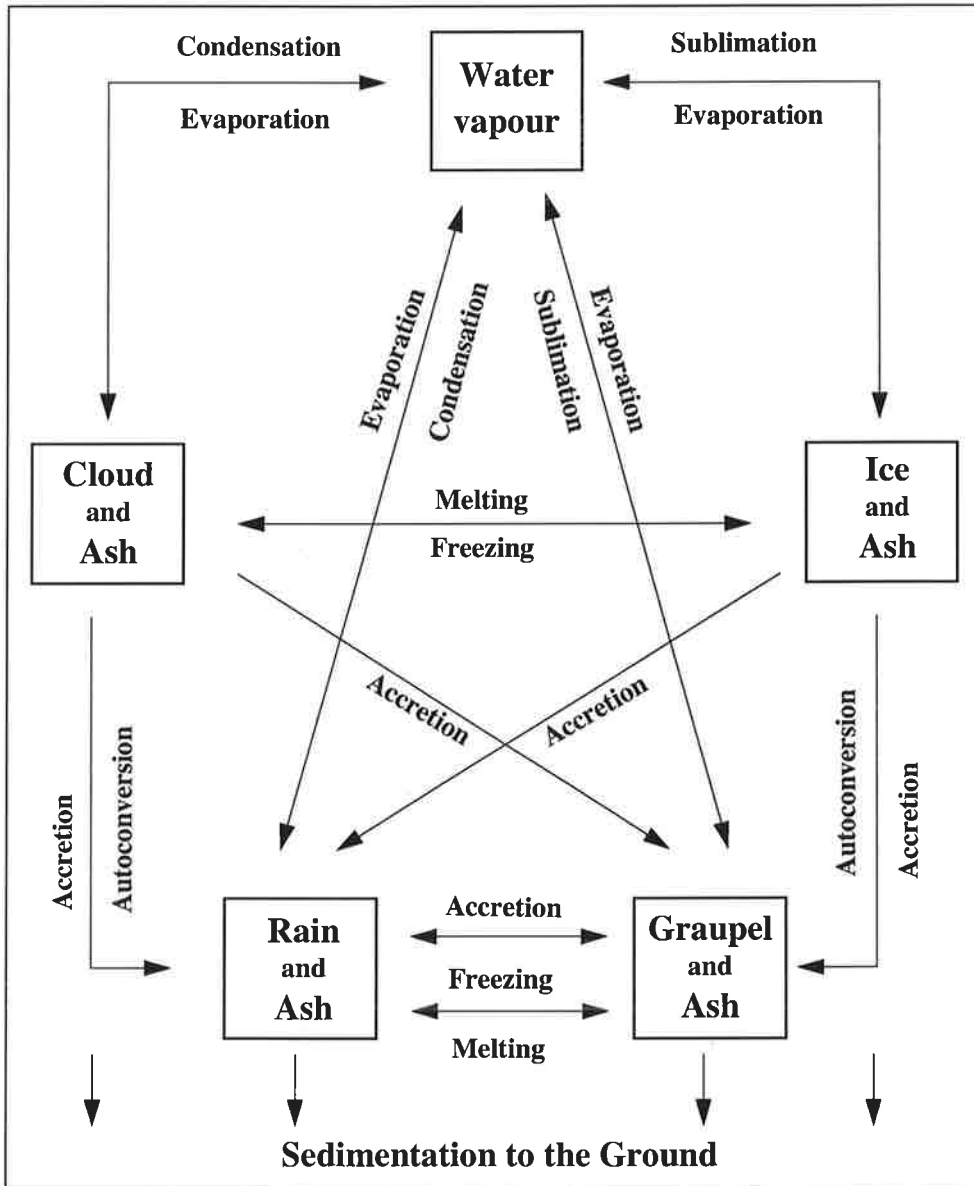


Figure 3: Microphysical Processes occurring in an explosive volcanic plume: a schematic representation.

3.2 Categories of Hydrometeors and Volcanic Ashes

Apart from water vapour, we consider the specific masses q of four classes of hydrometeors, four classes of ash and the number concentrations N as prognostic variables describing the microphysical processes. In our formulation, it is not possible for pure hydrometeors and pure volcanic ash to coexist in a given grid point. This assumption is certainly a simplification, however, the number concentrations in a volcanic plume are so high, see Sect. (2.3), that it seems not very probable that dry volcanic ash and hydrometeors could occur at the same place to a significant extent. The great advantage of this idea is an enormous reduction of the number of tracers and equations we have to consider in the model formulation.

The specific masses of the following categories are predicted in our simulations:

Specific mass content of pure hydrometeors q_x in $[kg/kg_{tot.mass}]$:

- cloud water (q_c);
- cloud ice (q_i);
- rain (q_r);
- graupel (q_h).

Specific mass content of ashes q_{ax} in $[kg/kg_{tot.mass}]$:

- small ash at $T > T_o$ (q_{ac});
- small ash at $T < T_o$ (q_{ai});
- large ash or aggregates at $T > T_o$ (q_{ar});
- large ash or aggregates at $T < T_o$ (q_{ah}).

We specify two different modes of volcanic particles. For each size class of ash, we define a category above the freezing temperature, $T_o = 273.15 K$, and one below. The ash erupted at the crater is initialised in the categories ‘small ash at $T > T_o$ (q_{ac})’ and ‘large ash at $T > T_o$ (q_{ar})’. The initial mean volume radius of erupted ash in the smaller category is $r_{ac} = 2.5 \mu m$ and $r_{ar} = 50 \mu m$ in the larger class. If pure ash in the warm categories, q_{ac} and q_{ar} , is lifted to regions colder than T_o , it is reclassified to the respective cold categories, q_{ai} and q_{ah} , respectively.

As soon as pure ash comes into contact with hydrometeors, small ash (q_{ac} and q_{ai}) will be contained in cloud water aggregates, or in cloud ice aggregates at lower

temperatures. Large ash (q_{ar} and q_{ah}) in aggregates of will be treated like rain or graupel. The specific mass content of water-ash aggregates q_{px} in a category x is obtained from the sum of the specific mass contents of ash q_{ax} and water q_x , it is not predicted during the simulation.

$$q_{px} = q_x + q_{ax}. \quad (1)$$

Specific mass content of ashes of particles q_{px} in [$kg/kg_{tot.mass}$]:

- cloud water / small ash / aggregates at $T > T_o$ (q_{pc});
- cloud ice / small ash / aggregates at $T < T_o$ (q_{pi});
- rain / large ash / aggregates at $T > T_o$ (q_{pr});
- graupel / large ash / aggregates at $T < T_o$ (q_{ph}).

The number concentration, which is predicted in our simulations, refers to these particles px , which are either dry ash, pure hydrometeors or hydrometeor-ash aggregates in the respective category x .

Number concentrations of particles N_{px} in [$Number/kg_{tot.mass}$]:

- cloud water / small ash / aggregates at $T > T_o$ (N_{pc});
- cloud ice / small ash / aggregates at $T < T_o$ (N_{pi});
- rain / large ash / aggregates at $T > T_o$ (N_{pr});
- graupel / large ash / aggregates at $T < T_o$ (N_{ph}).

The densities of pure water and cloud ice crystals are $\rho_c = \rho_r = 1000 \text{ kg/m}^3$ and $\rho_i = 900 \text{ kg/m}^3$, respectively. The density of larger frozen hydrometeors in a volcanic plume is not known. We employ an intermediate density of $\rho_h = 300 \text{ kg/m}^3$ for graupel. It lays between low density snow ($\sim 100 \text{ kg/m}^3$) developing from aggregation of small ice crystals and water vapour growth, and high density hail ($\sim 900 \text{ kg/m}^3$) mainly resulting form drop freezing. For volcanic particles, we prescribe a density of $\rho_{ac} = \rho_{ar} = 1500 \text{ kg/m}^3$. The density of hydrometeor-ash aggregates ρ_{px} is obtained from the volume ratio of ash and water:

$$\rho_{px} = \frac{q_x + q_{ax}}{q_x/\rho_x + q_{ax}/\rho_{ax}}. \quad (2)$$

3.3 Microphysical Processes Considered in the Model

In this section we shortly list the processes considered in the microphysical module used in this study and the related abbreviations, which are similar to those used in the cited literature. The change in specific mass and in number concentration resulting from a certain microphysical process is denoted by a q and N , respectively, attached to the abbreviations given below. The following sections will give a comprehensive description of the single processes.

- Nucleation of:
 - water vapour to build new water clouds (NC);
 - water vapour to build new ice clouds (NI);
- Condensation or evaporation of:
 - cloud water (CEC);
 - rain water (CER);
 - melting graupel (CEMH);
- Deposition or sublimation of:
 - cloud ice (SDI);
 - graupel (SDH);
- Melting of:
 - ice crystals to form cloud droplets (MI);
 - graupel to rain (MH);
- Freezing of:
 - cloud droplets to form ice crystals (FRC);
 - rain to graupel (FRR);
- Autoconversion of:
 - cloud droplets to rain (AUC);
 - ice crystals to graupel (AUI);
- Accretion of:
 - cloud water by rain (ACRC);
 - cloud water by graupel (ACHC);
 - cloud ice by rain (ACRI and ACIR);
 - cloud ice by graupel (ACHI);
 - rain by graupel or vice versa (ACHR);

3.4 Generalised Gamma Function

In our two-moment microphysical parameterisation the size distributions – always referring to the particle radius r_{px} – of hydrometeors, ash particles or aggregates are assumed to follow general gamma distributions as described by *Flatau et al.* (1989), *Verlinde et al.* (1990) and used by *Walko et al.* (1995):

$$f_{gam}(r_{px}) = \frac{1}{\Gamma(\nu_{px})} \left(\frac{r_{px}}{r_{n,px}} \right)^{\nu_{px}-1} \frac{1}{r_{n,px}} \exp \left(-\frac{r_{px}}{r_{n,px}} \right) \quad (3)$$

ν_{px} is the width parameter of the size distribution, $\Gamma(\nu_{px})$ is the gamma function of ν_{px} . $\Gamma(\nu_{px})$ is used as normalisation constant, ensuring that the integral over the particle radius r_{px} from zero to infinity of f_{gam} equals to unity. Hence, f_{gam} is the probability to find a particle of a certain radius r_{px} . The values of the gamma function are stored in a look-up-table. The characteristic radius $r_{n,px}$ is used as a scaling factor and makes the argument of the exponential function – the radius r_{px} – a dimensionless quantity. The values of ν_{px} , $\Gamma(\nu_{px})$ and $r_{n,px}$ are constant for a given point during one time step of the simulation. The characteristic radius $r_{n,px}$ is related to the modal radius r_{mode} by:

$$r_{mode} = (\nu_{px} - 1)r_{n,px}. \quad (4)$$

Any moment P of the distribution can be obtained from:

$$\int_0^{\infty} r_{px}^P f_{gam}(r_{px}) dr_{px} = r_{n,px}^P \frac{\Gamma(\nu_{px} + P)}{\Gamma(\nu_{px})}. \quad (5)$$

The number density distribution, the zeroth moment, is described by multiplying the generalised gamma function with the total particle number $N_{t,px}$:

$$N(r_{px}) = N_{t,px} f_{gam}(r_{px}). \quad (6)$$

For given ν_{px} , the size distribution for each particle class can be derived from its mixing ratio and number concentration. The modal radius of the number distribution function f_{gam} increases monotonically with increasing width parameter ν_{px} . The maximum of the mass or volume distribution $r_{px}^3 f_{gam}$ decreases with increasing width parameter ν_{px} . This is shown in Fig. (4) for a volume mean radius of $\overline{r_{px}} = 2.5 \mu m$ and ν_{px} varying from 1 to 10.

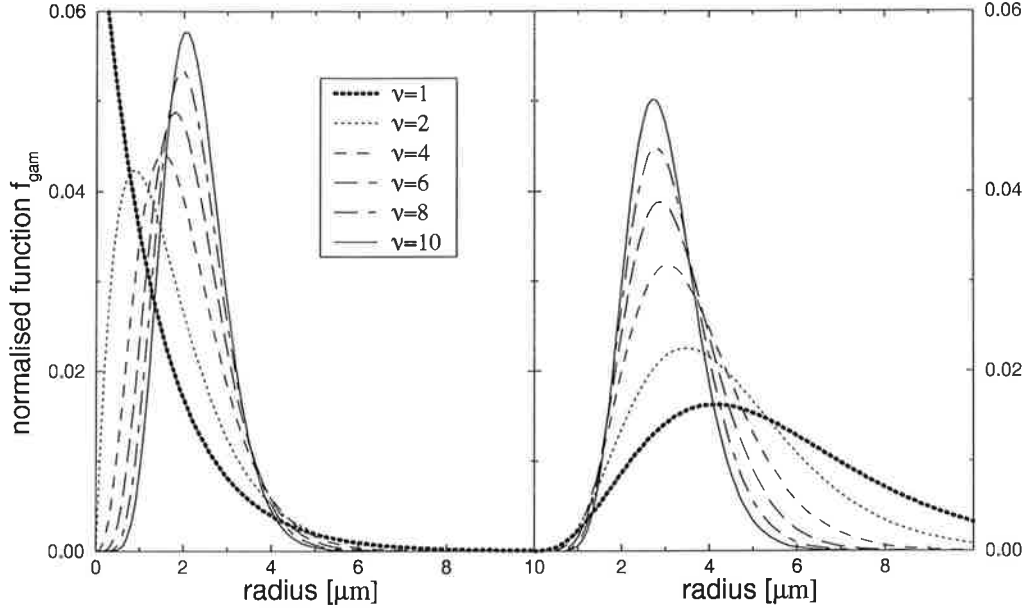


Figure 4: Normalised gamma function as a function of radius for different width parameters ν_{px} varying from 1 to 10 ($\overline{r_{px}} = 2.5 \mu m$). The left panel refers to the number distribution f_{gam} , the right to the mass or volume distribution $r_{px}^3 f_{gam}$

The mean particle mass $\overline{m_{px}}$ of the size distribution, which is related to the mean volume radius $\overline{r_{px}}$, is described by:

$$\begin{aligned}
 \overline{m_{px}} &= \rho_{px} \frac{4}{3} \pi \overline{r_{px}}^3 \\
 &= \int_0^{\infty} \rho_{px} \frac{4}{3} \pi r_{px}^3 f_{gam}(r_{px}) dr_{px} \\
 &= \rho_{px} \frac{4}{3} \pi r_{n,px}^3 \frac{\Gamma(\nu_{px} + 3)}{\Gamma(\nu_{px})}.
 \end{aligned} \tag{7}$$

The mean volume mass equals the total mass content of a category divided by the number concentration:

$$\overline{m_{px}} = \frac{q_{px}}{N_{t,px}} \tag{8}$$

where q_{px} is the specific mass and $N_{t,px}$ the number concentration. Thus, we derive the characteristic radius $r_{n,px}$ from:

$$r_{n,px} = \left(\frac{q_{px}}{N_{t,px}} \frac{3}{4 \pi \rho_{px}} \frac{\Gamma(\nu_{px})}{\Gamma(\nu_{px} + 3)} \right)^{\frac{1}{3}}. \tag{9}$$

The mean volume radius is connected with the characteristic radius by the following equation, derived from Eq. (7):

$$\overline{r_{px}} = r_{n,px} \left(\frac{\Gamma(\nu_{px} + 3)}{\Gamma(\nu_{px})} \right)^{\frac{1}{3}}. \quad (10)$$

For $\nu_{px} = 1$ the number distribution function Eq. (3) reduces to a simple exponential distribution, which had been used in the old microphysical scheme in ATHAM. Stable exponential size distributions of rain drops caused by breakup of larger drops have been observed, for references see *Pruppacher and Klett (1997)*. The simple Marshall-Palmer distribution $N_{MP}(r_{pr})$ (*Marshall and Palmer, 1948*) is only dependent on the hydrometeor's mass content, but it reflects this behaviour quite well:

$$N_{MP}(r_{pr}) = N_0 e^{-2\lambda_r} \quad \text{with} \quad \lambda_r = \left(\pi \frac{q_g \rho_{pr}}{\rho_g q_{pr}} N_0 \right)^{1/4} \quad (11)$$

ρ_{pr} is the rain particle density, q_g and ρ_g are the specific mass content and density of the surrounding gas. For simplicity's sake, exponential Marshall-Palmer-type distributions were often applied for graupel as well (e.g. *Rutledge and Hobbs, 1983; Lin et al., 1983; Wisner et al., 1972*), regardless of its ability to develop into bigger particles. The intercept parameter N_0 is the number concentration for a particle with the hypothetical radius $r = 0$. N_0 is a fixed value for a given hydrometeor type, thus, the distribution is purely determined by the mass content.

The generalised gamma functions employed in the new parameterisation depend on both the mass content and the number concentration. Even the simple exponential size distribution with $\nu_{px} = 1$ in Eq. (3) has now an intercept parameter that is dependent on the characteristic radius $r_{n,px}$ given in Eq. (9). A special advantage of generalised gamma distributions for the simulation of the microphysics in a volcanic plume is, that the width parameter of the size distribution of hydrometeor-ash aggregates ν_{px} can be linearly interpolated with respect to the mass fraction of ash and water:

$$\nu_{px} = \frac{q_{ax} \cdot \nu_{ax} + q_x \cdot \nu_x}{q_{ax} + q_x} \quad (12)$$

with the index ax referring to ash in hydrometeors with the index x . The selection of the width parameter is rather difficult, since not many observations of size distributions are available. On the other hand, the microphysical structure is very sensitive to different values of ν_{px} in the 'regular' atmosphere, as stated

for example by *Meyers et al.* (1997). The overestimation of the concentration of small particles when using exponential Marshall-Palmer-type distributions is avoided in our scheme by assuming $\nu_r = \nu_h = 3.5$ for rain, as observed by *Willis* (1984), for simplicity, the same width parameter is applied for graupel. The size distributions of cloud water and cloud ice are described with $\nu_c = \nu_i = 16$ as used by *Beheng and Doms* (1990) and *Lüpkes* (1991) for typical continental clouds with high concentrations of condensation nuclei. We also expect to get narrow, rather symmetrical distributions in a volcanic plume due to the presence of many condensation nuclei provided by the ash particles.

The initial size distributions of volcanic particles when erupted at the crater are even less known. Post-eruptive compaction or erosion processes raise extreme difficulties in transferring the size and shape of particles observed in the deposits or in the plume to grain size distributions that actually occurred at the vent, see Chap. (2). The effect of the modal radius and the width of the original particle distribution on the plume microphysics and thus on the plume height and the particle deposition characteristics is subject to the sensitivity studies described in Sect. (6.3.2).

3.5 Terminal Fall Velocities

We take into account the fall velocities of each particle class in our model concept. In contrast to other microphysical parameterisations, cloud droplets and cloud ice are allowed to precipitate. In a volcanic plume, cloud particles can contain volcanic ash. This may lead to an increase of the resulting aggregate density, thus, the fall velocity can no longer be neglected. The particles are treated like rigid spheres, and the terminal velocities of the aggregates are calculated using the mixed densities given in Eq. (2).

For very small particles, less than $35 \mu\text{m}$, the interaction between gas and particles can be described by Stokes friction: the friction force is proportional to the relative particle velocity. The stationary fall velocity w_1 is then proportional to the square of the particle radius r_{px} (*Rogers and Yau*, 1989). We use the volume mean radius $\overline{r_{px}}$, since the fall velocity is determined by the particle mass, which is proportional to the particle volume:

$$w_1(r_{px}) = k_1 \rho_{px} \sqrt{\frac{\rho_0}{\rho_g}} \overline{r_{px}}^2 \quad (13)$$

where $k_1 = 1.19 \cdot 10^5 \text{ m}^2 / (\text{kg s})$. The density factor $\sqrt{\rho_0 / \rho_g}$ accounts for the increase in the fall velocity with height. $\rho_0 = 1.12 \text{ kg/m}^3$ is the reference gas density and ρ_g is the density of air at the height being considered.

For medium size particles, radii between $50 \mu\text{m}$ and $500 \mu\text{m}$, the fall velocity increases approximately linearly with the radius (*Rogers and Yau, 1989*):

$$w_2(r_{px}) = k_2 \rho_{px} \sqrt{\frac{\rho_0}{\rho_g}} \sqrt{r_{px}} \quad (14)$$

where $k_2 = 8 \text{ m}^3 \text{ kg}^{-1} \text{ s}^{-1}$.

Large particles ($r_{px} > 500 \mu\text{m}$) are influenced by Newtonian friction which is proportional to the square of the particle velocity. The stationary fall velocity is proportional to the square root of the radius of the particle (*Rogers and Yau, 1989*):

$$\begin{aligned} w_3(r_{px}) &= \sqrt{\frac{8}{3} \frac{\rho_{px} g}{C_{D,x} \rho_0}} \sqrt{\frac{\rho_0}{\rho_g}} \sqrt{r_{px}} \\ &= k_3 \sqrt{\frac{\rho_{px}}{C_{D,x}}} \sqrt{\frac{\rho_0}{\rho_g}} \sqrt{r_{px}} \end{aligned} \quad (15)$$

where $k_3 = 4.833 \text{ m}^2 / (\text{s kg}^{1/2})$, $g = 9.81 \text{ m s}^{-2}$ is the gravity constant.

The drag coefficient $C_{D,x}$ is a constant accounting for the roughness at the surface of a particle. *Gunn and Kinzer (1949)* give for water droplets a value of $C_{D,cp} = 0.54$, *Wisner et al. (1972)* assume $C_{D,h} = 0.6$ for graupel.

The drag coefficients for silicate particles of different shapes and dimensions, determined by *Walker et al. (1971)* and *Wilson and Huang (1979)*, have been successfully applied to simulate the settling velocity of volcanic particles by *Carey and Sparks (1986)* and *Armenti (1988)*. We use for volcanic particles a value of $C_{D,a} = 0.75$ proposed by *Carey and Sparks (1986)*, neglecting its dependence on flow characteristics. For hydrometeor-ash aggregates we apply the values for pure water hydrometeors based on the assumption that the aggregate surface is coated by a film of water or ice.

Hence, our formulation of the particle terminal fall velocities takes into account the effects of particle density, size and drag coefficient and the effect of decreasing friction with height in the atmosphere.

3.6 Nucleation Processes

The surface tension leads to an increased saturation vapour pressure for very small droplets (Kelvin effect). At the same time dissolved species reduce the saturation vapour pressure, the process being most effective for the smallest drops. Hence,

the resulting curve of water saturation vapour pressure as a function of radius (the Köhler Curve) has a maximum at a critical radius, which has a value between 0.1 and $1 \mu m$ under normal atmospheric conditions. Thus, an embryonic particle will continue to grow at constant ambient relative humidity when its size exceeds this critical value: it is then active as a cloud condensation nucleus.

The number concentration of particles in a volcanic plume is extremely high. *Hobbs et al.* (1982) reported the number of ash particles in the periphery of the Mt. St. Helens plume to be 20 000 times greater than in the ambient air. Thus, condensation occurs predominantly on tephra particles inside the plume. The particle radii are usually super-micron size ($> 2 \mu m$) (e.g. *Hobbs et al.*, 1982). The active surface area might be even higher than the value for rigid spheres that was used in the simulations due to the extreme porosity of tephra, see Chap. (2). Hence, the Kelvin effect can be neglected in this survey – ash particles are always active as cloud condensation nuclei for water vapour. We also assume volcanic particles to be active as ice condensation nuclei. Hence, dry ash is able to grow by water vapour condensation or deposition in just the same way as droplets do. The number of volcanic particles determines the number of newly formed hydrometeor-ash aggregates.

In addition, we also consider the formation of new drops, if the supersaturation has not been removed by condensation on ash particles. The radius of these cloud droplets is set constant at $r_{nuc,c} = 1 \mu m$. The change of specific mass related with the nucleation of cloud water is given by:

$$NCq = \frac{q_v - q_{sat,w}}{\Delta t}, \quad \text{for } q_v > q_{sat,w}. \quad (16)$$

where q_v is the specific content of water vapour and $q_{sat,w}$ the water vapour content at the saturation limit, see Eq. (22). However, the strong supersaturations in the central rising zone of the eruption column would result in unrealistic high number concentrations, thus, it is not allowed to exceed a maximum value, $N_{max,c}$. In this study, we employ the number of condensation nuclei determined empirically by (*Twomey and Wojciechowski*, 1969) in continental air to be the critical number concentration.

$$N_{max,c} = 6 \cdot 10^8 \sqrt{S_w - 1} \quad (17)$$

where $S_w = q_v/q_{sat,w}$ is the saturation ratio of water vapour with respect to liquid water. The maximum number of new droplets increases with increasing supersaturation. This parameterisation is certainly a simplification, but it represents a good approach for the first applications of this scheme. The increase in cloud

droplet number concentration is given by dividing the amount of nucleated water by the mass of a single nucleated particle $m_{nuc,c} = 4 \cdot 10^{-15} \text{ kg}$. We obtain for the change in number concentration related with the nucleation of cloud water:

$$NCn = \min\left(N_{max,c}, \frac{NCq}{m_{nuc,c}}\right) \quad \text{and} \quad \frac{\partial}{\partial t} N_{pc} = +NCn, \quad (18)$$

and for the time dependent change of the specific mass:

$$\frac{\partial}{\partial t} q_c = \min(NCn \cdot m_{nuc,c}, NCq) \quad \text{and} \quad \frac{\partial}{\partial t} q_v = -\frac{\partial}{\partial t} q_c.$$

The formation of new cloud ice particles from the gas phase is limited to the number of ice nuclei N_f in the undisturbed atmosphere. The number of active cloud ice nuclei depends on the temperature and can be described at normal atmospheric conditions (Fletcher, 1962):

$$N_f = \frac{q_g}{\rho_g} N_{0,f} \cdot e^{\beta(T_0 - T)} \quad (19)$$

$$\text{with } \beta = 0.6 \text{ K}^{-1} \quad \text{and} \quad N_{0,f} = 10^{-2} \text{ m}^{-3}.$$

The exponential decrease of active ice nuclei with increasing temperature causes this process to be only effective at temperatures well below the freezing point.

There are more comprehensive parameterisations describing the number of active ice nuclei in recent literature (Meyers *et al.*, 1992; Walko *et al.*, 1995). They represent different physical mechanisms and consider the effects of ice supersaturation and temperature. However, the rather simple Fletcher-formula is applied here for first investigations of microphysics in a volcanic plume.

From the mass of a nucleated cloud ice particle, $m_{nuc,i} = 3.8 \cdot 10^{-15} \text{ kg}$, and the radius of nucleated ice, $r_{nuc,i} = 1 \mu\text{m}$, we yield for the change in cloud ice number concentration due to nucleation:

$$\frac{\partial}{\partial t} N_{pi} = NI_n = \frac{\text{Max}(0., N_f - N_{pi})}{\Delta t}. \quad (20)$$

The mixing ratio tendencies caused by nucleation are given by:

$$NIq = m_{nuc,i} \cdot NI_n, \quad (21)$$

$$\frac{\partial}{\partial t} q_i = +NIq \quad \text{and} \quad \frac{\partial}{\partial t} q_v = -NIq.$$

The number of ice particles has been observed to be much higher than the number of ice forming nuclei in many clouds, especially at relatively warm temperatures. The reasons and mechanism responsible for this phenomenon are still not completely understood, for an overview see *Pruppacher and Klett (1997)*. The ice-multiplication process has been neglected in the framework of this study. Most of the cloud ice in this study is present at temperatures below -20°C , where ice multiplication processes are rather ineffective. In addition, no comprehensive quantitative description over the whole temperature range under consideration is available.

3.7 Diffusional Growth by Water Vapour Transfer

The water vapour pressure at the saturation limit over water, $p_{sat,w}$, and over ice, $p_{sat,i}$, is determined by applying the empirical Magnus-formula, see e.g. *Laube and Höller (1987)*, that provides the temperature dependence of the saturation vapour pressure:

$$p_{sat,w} = 610.7 \exp\left(17.25 \frac{T - T_0}{T - 36}\right), \quad (22)$$

$$p_{sat,i} = 610.7 \exp\left(22.33 \frac{T - T_0}{T - 2}\right) \quad (23)$$

where $T_0 = 273.15$ K. Deviations from the saturation value lead to mass exchange between existing hydrometeors and gaseous water vapour. This transfer can be expressed by:

$$\frac{\partial}{\partial t} m_v = 4\pi r_{px} C_v \frac{S - 1}{F_k + F_d} \quad (24)$$

where F_k is related to heat-conduction and F_d to water vapour diffusion, (*Byers, 1965*), given in Eq. (25) and Eq. (26). m_v is the water vapour mass and r_{px} is the radius of the droplet or water-ash aggregate. $S = q_v/q_{sat}$ is the saturation ratio of water vapour with respect to liquid water or ice. q_v is the specific content of water vapour and q_{sat} the water vapour content at the saturation limit.

The effect of heat-conduction F_k is given by:

$$F_k = \left(\frac{L_v}{R_v T} - 1\right) \frac{L_v}{K_a T} \quad (25)$$

where L_v is the evaporation or the sublimation enthalpy, R_v the specific gas constant for water vapour, K_a the thermal conductivity of air and T the in situ

temperature. Finally, F_d is the contribution of water vapour diffusion:

$$F_d = \frac{R_v T}{p_{sat} D_v} \quad (26)$$

where p_{sat} is the saturation vapour pressure over water or ice and D_v the diffusion coefficient for water vapour in air.

The ventilation coefficient C_v depends on the Reynolds number Re and describes the effect of turbulence caused by the circulation around a falling droplet. It is defined as the ratio of the water mass fluxes to or from a moving drop related to the fluxes of a motionless one. For simplicity, we apply the same approach of C_v to all particles regardless of their different sizes. Using the terminal fall velocity w_3 given in Eq. (15) for large particles, which are most relevant for ventilation effects we get (*Wisner et al.*, 1972):

$$C_v = 1 + 0.22 Re^{1/2} \quad (27)$$

$$\text{with } Re = \frac{2w_3 r_{px}}{\nu_{vis}}, \quad w_3 = k_3 \sqrt{\frac{\rho_{px}}{C_D}} \sqrt{\frac{\rho_0}{\rho_g}} \sqrt{r_{px}}$$

where ν_{vis} is the kinematic viscosity of air. We obtain for the ventilation coefficient C_v :

$$C_v = 1 + V_{px} r_{px}^{3/4} \quad (28)$$

$$\text{with } V_{px} = 0.22 \left(\frac{2k_3}{\nu_{vis}} \sqrt{\frac{\rho_{px}}{C_D}} \sqrt{\frac{\rho_0}{\rho_g}} \right)^{1/2}$$

Integration over the size distribution gives the change of hydrometeor mass:

$$\begin{aligned} \frac{\partial}{\partial t} q_x &= 4\pi \frac{S-1}{F_k + F_d} \int_0^\infty r_{px} (1 + V_{px} r_{px}^{3/4}) N(r_{px}) dr_{px} \\ &= 4\pi \frac{S-1}{F_k + F_d} N_{t,px} \left(r_{n,px} \frac{\Gamma(\nu_{px} + 1)}{\Gamma(\nu_{px})} + V_{px} r_{n,px}^{7/4} \frac{\Gamma(\nu_{px} + 7/4)}{\Gamma(\nu_{px})} \right) \end{aligned} \quad (29)$$

employing the definitions for $N(r_{px})$ given in Eq. (3) and Eq. (6). Eq. (29) is applied to get the change of mass content due to diffusional growth, using the respective values for each category. At temperatures below the freezing point one has to apply the sublimation enthalpy instead of the evaporation enthalpy in Eq. (25). Depending on the temperature, the saturation vapour pressure over water or ice is used in Eq. (26). Condensation and evaporation can also occur

at melting graupel, since it can exist above the melting temperature for a longer period of time in contrast to cloud ice. Melting graupel is coated by a film of liquid water. Therefore, the transition of water vapour to the gas phase is then performed with the values of liquid water.

The mixing ratio tendencies are given by:

$$\begin{aligned}
 \frac{\partial}{\partial t} q_c &= +CEC, & \frac{\partial}{\partial t} q_r &= +CER, \\
 \frac{\partial}{\partial t} q_i &= +SDI, & \frac{\partial}{\partial t} q_h &= +SDH, \\
 \frac{\partial}{\partial t} q_n &= +SDMH, \\
 \frac{\partial}{\partial t} q_v &= -CEC - CER - SDI - SDH - SDMH.
 \end{aligned}
 \tag{30}$$

The aggregates can be treated as pure hydrometeors given that the water or ice fraction forms a coating layer at the aggregate surface. Hence, water contained in hydrometeor-ash aggregates is allowed to be transferred between the gas phase and the particle in the same way as in pure water hydrometeors.

The ash content is not affected by diffusional growth of aggregates and the number concentration is not changed during water vapour transfer except for total evaporation or sublimation of pure water hydrometeors. Evaporation or sublimation results in drying of aggregates, possibly leading to their disintegration. On the other hand, cementation result in rather stable aggregates, see Chap. (2). No quantitative data on this process are available, thus breakup of ash-clusters has been neglected so far.

3.8 Autoconversion

Further particle growth is caused by water vapour transfer from the gas phase to the drop's surface, after the initial nucleation of very small droplets or ice crystals. Coagulation is less important for small drops, yet results in a broadening of the drop size spectrum. Under regular atmospheric conditions, a cloud drop can attain a radius of $20 \mu m$ in about 10 min, mainly by condensation. Above this radius the rate of drop collision rapidly increases since the collision cross section and settling speed become large enough, so that coagulation is likely to be the dominant growth process. Since we do not use the full stochastic coagulation equation in our simulations, we ignore interactions of particles inside one category. The coagulation of two cloud particles leading to a transfer of cloud particles to the larger category is parameterised by a process called autoconversion.

Kessler (1969) suggested a simple approach based on a limit mass content of cloud droplets above which the autoconversion process starts. This idea is based on observations of regular clouds indicating that at a certain limit of water content the minimum size of particles for coagulation processes to be efficient is reached. In a volcanic plume, this parameterisation is no longer valid, because the number concentration of condensation nuclei and the supersaturation is much higher than in the regular atmosphere. We use the autoconversion rate proposed by *Berry and Reinhardt* (1974) that is dependent on the mass content as well as on the particle size. They defined an average autoconversion rate ξ/τ to depend on the mean number radius $r_{c,av}$ of an aggregate and the width parameter ν_{px} :

$$AUCq = E_{auc} \cdot \frac{\rho_{pc} \xi}{\tau}$$

$$\text{where } \xi = q_g q_{pc} 2.7 \cdot 10^{-2} \left(10^{20} r_{c,av}^4 (\nu_{px} + 1)^{-0.5} - 0.4 \right) \quad (31)$$

$$\text{and } \tau^{-1} = \frac{q_g q_{pc}}{3.7} \left(10^6 r_{c,av} (\nu_{px} + 1)^{-0.5} - 0.75 \right)$$

where q_{pc} is the mass of a cloud-ash aggregate with the density ρ_{pc} . Coagulation of pure dry volcanic particles is neglected, autoconversion only takes place if the aggregate is coated by water. The coagulation efficiency of aggregates E_{auc} is not known. We estimate zero efficiency for dry ash, and for pure hydrometeors we use $E_{pure,auc} = 1$, a common practice for water drops. The coagulation efficiency of aggregates is assumed to be proportional to the water mass fraction in an aggregate, in the same way as applied for accretion processes shown below. If the water fraction in the hydrometeor-ash aggregate is larger 50 wt.%, the coagulation efficiency given in the literature for pure water hydrometeors is applied (e.g. *Wisner et al.*, 1972, among others). This approach is a rough estimate representing the increase of the sticking probability with increasing amount of liquid water. For very small water fractions the coagulation efficiency might be overestimated, since the aggregates are not completely coated by a layer of water or ice. However, for dry particles electrostatic forces and mechanical interlocking could become more important, as discussed in Chap. (2). The possible overestimation of ‘wet’ aggregation might be compensated by underestimation of other growth processes. We obtain for the ash-cloud aggregates:

$$E_{auc} = \min \left(1, \frac{q_c}{q_{ac}} \right). \quad (32)$$

The mixing ratio tendencies are given by:

$$\frac{\partial}{\partial t} q_{pr} = +AUCq \quad \text{and} \quad \frac{\partial}{\partial t} q_{pc} = -AUCq. \quad (33)$$

The change in number concentration can be calculated from:

$$\frac{\partial}{\partial t} N_{pr} = AUCnr = E_{auc} \cdot 3.5 \cdot 10^6 \frac{\xi}{\tau} \quad (34)$$

$$\frac{\partial}{\partial t} N_{pc} = -AUCnc = -\frac{AUCq}{\overline{m_c}}$$

where $\overline{m_c}$ is the mean volume mass of a cloud aggregate. The change in cloud droplet-aggregate number concentration is estimated under the assumption that all particles have the same probability to take part in autoconversion, regardless of their radii.

The autoconversion of small ice crystals to larger ice particles can occur by water vapour deposition, by riming (i.e., contact freezing of cloud water droplets) or by coagulation of cloud ice to form larger aggregates. The latter process is temperature-dependent and becomes less likely the more the temperature decreases due to the decreasing coalescence efficiency (*Lin et al.*, 1983). The fast ascent of the volcanic eruption column causes the ice cloud to exist at very low temperatures at the tropopause region. Hence, ice crystal growth is assumed to arise predominantly from the deposition of water vapour. The resulting density of a pure hydrometeor will be rather low and is set to $\rho_h = 300 \text{ kg/m}^3$ – a value between snow and hail – in our model simulations. The mass transfer of pristine ice crystals to larger aggregates due to water vapour deposition is described by shifting all ice particles of aggregates larger than the limit radius of $r_{pi,lim} = 62.5 \mu\text{m}$ to graupel (aggregates) as proposed by *Harrington et al.* (1995) and *Walko et al.* (1995). We have to integrate over the size distribution of ice from $r_{pi,lim}$ to infinity. This way, we obtain the amount of ice (aggregates) transferred to graupel (aggregates), and we get for the tendency in number concentration:

$$\begin{aligned} AUI n &= E_{aui} \cdot \int_{r_{pi,lim}}^{\infty} N(r_{pi}) d(r_{pi}) \\ &= E_{aui} \cdot N_{t,pi} \int_{r_{pi,lim}}^{\infty} f_{gam}(r_{pi}) d(r_{pi}), \end{aligned} \quad (35)$$

and for the mass content change:

$$\begin{aligned} AUI q &= E_{aui} \cdot \int_{r_{i,lim}}^{\infty} m(r_{pi}) N(r_{pi}) d(r_{pi}) \\ &= E_{aui} \cdot \frac{4}{3} \pi \rho_{pi} N_{t,pi} \int_{r_{pi,lim}}^{\infty} r_{pi}^3 f_{gam}(r_{pi}) d(r_{pi}). \end{aligned} \quad (36)$$

Based on the assumption that pure, i.e. dry, volcanic ash does not grow and for consistency with autoconversion of cloud water and accretion processes, we use for the collection efficiency E_{aui} for autoconversion of ice-aggregates:

$$E_{aui} = \min\left(1, \frac{q_i}{q_{ai}}\right). \quad (37)$$

The solution for the zeroth and the third moments P (see Eq. (5)), of the incomplete gamma function is obtained from:

$$\int_{r_{pi,lim}}^{\infty} r_{pi}^P f_{gam}(r_{pi}) dr_{pi} = \int_0^{\infty} r_{pi}^P f_{gam}(r_{pi}) dr_{pi} - \int_0^{r_{pi,lim}} r_{pi}^P f_{gam}(r_{pi}) dr_{pi} \quad (38)$$

where the second term is numerically integrated using the trapezium rule (*Fichtenholz*, 1964).

Based on the assumption that the autoconversion process of cloud ice in a volcanic plume is controlled by water vapour deposition, we neglect any change in the total number concentration, large cloud ice is simply reclassified as graupel. Hence, for the tendencies in mass content and number concentration of ice and graupel we get:

$$\begin{aligned} \frac{\partial}{\partial t} q_{ph} &= +AUIq & \text{and} & & \frac{\partial}{\partial t} q_{pi} &= -AUIq, \\ \frac{\partial}{\partial t} N_{ph} &= +AUI n & \text{and} & & \frac{\partial}{\partial t} N_{pi} &= -AUI n. \end{aligned} \quad (39)$$

The transfer of the pure water q_x and volcanic particle q_{ax} mass fraction contained in a hydrometeor-ash aggregate $q_{px} = (q_x + q_{ax})$ is calculated in proportion to their fraction f in the aggregates:

$$f_x = \frac{q_x}{q_{px}} \quad \text{and} \quad f_{ax} = 1 - f_x, \quad (40)$$

$$\frac{\partial}{\partial t} q_x = f_x \frac{\partial}{\partial t} q_{px} \quad \text{and} \quad \frac{\partial}{\partial t} q_{ax} = f_{ax} \frac{\partial}{\partial t} q_{px}. \quad (41)$$

This procedure is based on the assumption that each hydrometeor contains the same portion of ash, hence, the aggregates are well mixed.

3.9 Accretion

We introduce auxiliary variables and indices in order to explain accretion processes: the collecting species Y collects the species X . After derivation of the general equations with these variables, we will show the corresponding tendencies for mass contents and number concentrations of hydrometeors and aggregates.

Accretion processes are simulated by applying the stochastic collection equation for two interacting species X and Y using the hydrodynamic collection kernel K_{xy}

$$K_{xy} = E_{xy} \pi (r_x + r_y)^2 |w_x(r_x) - w_y(r_y)| \quad (42)$$

The collection efficiency E_{xy} is equal to the product of collision efficiency and coalescence efficiency. The coalescence efficiency for liquid drops smaller than about $100 \mu\text{m}$ is usually assumed to be unity (*Rogers and Yau, 1989*). The coalescence efficiency decreases with temperature for frozen particles and depends on both the individual charges and the ambient electric field for charged particles. The collision efficiency is defined by the ratio of the actual collision to number of particles in an area equal to the geometric cross section: it is influenced by inertial, aerodynamic and electric forces. Most of these effects are difficult to observe and they show a strong non-linear behaviour. In the concept of this work, we will neglect the radius dependency of the collection efficiency as well as electric effects. The collection efficiency is also dependent on the shape of the colliding particles. Higher particle densities and lower air density lead to increased collision efficiencies since the relative velocities increase (*Khain, 1999*). These effects have not been considered in the framework of this study.

For accretion processes of hydrometeor-ash aggregates, in particular, the collection efficiencies are unknown. Therefore, they are parameterised by the same approach we employed for autoconversion processes described in Sect. (3.8). Again, the aggregation of dry volcanic ash is neglected: coagulation of volcanic particles occurs only if they are coated by water or ice. The collection efficiencies $E_{xy,agg}$ for accretion processes are linearly interpolated between the values for pure hydrometeors E_{xy} and zero efficiency assumed for pure ash. We suppose that the collision efficiency is determined by the aggregate containing the higher water or ice fraction.

$$E_{xy,agg} = E_{xy} \cdot \min(1., \max(\frac{q_x}{q_{ax}}, \frac{q_y}{q_{ay}})). \quad (43)$$

The rate of change in the specific mass content $\frac{\partial q_x}{\partial t}$ of species X due to collisions

with species Y is given by:

$$AcYXq = \frac{\rho_g}{q_g} \frac{4}{3} \pi^2 \rho_x E_{xy} \quad (44)$$

$$\cdot \int_0^\infty \int_0^\infty r_x^3 (r_x + r_y)^2 |w_x(r_x) - w_y(r_y)| N_x(r_x) dr_x N_y(r_y) dr_y.$$

The analytical solution of this double integral is difficult to obtain. There are two assumptions widely held in the literature:

- Neglecting the change in radius and fall velocity of smaller particles compared to larger ones. This reduces Eq. (44) to the continuous growth equation, assuming the smaller droplets have a uniform radius and are suspended in the air (e.g. *Kessler (1969)*).
- Neglecting the radius dependence of the terminal velocity difference in Eq. (44), $|w_x(r_x) - w_y(r_y)|$. This difference is replaced by the constant value $|\Delta w_{xy}|$ calculated for the volume mean radii \bar{r} and can thus be drawn out of the integral (*Wisner et al., 1972*).

In a volcanic plume, the first approximation is no longer valid since all hydrometeors can be polluted by ash. For simplicity, we chose the Wisner-approximation, that was found to be most suitable for particles of different fall velocities (*Verlinde et al., 1990*). With the generalised gamma distributions and under the assumption that the particles are spherical we have:

$$ACYXq = \frac{\rho_g}{q_g} \frac{4}{3} \pi^2 \rho_x E_{xy} |\Delta w_{xy}| \quad (45)$$

$$\cdot \int_0^\infty \int_0^\infty (r_x^5 + 2r_x^4 r_y + r_x^3 r_y^2) N_x f_{gam}(r_x) N_y f_{gam}(r_y) dr_x dr_y.$$

The general solution of this equation can be obtained analytically with the aid of Eq. (5):

$$ACYXq = \frac{\rho_g}{q_g} \frac{4}{3} \pi^2 \rho_x E_{xy} |\Delta w_{xy}| \frac{1}{\Gamma(\nu_x) \Gamma(\nu_y)} \quad (46)$$

$$\cdot \left(N_x r_{n,x}^5 \Gamma(\nu_x + 5) \Gamma(\nu_y) \right.$$

$$+ 2 N_x r_{n,x}^4 \Gamma(\nu_x + 4) N_y r_{n,y} \Gamma(\nu_y + 1)$$

$$\left. + N_x r_{n,x}^3 \Gamma(\nu_x + 3) N_y r_{n,y}^2 \Gamma(\nu_y + 2) \right).$$

The rate at which the number concentration N_x of species X decreases due to collections by species Y with concentration N_y may be written as:

$$\begin{aligned}
 ACYXn &= \frac{\rho_g}{q_g} \pi E_{xy} \\
 &\cdot \int_0^\infty \int_0^\infty (r_x + r_y)^2 |w_x(r_x) - w_y(r_y)| N_x(r_x) dr_x N_y(r_y) dr_y
 \end{aligned} \tag{47}$$

After applying the Wisner-approximation we can obtain analytically:

$$\begin{aligned}
 ACYXn &= \frac{\rho_g}{q_g} \pi E_{xy} |\Delta w_{xy}| \frac{1}{\Gamma(\nu_x) \Gamma(\nu_y)} \\
 &\cdot \left(N_x r_{n,x}^2 \Gamma(\nu_x + 2) \Gamma(\nu_y) \right. \\
 &+ 2 N_x r_{n,x} \Gamma(\nu_x + 1) N_y r_{n,y} \Gamma(\nu_y + 1) \\
 &\left. + N_y r_{n,y}^2 \Gamma(\nu_y + 2) \Gamma(\nu_x) \right).
 \end{aligned} \tag{48}$$

The number of the collecting particles does not change, they only gain mass by accretion. In cases where the destination category is different from both the collecting and the collected classes, the accretion process is calculated twice with the collector and collecting categories reversed (e.g. accretion of cloud ice by rain forming graupel below the freezing point). In what follows we will explain the accretion processes for aggregates. The related changes of the hydrometeor and ash content contained in the aggregates are calculated from Eq. (40) and Eq. (41), the collision efficiency follows from Eq. (43).

From the accretion of cloud droplet by rain we get additional rain. If the small drops contain ash, this process leads to larger aggregates. For the collection efficiency of the pure hydrometeors we use $E_{rc} = 1$.

$$\begin{aligned}
 \frac{\partial}{\partial t} q_{pr} &= +ACRCq, & \frac{\partial}{\partial t} q_{pc} &= -ACRCq, \\
 \frac{\partial}{\partial t} N_{pc} &= -ACRCn.
 \end{aligned} \tag{49}$$

The accretion of ice crystals by graupel leads to more graupel, respectively aggregates. With the sticking probability E_{hi} following *Lin et al.* (1983)

$$E_{hi} = e^{0.025(T-T_0)}, \tag{50}$$

we obtain:

$$\begin{aligned}\frac{\partial}{\partial t}q_{ph} &= +ACHIq, & \frac{\partial}{\partial t}q_{pi} &= -ACHIq, \\ \frac{\partial}{\partial t}N_{pi} &= -ACHIn.\end{aligned}\quad (51)$$

At temperatures below the freezing point, the accretion of cloud droplets by graupel leads to contact freezing of cloud water increasing the graupel or aggregate mass. Above the freezing point, the same process leads to a gain of heat for graupel. This results in additional melting which is considered below in the equation for melting of graupel, Eq. (59). Melted graupel and accretioned cloud droplets form new rain water. We apply a collection efficiency for cloud droplets at graupel $E_{hc} = 1$ and get:

$$\begin{aligned}\frac{\partial}{\partial t}q_{pc} &= -ACHCq, & \frac{\partial}{\partial t}N_{pc} &= -ACHCn, \\ \frac{\partial}{\partial t}q_{ph} &= +ACHCq & \text{for } T < T_0, \\ \frac{\partial}{\partial t}q_{pr} &= +ACHCq & \text{for } T > T_0.\end{aligned}\quad (52)$$

The accretion of cloud ice by rain leads to contact freezing of supercooled rain water. The process diminishes both cloud ice and rain content and leads to the formation of new graupel or graupel aggregates.

$$\begin{aligned}\frac{\partial}{\partial t}q_{ph} &= +ACRIq + ACIRq, \\ \frac{\partial}{\partial t}N_{ph} &= 0.5(ACRI n + ACIRn), \\ \frac{\partial}{\partial t}q_{pi} &= -ACRIq, & \frac{\partial}{\partial t}q_{pr} &= -ACIRq, \\ \frac{\partial}{\partial t}N_{pi} &= -ACRI n, & \frac{\partial}{\partial t}N_{pr} &= -ACIRn.\end{aligned}\quad (53)$$

Finally, a differential fall velocity between graupel and rain also results in accretion. This will lead to more graupel-aggregate formation below the freezing temperature. Above the freezing temperature, melting graupel will cause rain-aggregate formation. This is considered in the equation for melting of graupel, Eq. (59).

With $E_{rh} = 1$ one obtains for $T < T_0$:

$$\begin{aligned} \frac{\partial}{\partial t} q_{ph} &= +ACHRq, & \frac{\partial}{\partial t} q_{pr} &= -ACHRq, \\ \frac{\partial}{\partial t} N_{pr} &= -ACHRn. \end{aligned} \quad (54)$$

3.10 Melting and Freezing

Water contained in the hydrometeor-ash aggregates is assumed to melt or freeze like pure water hydrometeors. A corresponding fraction of volcanic ash in the aggregate is transferred to the melted or frozen category, respectively. This ash fraction is proportional to that of water or ice transfer during the process considered. The corresponding fractions of water and volcanic material are again obtained from Eq. (40) and Eq. (41).

We suppose that cloud ice will melt instantaneously within one time step and form cloud droplets or aggregates if it is brought into areas where temperatures exceed the freezing point. The changes in mass content can be described by:

$$\begin{aligned} MIq &= q_{pi} \\ \Delta q_{pc} &= +MIq \quad \text{and} \quad \Delta q_{pi} = -MIq. \end{aligned} \quad (55)$$

For the related tendencies in number concentration we get:

$$\begin{aligned} MIN &= N_{pi} \\ \Delta N_{pc} &= +MIN \quad \text{and} \quad \Delta N_{pi} = -MIN. \end{aligned} \quad (56)$$

Melting of graupel is achieved by heat transfer through heat-conduction, water vapour diffusion and accretion of cloud or rain water (*Mason, 1956*). We assume that the particle radius is constant during melting. That implies that we neglect the effect of meltwater loss by shedding or evaporation with regard to the heat balance. The mass loss by melting of an individual graupel particle, neglecting heat transfer by accretion, is given by:

$$\frac{\partial}{\partial t} m_{ph} = \frac{4\pi r_{ph} C_v}{L_f} \left(K_a \Delta T - L_v D_v \frac{\rho_g}{q_g} \Delta q_v \right) \quad (57)$$

with the deviation from the freezing temperature $\Delta T = T - T_0$ and the deviation from the saturation water vapour content in air $\Delta q_v = q_v - q_{sat}$.

The ventilation coefficient C_v is given in Eq. (27) and Eq. (28). We have to integrate over the size distribution of graupel:

$$\int_0^{\infty} \frac{\partial}{\partial t} m_{ph} dr_{ph} = \int_0^{\infty} \frac{4\pi r_{ph}}{L_f} A \left(1 + V_p r_{ph}^{\frac{3}{4}} \right) N(r_{ph}) dr_{ph} \quad (58)$$

$$\text{where } A = \left(K_a \Delta T - L_v D_v \frac{\rho_g}{q_g} \Delta q_v \right)$$

including the effect of the accretion of liquid water we obtain:

$$\begin{aligned} MHq &= \frac{4\pi}{L_f} A N_{ph} \left(r_{n,h} \frac{\Gamma(\nu_h + 1)}{\Gamma(\nu_h)} + V_p r_{n,h}^{7/4} \frac{\Gamma(\nu_h + 7/4)}{\Gamma(\nu_h)} \right) \\ &+ \frac{C_{p,wat}}{L_f} \Delta T (f_c ACHCq + f_r ACHRq) \end{aligned} \quad (59)$$

where $C_{p,w}$ is the specific heat capacity of water. The change in mass content of rain and graupel is then given by:

$$\frac{\partial}{\partial t} q_{pr} = +MHq \quad \text{and} \quad \frac{\partial}{\partial t} q_{ph} = -MHq. \quad (60)$$

Melting graupel consists of an ice core that is surrounded by meltwater. Depending on the fall velocity and the diameter of the ice spheres one can distinguish between different melting modes (*Rasmussen et al.*, 1984), however the whole phenomenon of melting and shedding is not well quantified at the moment. It has been observed that ice particles shed their meltwater if they are larger than about 4.5 mm in radius (*Rasmussen et al.*, 1984). Melting graupel, as well as rain drops, get instable due to hydro-dynamical imbalances if they exceed this limit size. In addition, the fraction of meltwater water must be larger than a critical value of about 20 % of the particle mass. The radius of drops resulting from meltwater shedding from hail or graupel is observed to be in the range of 0.25 and 1 mm with a 0.5 mm modal size (*Rasmussen et al.*, 1984; *Rasmussen and Heymsfield*, 1987, among others).

For simplicity, we assume in our simulation that the liquid water resulting from melting of graupel will be completely shed and transferred to rain. The number concentration of drops is determined by assuming that the shed size is $r_{shed} = 0.5 \text{ mm}$, but not larger than the volume mean graupel radius, \bar{r}_h .

$$MHn = \frac{MHq}{\rho_w \frac{4}{3} \pi \min(r_{shed}, \bar{r}_h)^3} \quad (61)$$

where ρ_w is the density of liquid water. The number concentration of graupel does not change during melting, except for total melting of pure graupel that is unpolluted with volcanic ash.

The tendencies in number concentrations due to melting are then given by:

$$\frac{\partial}{\partial t} N_{ph} = 0 \quad \text{and} \quad \frac{\partial}{\partial t} N_{pr} = +MHn. \quad (62)$$

For the parameterisation of heterogeneous freezing of supercooled water, we follow the stochastic hypothesis of *Bigg* (1953) and *Barklie* (1959). After integrating over the size distribution, we get the change in number concentration due to freezing of drops with the radius r :

$$\begin{aligned} FRXn &= \int_0^{\infty} N(r_{px}) \frac{4}{3} \pi r_{px}^3 \frac{\rho_0}{\rho_g} B' \left(e^{A'(T_0-T)} - 1 \right) dr_{px} \\ &= \frac{4}{3} \pi \frac{\rho_0}{\rho_g} B' \left(e^{A'(T_0-T)} - 1 \right) N_{t,px} r_{n,px}^3 \frac{\Gamma(\nu_{px} + 3)}{\Gamma(\nu_{px})} \end{aligned} \quad (63)$$

$$\text{where} \quad A'=0.66 K^{-1} \quad \text{and} \quad B'=100 m^{-3} s^{-1}.$$

Freezing does not change the total number concentration of the particles involved, but the particles change from a liquid to a frozen category. The change in number concentration is given by:

$$\begin{aligned} \frac{\partial}{\partial t} N_{ph} &= +FRRn \quad \text{and} \quad \frac{\partial}{\partial t} N_{pr} = -FRRn, \\ \frac{\partial}{\partial t} N_{pi} &= +FRCn \quad \text{and} \quad \frac{\partial}{\partial t} N_{pc} = -FRCn. \end{aligned} \quad (64)$$

In order to get the mass change due to statistical freezing of cloud and rain water, we have to multiply by droplet mass:

$$\begin{aligned} FRXq &= \int_0^{\infty} \left(\frac{4}{3} \pi r_{px}^3 \right)^2 \frac{\rho_0}{\rho_g} \rho_w B' \left(e^{A'(T_0-T)} - 1 \right) N(r_{px}) dr_{px} \\ &= \left(\frac{4}{3} \pi \right)^2 \frac{\rho_0}{\rho_g} \rho_w B' \left(e^{A'(T_0-T)} - 1 \right) N_{t,px} r_{n,px}^6 \frac{\Gamma(\nu_{px} + 6)}{\Gamma(\nu_{px})}. \end{aligned} \quad (65)$$

We obtain for the tendencies of mass content due to freezing:

$$\begin{aligned} \frac{\partial}{\partial t} q_{ph} &= +FRRq \quad \text{and} \quad \frac{\partial}{\partial t} q_{pr} = -FRRq, \\ \frac{\partial}{\partial t} q_{pi} &= +FRCq \quad \text{and} \quad \frac{\partial}{\partial t} q_{pc} = -FRCq. \end{aligned} \tag{66}$$

The sources and sinks of tracers due to microphysics are summarized in the appendix.

3.11 Thermodynamic Effects of Phase Changes

All microphysical processes that include a phase change in water consume or produce thermal energy, this way influencing the dynamics of the entire system. For the processes discussed above, the potential temperature, Θ , of the gas-particle-mixture is changed by:

$$\begin{aligned} \frac{\partial}{\partial t} \Theta &= \frac{L_v}{c_p} (CEC + CER + CEMH + NCq) \\ &+ \frac{L_s}{c_p} (NIq + SDI + SDH) \\ &+ \frac{L_f}{c_p} (f_c ACHCq + f_r ACHRq(T < T_0) + f_r ACIRq(T < T_0) \\ &\quad - f_i XMIq - f_h XMHq + f_c FRCq + f_r FRR) \end{aligned} \tag{67}$$

where c_p is the specific heat capacity of the gas-particle-mixture.

A balance procedure guarantees mass conservation and ensures that the phase transfer of water vapour is confined to the existing super- or sub-saturation.

3.12 Salinity Effects

The dissolution of gases changes the thermodynamic properties of water: the solution's saturation vapour pressure and freezing temperature will be lowered when compared to that of pure water (*Levine, 1995*). In an ideal diluted solution, these effects are only dependent on the mole fraction x_i of the species i and not on the solute's chemical nature. According to Raoult's law the saturation pressure of water vapour over an ideal solution droplet is given by:

$$p_{sat,l} = p_{sat,w}^o \cdot \left(1 - \sum_{i=1}^n x_i\right) \quad (68)$$

where $p_{sat,w}^o$ and $p_{sat,l}$ are the saturation vapour pressure of pure water and the solution, respectively. We get for the freezing point depression:

$$T_f = T_f^o \cdot \left(1 - T_f^o \frac{R}{\Delta H_f} \sum_{i=1}^n x_i\right) = T_f^o \cdot \left(1 - k_f \sum_{i=1}^n x_i\right) \quad (69)$$

where $k_f = 0.38 \text{ K}$. $T_f^o = 273.15 \text{ K}$ and T_f are the freezing point of pure water and the solution, respectively. $R = 8.3143 \text{ J/mol K}$ is the general gas constant and $\Delta H_f = 6007 \text{ J/mol}$ the molar enthalpy of freezing. The lowering of the freezing point is limited to the liquidus of HCl solutions, $T_{f,min} = 198.45 \text{ K}$ (*Thibert and Dominé, 1997*) in our simulations.

The droplets in a volcanic eruption column are contaminated with gases and salts of highly indefinite qualities and quantities (see for example *Mackinnon et al., 1984*; *Smith et al., 1982*). These electrolyte solutions cannot be regarded as ideal, because of long-range inter-ionic forces, that influence the actual concentrations of the solutes and of the water itself. The actual concentrations in a solution can be larger or even smaller, due to the formation of ion-pairs, than the ideal value. There are sophisticated thermodynamic models that treat intermolecular and inter-ionic interactions in a solution in order to determine the key parameter of real solutions, the activity coefficient. For a review see for example *Kim and Seinfeld (1993)* or *Carslaw et al. (1997)*. The properties of multicomponent solutions cannot be predicted a priori at any concentration, but are derived from highly simplified views and contain empirical parameters. With the major uncertainties concerning the droplet composition in volcanic plumes, the determination of the activity coefficients is even more problematic. Hence, the droplets in our model are assumed to behave like ideal solutions in order to obtain a first estimate of the salinity effect.

Theory and observations indicate the saturation vapour pressure of polluted ice particles to be substantially reduced, for references see *Chen and Crutzen (1994)*.

The special properties of ice surfaces have led to the imagination of a quasi-liquid layer at the ice particle's surface. The existence of such a layer was already proposed by *Faraday* (1859) to explain the adhesive properties of ice, however, there are still great uncertainties in its characteristics. The thermodynamic properties, like electrical conductivity, structure and viscosity, are found to be between that of water and bulk ice. The thickness of the layer increases with temperature and ionic content of the ice, for a short review see *Pruppacher and Klett* (1997) or *Santachiara et al.* (1998). *Conklin et al.* (1993) estimated the layer thickness to range from 3 nm at -60°C to 500 nm at -1°C for ice made from distilled water. Hence, a comprehensive characterisation of saturation vapour pressure depression of polluted ice is even more difficult than for aqueous solutions. In addition, there are certainly interactions of different ions that further complicate a quantitative description. In the framework of this research, the salt effects of ice particles are therefore characterised through the formulations for ideal water solutions described above.

The salinity effect is examined in Sect. (6.4.2), it does not show a substantial depression of the saturation water pressure and the freezing point of droplets in volcanic eruption plumes.

4 Scavenging of Volcanic Gases

4.1 Scavenging by Liquid Droplets

4.1.1 Phase Equilibrium

The physical solubility of an arbitrary gas, HA , in water is described by the Henry coefficient He :

$$He = \frac{[HA]_{aq}}{[HA]_g} \quad (70)$$

where the parenthesis indicate the species concentration in the gas and water phase, g and aq , respectively. Within the context of this work, all concentrations are given in terms of $[mol/kg_{tot.mass}]$. In these units the Henry coefficient He increases with increasing liquid water content. It refers to the pure physical solubility equilibrium of a gas in water, regardless of its subsequent fate in the droplet. However, acidic gases undergo acid-base reactions like $HA \rightleftharpoons A^- + H^+$ described by the dissociation constant K_s :

$$K_s = \frac{[A^-]_{aq} \cdot [H^+]_{aq}}{[HA]_{aq}} \quad (71)$$

The dissociation reaction in the liquid phase enhances the uptake of gases in droplets. The total solubility – given by the effective Henry coefficient He^* – is then also a function of the pH-value:

$$He^* = \frac{[HA]_{aq} + [A^-]_{aq}}{[HA]_g} = He \cdot \left(1 + \frac{K_s}{[H^+]}\right) \quad (72)$$

Corresponding expressions are valid for two protonic acids like H_2S and SO_2 .

All equilibrium constants are temperature dependent according to the van't Hoff equation (see e.g. *Wedler*, 1987):

$$K = K_{\ominus} \cdot \exp\left(\frac{\Delta H}{R} \left(\frac{1}{T} - \frac{1}{T_{\ominus}}\right)\right) \quad (73)$$

The Henry coefficients generally increase as the temperature decreases, reflecting a greater solubility at lower temperatures. The reaction enthalpy, ΔH , is the energy change involved with dissolution of gases in water and $T_{\ominus} = 289 K$ is the reference temperature for the values of the Henry coefficients and the acidity constants, K_{\ominus} , which are taken from *Sander* (1994).

At room temperature and a pH-value of 2 we get effective Henry coefficients of $1.9 \cdot 10^4$, 3.0 and 0.1 for HCl, SO₂ and H₂S (here given in [mol/l atm]), respectively. The water solubility of HCl is about four orders of magnitude higher than that of the sulphur containing gases. Hence, this gas is likely to be completely scavenged by water drops, its revolatilisation would require a drastic decrease of the system's liquid water content.

4.1.2 Kinetics of the Phase Transfer

The time scales to adjust to phase equilibrium are on the order of a fraction of a second for the dissolution of slightly soluble gases. However, highly soluble gases need much longer times. The time to establish phase equilibrium increases with drop radius and liquid water content. The characteristic times needed to achieve the Henry's law equilibrium (including subsequent dissociation reaction inside the droplets) are long when compared to the model time step, of about half a second simulation time in ATHAM, especially for HCl. Hence, we have to consider the time dependency of phase transfer.

The overall process of the phase transfer of a reactive species can be divided into the following sub-processes (*Schwartz, 1986*):

- gas phase mass transport to the air-water interface;
- mass transport across the interface and possible establishment of the solubility equilibrium locally at the interface;
- establishment of rapid aqueous phase equilibria (e.g. acid-base reactions);
- aqueous phase mass transport inside the drop;
- aqueous phase chemical reactions;
- mass transport of reaction products in the aqueous phase;
- mass transport across the interface and release of product into the gas phase;
- gas phase mass transport of the species.

There are various theoretical formulations for the time dependence of gas scavenging by liquid droplets used in atmospheric modeling. A brief summary of the different concepts is given below.

The simplest approach was used in older investigations: all cloud and rain drops were assumed to be in Henry's equilibrium with the ambient gases (e.g. *Gravenhorst et al.*, 1978).

A more detailed approach, called the 'two-film-model' presumes that the resistance to phase transfer is confined to two boundary layers at the surface, one outside and one inside the drop (*Barrie*, 1978). Apart from these two layers, complete mixing of the species is expected. The possible resistance to mass transfer across the phase boundary is not taken into account. However, the applicability of the idea is limited, because the thickness of the boundary layer is a priori not known and is not constant during the increase of the solute concentration inside the drop.

The most elaborated idea employs the complete convective diffusion equation that describes the transport of a gas through moving air to and into a circulating drop falling at terminal velocity (*Walcek et al.*, 1984). Again, the resistance to interfacial mass transport was not taken into account. This detailed theory was simplified by applying the suggestion of *Kronig and Brink* (1950) and *LeClair et al.* (1972): they assume for small drops (radius $\leq 500 \mu\text{m}$) with a laminar flow-pattern of the internal circulation – the Stokes-flow approximation – that the transport of the solute takes place only perpendicular to the streamlines. In the so-called 'fully-mixed-model' for larger drop sizes, *Walcek et al.* (1984) suggested complete turbulent mixing inside the drop: the resistance to phase transfer is only restrained to gas phase diffusion, again neglecting interfacial resistance. For drops larger than $500 \mu\text{m}$ in radius the internal circulation oscillates between complete turbulent mixing and an organized Stokes-flow regime. This has been shown experimentally by *LeClair et al.* (1972); *Pruppacher and Beard* (1970); *Diehl* (1989). The fully-mixed-model and the Kronig-Brink approach were compared with experimental results for the scavenging of different atmospheric gases by droplets of various size (*Mitra et al.*, 1992; *Hannemann et al.*, 1995). It was shown that the validity of the fully-mixed-model is restricted also for large drops, when chemical reactions occur in the liquid phase leading to a more complex behaviour.

The interfacial mass transfer – that has not been considered by the approaches described above – is basically a process involving individual molecules, thus, it is described by the kinetic gas theory. The fraction of molecules impinging at the drop's surface that are successfully incorporated into the drop is given by the sticking coefficient α . The data available from the literature vary considerably for this parameter since it is extremely difficult to measure. *Schwartz* (1986) indicated that interfacial mass transfer is not very important for atmospheric applications compared to other sub-processes, as long as $\alpha \geq 0.01$, which is the case under most circumstances.

In the framework of this survey, we assume that the characteristic phase transfer time of gases into the liquid phase, and vice versa, is dominated by gas phase diffusion and interfacial mass transfer. For simplicity we suppose that the droplets are internally well mixed and that rapid dissociation equilibria in the aqueous phase are instantaneously reached. We neglect any other liquid phase reactions.

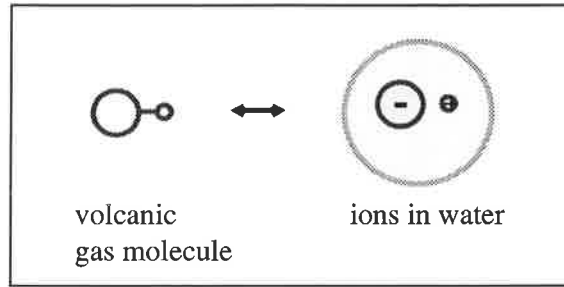


Figure 5: Scheme of gas scavenging by liquid droplets.

A further simplification is achieved by applying the steady state approximation: species concentrations, fluxes and reaction rates are no longer a function of time during one model time step (*Schwartz, 1986*). The phase transfer rate of volatiles into liquid droplets with subsequent dissociation reactions of acidic gases in the liquid phase is then proportional to the deviation from the solubility equilibrium:

$$\frac{\partial}{\partial t} c_{aq} = -\frac{1}{L} \frac{\partial}{\partial t} c_g = k_t (c_{g,\infty} - c_{g,eq}) \quad (74)$$

where $c_{aq} = [HA]_{aq} + [A^-]_{aq}$ is the total concentration in the aqueous phase and $c_{g,eq} = [HA]_g$ denotes the concentration in the gas phase at the drops' surface, given by the effective Henry constant in Eq. (72). $c_{g,\infty}$ is the gaseous concentration in the undisturbed environment and L in $[kg_{aq}/kg_{tot.mass}]$ the liquid water content.

The phase transfer constant k_t in $[s^{-1}]$ is defined as the reverse sum of the characteristic times of mass transport of a gas to the drop surface, τ_{dg} , and that across the air-water interface including the possible establishment of solubility equilibrium locally at the interface, τ_i , and vice versa (*Schwartz, 1986*).

$$k_t = (\tau_{dg} + \tau_i)^{-1} = \left(\frac{r^2}{2D_g} + \frac{4r}{3\bar{v}\alpha} \right)^{-1} \quad (75)$$

$$\text{where } D_g = \lambda \bar{v}$$

$$\text{and } \bar{v} = \sqrt{\frac{8RT}{M\pi}} \quad (76)$$

where r is the volume mean radius of the particle in m , D_g the gas phase diffusion coefficient in m^2/s . \bar{v} denotes the mean speed of gas molecules from the kinetic gas theory in m/s , $R = 8.3143 \text{ mol/KJ}$ is the general gas constant, M in kg/mol the molecular weight and λ in m the mean free path in air.

The sticking coefficients $\alpha_{\text{HCl}} = 0.2$ and $\alpha_{\text{SO}_2} = 0.11$ are taken from *DeMore et al.* (1997). The value for H_2S was estimated ($\alpha_{\text{H}_2\text{S}} = 0.1$) to be in the range of the other values, because no observational data are available.

In the case of falling drops, we have to take into account the effect of turbulence caused by circulation around the moving drop. This is done by applying the ventilation coefficient C_v , we already used for the phase transfer of water vapour in Eq. (27). We get for the diffusion coefficient D_g^* which includes the effects of turbulence:

$$D_g^* = D_g \left(1. + 0.22 Re^{1/2} \right). \quad (77)$$

This coefficient is then applied in Eq. (75) instead of D_g .

4.1.3 Numerical Treatment of Gas Scavenging by Liquid Drops

We get the following chemical rate expressions describing the simultaneous dissolution of gases including their subsequent dissociation in the liquid phase:

$$\frac{\partial}{\partial t} c_{c,i} = k_{t,c,i} c_{g,i} - k_{t,c,i} \frac{c_{c,i}}{He_{c,i}^*}, \quad (78)$$

$$\frac{\partial}{\partial t} c_{r,i} = k_{t,r,i} c_{g,i} - k_{t,r,i} \frac{c_{r,i}}{He_{r,i}^*}, \quad (79)$$

$$\frac{\partial}{\partial t} H_c^+ = f(c_{c,1}, c_{c,2}, \dots, c_{c,n}), \quad (80)$$

$$\frac{\partial}{\partial t} H_p^+ = f(c_{r,1}, c_{r,2}, \dots, c_{r,n}), \quad (81)$$

$$\frac{\partial}{\partial t} c_{g,i} = -L \left(\frac{\partial}{\partial t} c_{c,i} + \frac{\partial}{\partial t} c_{r,i} \right). \quad (82)$$

$c_{c,i}$, $c_{r,i}$, $c_{g,i}$ are the total concentrations in $[mol/kg_{tot.mass}]$ of the species $i = 1, 2, \dots, n$ in cloud and rain water, and in the gas phase, respectively. $k_{t,c,i}$ and $k_{t,r,i}$ are the corresponding phase transfer coefficients. The effective Henry constants $He_{c,i}^*$ and $He_{r,i}^*$ for each species are coupled with the concentrations of the dissolved

acid species via the proton concentrations H_c^+ and H_r^+ in clouds and rain, respectively. Because of mass conservation, the concentration change of a species in the gas phase is obtained from its changes in the liquid phases, L is the liquid water content.

The resulting set of stiff non-linear equations is solved by employing an implicit time stepping procedure:

$$c^{n+1} = c^n + \Delta t f(c^{n+1}) \quad (83)$$

with the n_{th} time step Δt . c denotes the species concentration ($c_{g,i}$; $c_{c,i}$; $c_{r,i}$; H_c^+ and H_r^+), and f are the time derivatives given in Eq. (78) to Eq. (82). $f(c^{n+1})$ can be linearized by using a Taylor expansion with truncation after the first term as in Newton's method (*Press et al.*, 1992) which gives the following expression:

$$c^{n+1} = c^n + \Delta t \left(f(c^n) + \mathbf{J}^n (c^{n+1} - c^n) \right) \quad (84)$$

The Jacobian matrix \mathbf{J} includes the partial derivatives of each species with respect to all others species of the system. Eq. (84) was iteratively solved with a very efficient realisation of a Gauss elimination (*Oberhuber*, 1996).

4.2 Scavenging by Ice Particles

4.2.1 Incorporation of Gases into Ice

Recently, field studies and a number of laboratory experiments indicated that ice crystals are able to scavenge gaseous species from the surrounding air, for references see *Diehl et al.* (1998). The solubility of gases in ice is much lower than in liquid water, since ions are rejected by the ice matrix. The gas uptake is dependent on the type of gas, temperature and crystalline structure of the ice. In addition, gas uptake is different for growing and non-growing ice (*Pruppacher and Klett*, 1997). It has been observed that the contamination of ice does not correspond to the thermodynamic equilibrium solubility of chemical species in ice.

Among others, *Valdez and Dawson* (1989); *Mitra et al.* (1992); *Diehl* (1995); *Diehl et al.* (1995); *Thibert and Dominé* (1997) performed laboratory experiments in order to investigate the uptake of gases by ice crystals. The experiments indicated that the diffusivities of electrolytes in ice are very low compared to liquid water values. Species once incorporated in ice will not be able to considerably

change their position within the crystal. Thus the phase equilibrium cannot be established after the initial gas incorporation within the time period of the simulation with ATHAM (about 1 hour). *Diehl* (1995) found that the HCl uptake of non-growing ice is much larger than that of a growing ice surface. The author suggested that the amount of incorporation during ice growth is determined by the number of vacancies and other defects in the crystal lattice. In case of non-growing ice, the accumulation of dissolved gases might induce surface melting due to freezing point depression. At temperatures near the freezing point, the absorption on ice surfaces seems to become more efficient due to a quasi-liquid layer, see Sect. (3.12). In the presence of a quasi-liquid layer, the incorporation of gases into ice might be a multi-step process (*Petrenko*, 1994) comparable to that of gas transfer to liquid drops as mentioned previously. Freezing point depression caused by dissolved species increases the layer extent. This may explain the observed enhanced gas-uptake-capacity of the thicker quasi-liquid layer of non-growing ice. At temperatures too low for the quasi-liquid layer to exist, the uptake of gases by ice tends to increase with decreasing temperature (*Santachiara et al.*, 1998).

Inside a rising volcanic plume, most of the ice particles are likely to grow continuously due to supersaturation in the lifted air masses. It has experimentally been shown (e.g. *Dominé et al.*, 1995; *Diehl*, 1995) that the incorporation of gases during ice growth is ruled by condensation kinetics. The mass of the incorporated species is proportional to the mass of water vapour converted to ice. The simulation of gas scavenging by ice particles in ATHAM is performed by employing the ideas of *Dominé et al.* (1995); *Dominé and Thibert* (1996). These authors suggested that the species concentration in ice is determined by the ratio of the number of molecules n_c to that of n_{H_2O} that hit and stick to the ice surface. This is given by:

$$x_i = \frac{n_c \alpha_c}{n_{H_2O} \alpha_{H_2O}} \frac{\bar{v}_c}{\bar{v}_{H_2O}}. \quad (85)$$

where α denotes the sticking coefficient and \bar{v} the mean speed of gas molecules from the kinetic gas theory given in Eq. (76). The low diffusion constant of electrolytes in ice prevents volcanic volatiles once incorporated into ice crystals from reevaporation.

It has been observed, for example, that the concentration of HCl in Greenland snow was orders of magnitude lower than the equilibrium value. However, it was consistent with kinetic considerations because of the low rate of water vapour deposition. On the other hand, the high growth rate of ice in the buoyant volcanic plume might lead to concentrations in the ice phase that are higher than the solubility equilibrium. Correspondingly, *Thibert and Dominé* (1997) assumed based on their theoretical considerations, that ice particles in cirrus and aircraft

condensation trails can trap amounts of HCl well above the equilibrium saturation limit.

The time dependent change of a chemical species due to incorporation into ice crystals is proportional to the amount of water vapour being transferred during a time step Δt , which is calculated in the microphysical module. Using the expressions for the mean gas speed \bar{v} given in Eq. (76) we get:

$$\frac{\partial}{\partial t} c_i = - \frac{\partial}{\partial t} c_g = \frac{\partial}{\partial t} q_i \frac{c_g}{q_v} \frac{\alpha_c}{\alpha_{H_2O}} \sqrt{\frac{M_{H_2O}}{M_c}} \quad \text{for incorporation} \quad (86)$$

where c_i and c_g are the contents of chemicals in ice and in the gas phase in $mol/kg_{tot.mass}$, respectively. q_i and q_v denote the specific contents of ice and water vapour in $kg/kg_{tot.mass}$. The sticking coefficient $\alpha_{HCl} = 0.3$ is taken from *DeMore et al.* (1997). For SO_2 and H_2S we assume the same values as for liquid water, $\alpha_{SO_2} = 0.11$ and $\alpha_{H_2S} = 0.1$, because no observational data are available. We apply for water vapour $\alpha_{H_2O} = 1$. In the context of this work, we neglect the temperature dependence of α . Considering the poor data basis, the sticking coefficients applied in our simulations may hold for a first investigation of the significance of gas incorporation into ice particles. The efficiency factor $f_{inc,c}$:

$$f_{inc,c} = \frac{\alpha_c}{\alpha_{H_2O}} \sqrt{\frac{M_{H_2O}}{M_c}} \quad (87)$$

is for HCl $f_{inc,HCl} = 0.21$, for SO_2 $f_{inc,SO_2} = 0.06$ and for H_2S $f_{inc,H_2S} = 0.07$, respectively. Hence, HCl will be most effectively incorporated into ice particles.

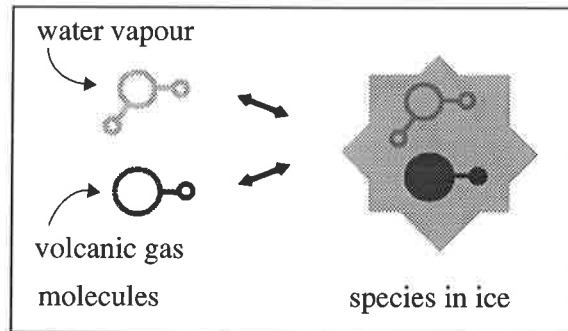


Figure 6: Scheme of gas scavenging by frozen hydrometeors.

4.2.2 Release of Gases from Ice

Diehl et al. (1995) observed in laboratory experiments during the sublimation of polluted ice, that pure water vapour is transferred to the gas phase at first, leading to increased concentrations of dissolved species in the remaining hydrometeor. After reaching a critical contamination, simultaneous sublimation of water vapour and dissolved chemicals occurs. However, no quantitative information of this process is available. Probably, the release of solutes depends on the rate of water vapour transfer. There might be no time to build up an accumulation zone during fast sublimation, instead, solutes and water vapour leave the ice crystal simultaneously. In the context of this work, we adopt the fraction of chemicals released to the gas phase to be proportional to that of sublimating water vapour. For consistency, the amount of released gases is weighted with the inverse of the factor applied in the gas incorporation equation Eq. (86). The tendency of the species concentration caused by release of gases from ice particles is given by:

$$\frac{\partial}{\partial t} c_g = - \frac{\partial}{\partial t} c_i = \frac{\partial}{\partial t} q_v \frac{c_i}{q_i} \frac{\alpha_{H_2O}}{\alpha_c} \sqrt{\frac{M_c}{M_{H_2O}}} \quad \text{for release.} \quad (88)$$

4.3 Transfer of Solutes during Microphysical Processes

Coagulation of different hydrometeor classes leads to a mixture of the original solutions, thus producing new droplets or ice particles with average species concentrations.

Different studies about the retention coefficients for gases in water during freezing of the solution delivered different results. *Iribarne and Pyshnov* (1990) demonstrated experimentally that during freezing of liquid droplets some highly soluble chemical species, among them HCl, are totally retained in the ice phase. *Iribarne et al.* (1990) found that S(IV) dissolved in droplets is partially evolved as SO₂ during freezing, the retention of S(IV) increases with increasing growth rate of the ice particles. In a volcanic eruption column, liquid droplets experience a strong temperature decrease because of the quick ascent (about 100 m/sec) leading to rapid drop freezing. Hence, in ATHAM we assume that the total amount of the chemicals contained in the liquid phase is shifted into the ice phase during droplet freezing. Vice versa, the species previously contained in the ice phase are completely transferred into the liquid phase during ice melting.

The time dependent change of the specific content c_x in $mol/kg_{tot.mass}$ of a chemical species contained in a hydrometeor q_x in $kg/kg_{tot.mass}$ is assumed to be proportional to that of the hydrometeor. It is calculated from the sum over the

microphysical processes involved with the particular hydrometeor type x under consideration:

$$\frac{\partial}{\partial t} c_x = \sum_{procs} \frac{c_x}{q_x} \left(\frac{\partial}{\partial t} q_x \right). \quad (89)$$

Condensation of water vapour on liquid hydrometeors leads to dilution of the solutions; evaporation of water drops causes an increase of the concentration. At the same time, the phase transfer kinetics of chemical species works towards a phase equilibrium. Total evaporation releases the species back into the gas phase, neglecting a possible aerosol formation due to the crystallisation of salt particles. The treatment of incorporation and resublimation of chemicals into ice particles during their growth has been shown in Sect. (4.2).

The processes included in the scavenging module guarantee that volcanic species, initially erupted at the vent as gases, can be contained in each class of hydrometeor. Once scavenged, they experience all microphysical processes shown in Fig. (3). In the framework of this study, we do not consider the adsorption of volcanic gases on dry ash. The information about the surface area of volcanic particles and about the sticking probabilities of gases on ash are too speculative at the moment and will be the subject of future research.

4.3.1 Limit Solubility

The real solubility of highly soluble electrolytes does not obey Henry's law that is strictly true only for ideal solutions. The concept of activity coefficients – not considered in this study, as mentioned in Sect. (3.12) – deals with this problem. The solubility converges to saturation when the solute concentration increases, especially for large gas/liquid-water ratios. Hence, SO_2 and H_2S being only slightly soluble in water follow the Henry law more accurately than HCl . At the concentrations occurring in a volcanic plume the gases are not likely to reach their solubility limit in the droplets, apart from locations which have extremely low liquid water content and high species partial pressure. However, these few places are not important for the overall scavenging ratio in the plume. We only have to make sure that we do not obtain unreasonable high solution concentrations. The saturation solubility of gases in water increases with decreasing temperature as shown in Fig. (7) for a pure aqueous HCl solution at a HCl -pressure of 1 atm.

The saturation solubility of HCl is always higher than 10 mol/l. We performed a quadratic fitting to the data given in *Gmelin and Pietsch* (1926) and got the following equation for the temperature dependence of the saturation concentration of HCl :

$$C_s = 1.609 \cdot 10^{-4} T^2 - 5.3 \cdot 10^{-2} T + 12.6 \quad (90)$$

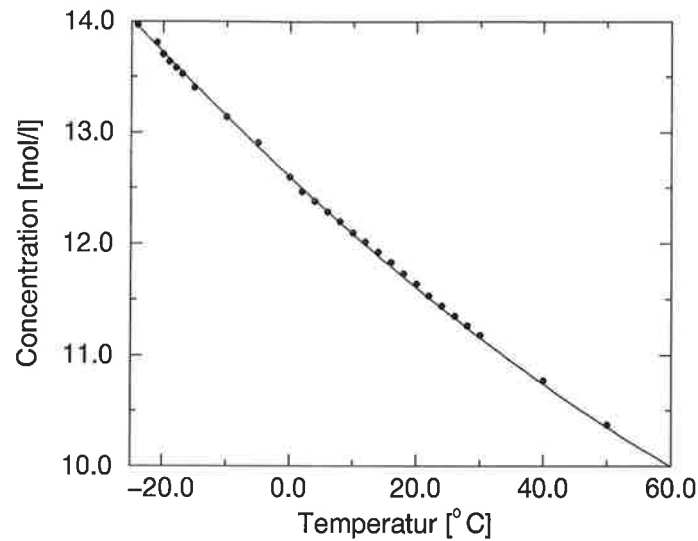


Figure 7: Maximum solubility of HCl gas as a function of temperature.
Dots: data taken from *Gmelin and Pietsch* (1926), solid line: fitting curve

where C_s is given in [mol/l], the temperature T in [°C] and related units of the constant factors. The species concentration in hydrometeors is not allowed to exceed this saturation limit. For simplicity, this concept is also applied for solid hydrometeors and for the sulphur species (which are not likely to ever reach this limit).

5 The Plume Model ATHAM

The numerical model ATHAM (Active Tracer High Resolution Atmospheric Model) is designed to simulate the mesoscale evolution of an explosive volcanic plume in the atmosphere. The model concept facilitates to easily connect additional tracers and modules of different focus and complexity. At the moment, the model consists of five modules:

- The dynamic part solves the Navier-Stokes equation for the gas-particle-mixture and includes the transport of active tracers (*Oberhuber et al.*, 1999; *Herzog*, 1998).
- The turbulence closure scheme delivers the turbulent exchange coefficients for each dynamic quantity, thereby describing the entrainment of ambient air into the plume (*Herzog*, 1998; *Oberhuber et al.*, 1999).
- The cloud microphysics describes condensation of water vapour and formation of precipitation. All phases of water are included: vapour, liquid and solid. The feedback of the of thermal energy changes on the dynamics is considered (*Graf et al.*, 1999; *Herzog et al.*, 1999, new version: this work).
- The ash module describes particle growth and coagulation based on microphysical interactions between hydrometeors and ash (this work).
- The scavenging module calculates dissolution of volcanic gases into droplets and the incorporation of volatiles into ice particles. The redistribution of species contained in hydrometeors due to microphysical processes is included (this work).

The model is formulated in three dimensions with an implicit time stepping scheme. The conservation of mass and momentum is explicitly guaranteed by applying the flux form for the equations of motion and continuity of the tracers. Because of computer restrictions, only two dimensions are used at present. Two different two-dimensional versions are implemented: one in cartesian and one in cylindrical coordinates; the latter is employed in this study. No cross wind effects can be studied in cylindrical coordinates, but the dilution of the mixture by entrainment of surrounding air corresponds better to the three dimensional case than the cartesian version (*Herzog*, 1998).

The simulations in this study are performed on a stretched lattice with 127×127 grid points. The model domain is 150 km in the horizontal and 50 km in the vertical direction. In the center of the model domain we use a spatial resolution of 100 m, at the lateral boundaries it is about 5 km. This grid choice permits the simulation of the full plume development with restricted computer resources

without disturbances from the model boundaries for a simulation time of one hour. An arbitrary orography, i.e., shape and height of a volcano, can be defined at the lower boundary.

ATHAM is initialized with profiles for horizontal wind, temperature, relative humidity and gaseous species in the background atmosphere. The input of volcanic material during the eruption is specified by defining additional vertical velocities, temperature and composition of the ejecta at three vent grid points. However, in this survey the spatial grid resolution at the vent is coarser than the size of a real vent. Hence, a scaling procedure by a factor of three (*Herzog, 1998*) was carried out: the volcanic ejecta are diluted with dry air before starting the model simulation. The fluxes of momentum, thermal energy and mass for particles and gases erupted at the vent are conserved. This implies that the simulation begins just after the earliest mixing of the erupting gas-particle-mixture with the atmosphere, small scale processes in the vicinity of the crater in the hot temperature regime are not resolved in the concept of ATHAM. We focus on processes occurring in the plume in the range of about hundred meters to some tens of kilometers. The results of a simulation performed with higher spatial resolution and realistic forcing differs only slightly from that with a coarser grid and scaled forcing; the principal mesoscale plume behaviour is similar (*Herzog, 1998*).

Volcanic ash particles occur typically in mass fractions greater than 95% in volcanic plumes. They can no longer be transported as passive tracers with the mean flow as in usual atmospheric models, but their impact on the dynamics of the system has to be considered. In the non-hydrostatic model ATHAM, particles are treated as active tracers: they can occur in any concentration and they can influence the dynamics of the system by contributing to the mixture density, pressure and heat content. In general, the description of such a multicomponent system of active tracers requires a set of dynamic and thermodynamic equations for each component including the interactions between them. Detailed models employing this approach have been developed by *Valentine and Wohletz (1989)*, *Dobran and Neri (1993)* and *Neri and Macedonio (1996)* for up to three components. However, the consideration of a higher number of grid points for investigating the mesoscale evolution of the plume, and the treatment of higher numbers of tracers is not possible with this concept.

Two main ideas are applied in ATHAM to circumvent the problem of dealing with a very large equation system (*Oberhuber et al., 1999*):

- Dynamic equilibrium: we assume instantaneous exchange of momentum between particles and gas. All particles move with their terminal velocity relative to the mixture, which allows for the description of sedimentation.

-
- Thermal equilibrium: tracers can act as a source of heat, but we expect the system to exchange heat instantaneously, the in situ temperature of the volume mean being identical to the individual in situ temperature of each tracer.

Both assumptions require that the particles modeled are small. The grain sizes of volcanic particles considered in ATHAM are well inside the range of validity as shown by *Herzog* (1998); *Oberhuber et al.* (1999). The only restriction resulting from our assumptions is that the time resolution of the model must be large compared to the time needed to achieve both equilibria. The dynamical features of a volcanic eruption we simulate set a lower limit for the time step, which should be in the order of a second. On the other hand, the great advantage of applying both dynamic and thermal equilibrium is the strong reduction in the number of prognostic equations. The dynamic behaviour of the gas-particle-mixture can now be described by five equations predicting the three momentum components, heat and pressure for the mixture. For each tracer one additional transport equation concerning its specific fall velocity is taken into account. Active tracers and dynamical variables are coupled by the bulk density and the heat capacity of the mixture via the equation of state. Further diagnostic equations are used to account for the interactions between the tracers and to close the system of dynamic equations. For a complete description of the model equations see *Herzog* (1998) and *Oberhuber et al.* (1999).

The plume of a plinian eruption is characterised by a jet regime close to the vent and a plume regime above. The jet regime is dominated by the consumption of initial momentum and relatively lower turbulence and the plume regime is ruled by buoyancy forces. Initially, the bulk density of the erupted hot gas-particle mixture is much higher than that of the surrounding air. The entrainment of air reduces the density of the initial gas-particle-mixture and allows for the evolution of a convective plume. Furthermore, entrainment supplies additional water vapour which determines microphysical processes and results in latent heat release when it condenses. Turbulence is responsible for entrainment processes. Sub-scale eddies cannot be resolved by the model grid, however, they are described by a turbulence closure scheme (*Herzog*, 1998; *Oberhuber et al.*, 1999). ATHAM – being developed in recent years – has been successfully tested to simulate the dynamics of an explosive volcanic eruption (*Herzog*, 1998; *Oberhuber et al.*, 1999). The model has been employed to examine the effects of different environmental conditions (*Herzog et al.*, 1999; *Graf et al.*, 1999) and grain sizes (*Seyfried*, 1999) on the mesoscale plume evolution.

In the framework of this study, an improved module for the representation of cloud microphysics in the plume has been developed. The interaction between hydrometeors and volcanic ash has been implemented considering the formation

of hydrometeor-ash aggregates that lead to more realistic sedimentation features. In addition, the eruption of volcanic gases at the vent and their scavenging by hydrometeors and aggregates has been included.

6 Numerical Simulations with ATHAM

6.1 Conditions of the Simulation

In the following chapter, we will present the results from numerical simulations with the plume model ATHAM. We do not try to simulate a specific volcano, but choose conditions typical for plinian eruptions. The first section deals with the general plume characteristics of an explosive volcanic event, focusing on the fate of tephra, volcanic gas and hydrometeors in the atmosphere. We investigate the effect of interactions between volcanic ash and condensed water leading to larger aggregates. In addition, the influence of the initial particle size distribution is examined. The second part of this chapter treats the behaviour of volcanic gases in the eruption column. We are interested in the scavenging ratio of HCl, SO₂ and H₂S by liquid droplets and ice particles in the plume. The consequences of ash-hydrometeor aggregation for the stratospheric injection of these gases are considered.

The volcano studied in the model was 1750 m high with a crater depth of 200 m. For the simulations presented here, we choose the following parameters to describe a typical plinian eruption (*Seyfried*, 1999). We give here the conditions before the scaling procedure:

- the crater diameter is 100 m,
- the vent exit velocity is 300 m/s,
- the vent temperature is 1000 K,
- and the gas mass fraction is 6 wt.%,
where water vapour contributes a fraction of 85 %.
- Two sizes of ash are erupted at the vent
with mean volume radii of $2.5 \mu\text{m}$ and $50 \mu\text{m}$
and a particle density of $\rho = 1500 \text{ kg/m}^3$.
(The composition of the erupting magma is varied in the sensitivity studies.)
- The density of the gas-particle-mixture is 3.2 kg/m^3
- and the ash mass eruption rate $7.05 \cdot 10^6 \text{ kg/s}$.

The simulation time is one hour, the eruption lasts 30 min. Within the first 10 seconds, the eruption velocity is increased to its maximum, followed by a phase of 27 min of continuous eruption. During the last 3 min of the eruption, the vent exit velocity is reduced to zero again. We continue the simulation for

additional 30 min in order to investigate the post-eruptive development of the volcanic plume.

For initialising the environmental profiles of temperature and humidity, we use radiosonde data from the tropical pacific with the tropopause at 17 km, shown in Fig. (8). The impact of the plume geometry and the environmental conditions on

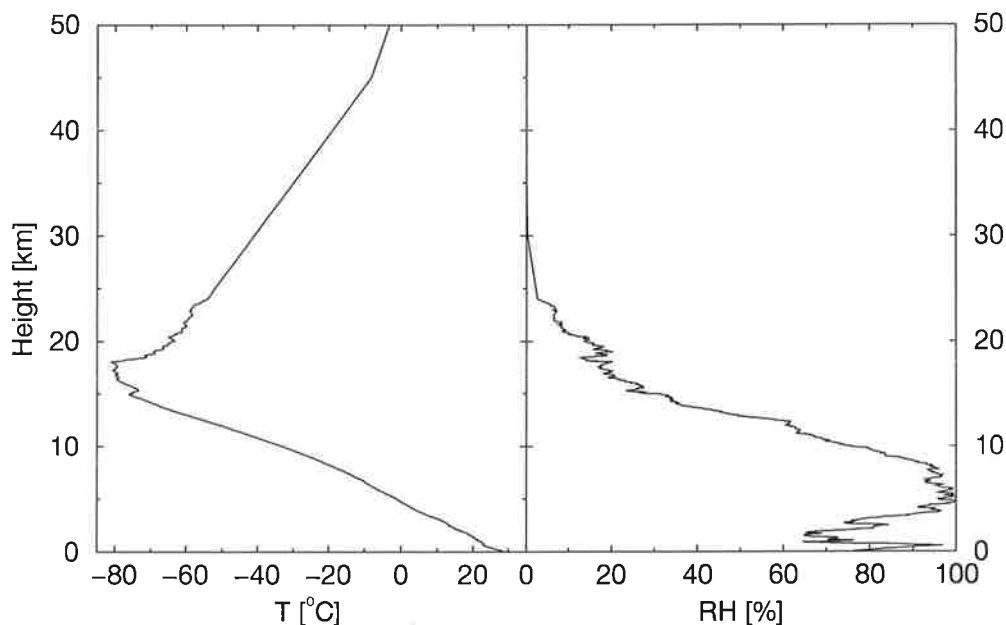


Figure 8: Atmospheric profiles for temperature and relative humidity. Radiosonde data from TOGA COARE, R/V Vickers, Feb. 10th 1993, 12 h UTC, 2.04 °S, 156.1 °E.

the plume's shape and height has been investigated by (*Herzog, 1998; Graf et al., 1999*) and is not the subject of this study. Their simulations revealed, that the plume height is not only determined by the composition and temperature of the erupting material and its vent exit velocity. But it is also strongly dependent on the actual meteorological conditions in the environment in terms of atmospheric stability and relative humidity. The latent heat release due to phase changes of water contributes a considerable amount to the plume's total thermal energy and has therefore a significant effect on the vertical development of the eruption column. The plume that develops under the conditions employed for the simulations in this study reaches the stratosphere. The dynamic and environmental conditions of the volcanic eruption are constant for all experiments.

6.2 Reference Experiment

In the next sections, we present the results of the reference experiment REF.⁵ Plume shape and height as well as qualities of the hydrometeors and ash aggregates will be described. After that, the sensitivity studies concerning the microphysics of hydrometeors and ash particles in the eruption column will be discussed.

The simulated size distribution of volcanic particles erupted at the crater has been fitted to the size distribution observed by *Carey and Sigurdsson* (1982), illustrated in Sect. (2.3). The mean volume radius of the two particle classes in the reference experiment is $r_{ac} = 2.5 \mu\text{m}$ and $r_{ap} = 50 \mu\text{m}$, respectively, with the smaller class contributing 40% to the total ash mass. The width parameters of the gamma distributions are both $\nu = 1$, hence, the distributions are rather broad with a small modal radius as shown in Fig. (9).

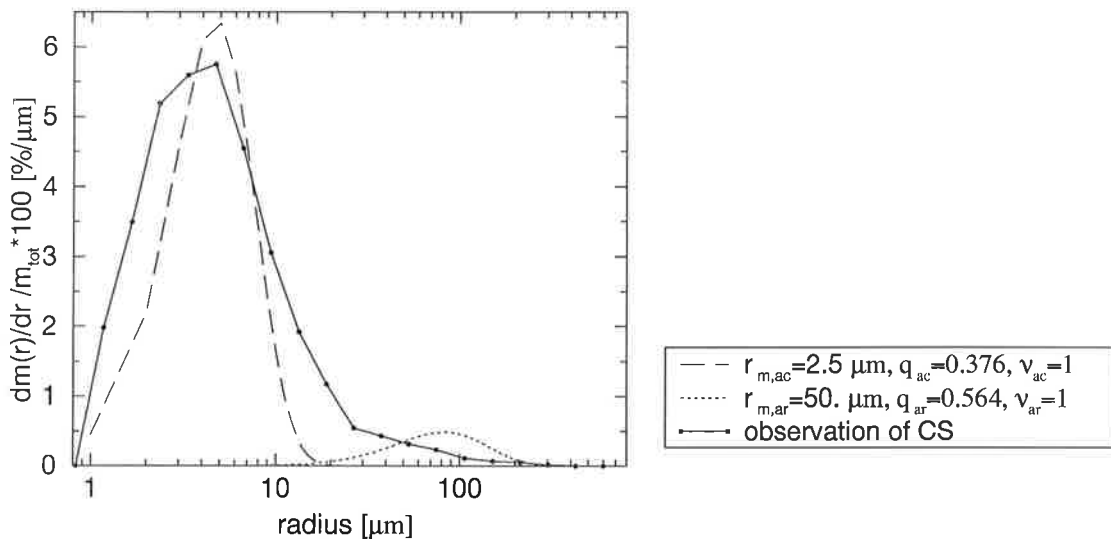


Figure 9: Initial mass distribution of volcanic particles in the reference experiment REF: the observations of *Carey and Sigurdsson* (1982) and the fitted distributions are shown. Legend: r_m is the mean volume radius, q the specific mass and ν the width parameter of the size distribution. The indices *ac* and *cr* refer to the small and the large ash mode, respectively.

⁵ REF: reference experiment

6.2.1 Plume Characteristics

Under the conditions applied in the reference experiment, the central plume zone penetrates the tropopause within ~ 5 min after the eruption has started, due to the strong vertical velocity of about 100 m/s. (For the streamline pattern see Fig. (15).) Fig. (10) and Fig. (11) show the plumes of volcanic particles and of an inert volcanic gas after 30 min of eruption. An inert gas is not scavenged by particles or hydrometeors, but it is passively transported with the mean flow. The shape of the ash plume is determined by the fallout of particles, most of the mass stays in the troposphere. A comparatively narrow gas band with a higher horizontal extension expands at the tropopause level. The separation of gas and particles is clearly visible. The stationary height at the tropopause level, where the density inside the plume is the same as in the ambient atmosphere, is reached approximately 10 min after the eruption onset. It can be identified by the horizontal spreading of both plumes; though in the case of ash, the pattern is modified by sedimentation of particles. The peak heights of both plumes are well in the stratosphere, the eruption exhibits overshooting by more than 3 km above the equilibrium height. The maximum gas plume height of 22 km is slightly higher than that of the ash plume at 20 km.

The post-eruptive plumes of the volcanic particles and the inert gas 30 min after the eruption ended are shown in Fig. (12) and Fig. (13). The patchy structure of the ash plume is due to the eddy structure of the currents in the atmosphere, see Fig. (15), that are conserved also after the end of the eruption, because cross wind effects had to be neglected in the cylindrical model version used for these simulations. The ash plume has collapsed, most of the ash is constrained below the tropopause within a horizontal area of about 20 km around the volcano. During our simulation, most of the deposits fall in proximal areas, a very small amount of fine ash is still situated in the stratosphere and will be transported to great distances before it will precipitate. These results are in qualitative agreement with the observed deposition fans of volcanic ash (e.g. at Mt. St. Helens reported by *Carey and Sigurdsson, 1982*).

The post-eruptive volcanic gas cloud is distributed in the stratosphere with a large horizontal extension of more than 60 km. The central gas peak in the stratosphere above the crater is induced by the collapsing ash plume: for reasons of continuity a corresponding updraft develops, further enhancing the gas-particle separation. Gas-particle separation was observed by remote sensing in the volcanic eruption cloud of El Chichón during the first days after the eruption. *Schneider et al. (1999)* indicated that gaseous SO_2 and fine grained ash at different heights were further separated by strong vertical wind shears prevailing in the atmosphere: the upper stratospheric SO_2 cloud was transported to the west, while the ash traveled to the south in the troposphere. This additional horizontal separation

permitted the isolated observation of the two different clouds by satellites (SO_2 by TOMS and volcanic ash by AVHRR).

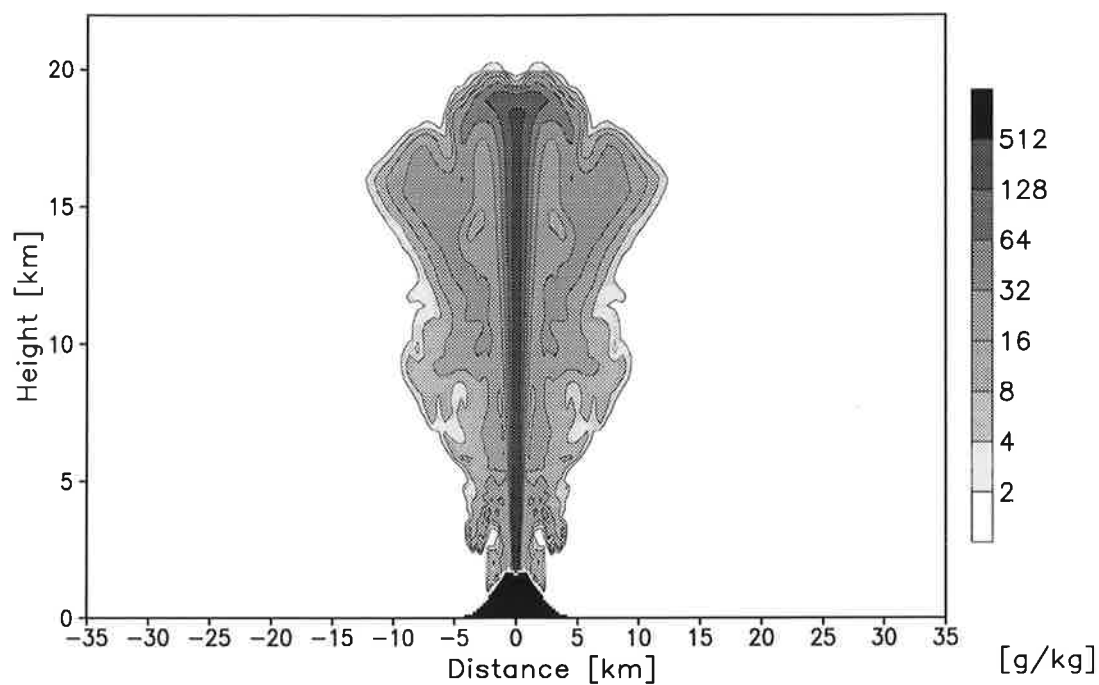


Figure 10: Plume of volcanic particles: specific mass content after 30 min of eruption in the reference experiment REF.

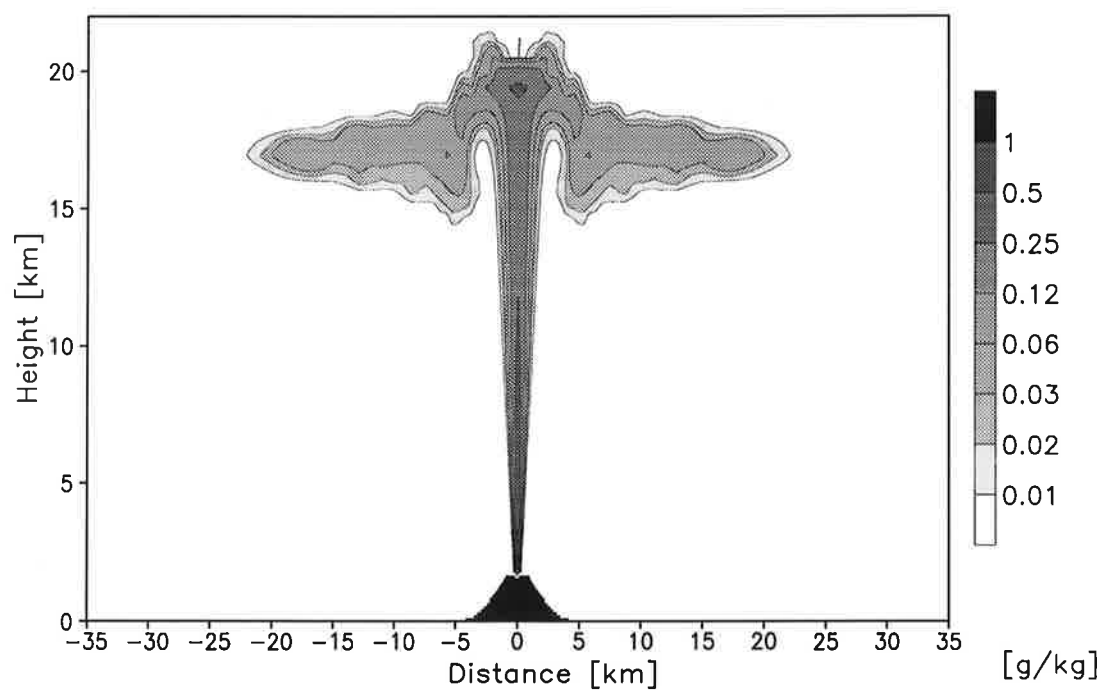


Figure 11: Plume of an inert volcanic gas: specific mass content after 30 min of eruption in the reference experiment REF.

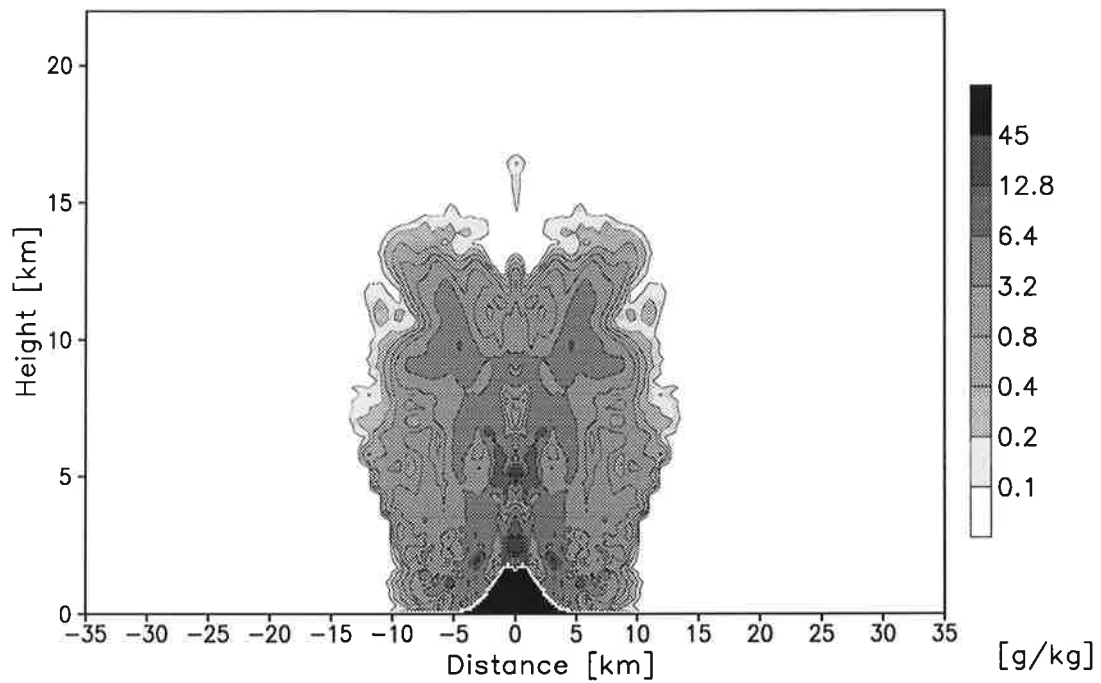


Figure 12: Plume of volcanic particles: specific mass content 30 min after the end of the eruption in the reference experiment REF.

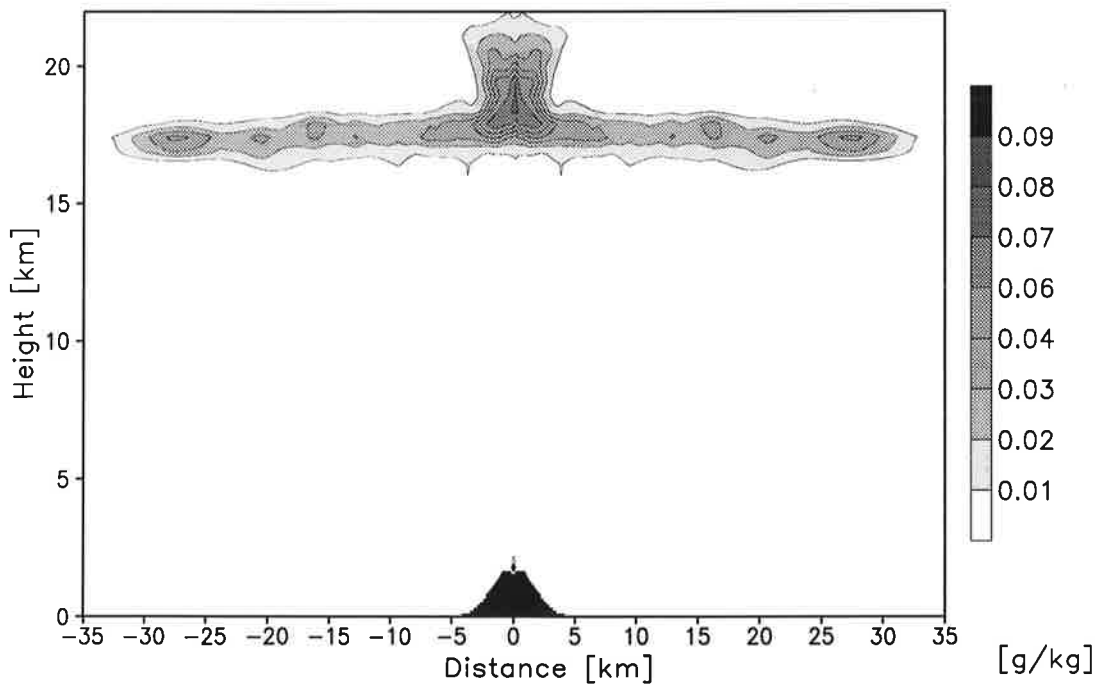


Figure 13: Plume of an inert volcanic gas: specific mass content 30 min after the end eruption in the reference experiment REF.

Fig. (14) illustrates the vertical distributions of the two particle classes considered in ATHAM, again after 30 min of eruption and for the post-eruptive situation another 30 min later. By far the highest portion of particles is contained in the

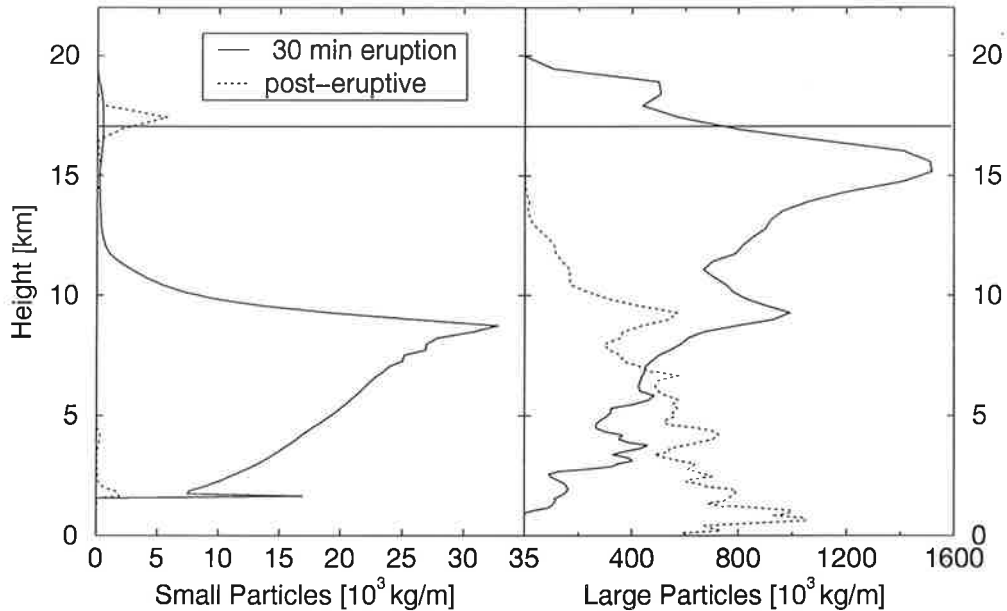


Figure 14: Vertical distributions of volcanic particles in [10^3 kg per m height] in the small category (left panel) and volcanic particles in the large category (right panel) at 30 min of eruption and 30 min after the end of the eruption in the reference experiment REF. The tropopause at 17 km is indicated by the thin horizontal line.

large mode resulting from particle coagulation, which leads to larger sizes (notice the different mass scales). The small ash mode is strongly reduced above 8 km height, where the condensation of hydrometeors results in efficient coagulation which transfers small ash to the large mode. The corresponding peak in the vertical distribution of large particles (Fig. (14), right panel) can be seen at about 10 km height. The vertical distribution of the large mode is determined by sedimentation processes: it prevents larger aggregates from staying at great altitudes. During the eruption, most of the ash in the large mode occurs below the tropopause; at the end of our simulation time, a high portion of aggregates has already reached the ground. Fine particles and volcanic gases stay at the tropopause level and distribute laterally. The post-eruptive plume of the smaller particles in Fig. (14), left panel, reveals a peak above the tropopause. The updraft occurring in the upper part of the plume lifts volcanic material while the lower part collapses: fine particles – and gases, as mentioned before – staying in the tropopause region are separated from the lower column.

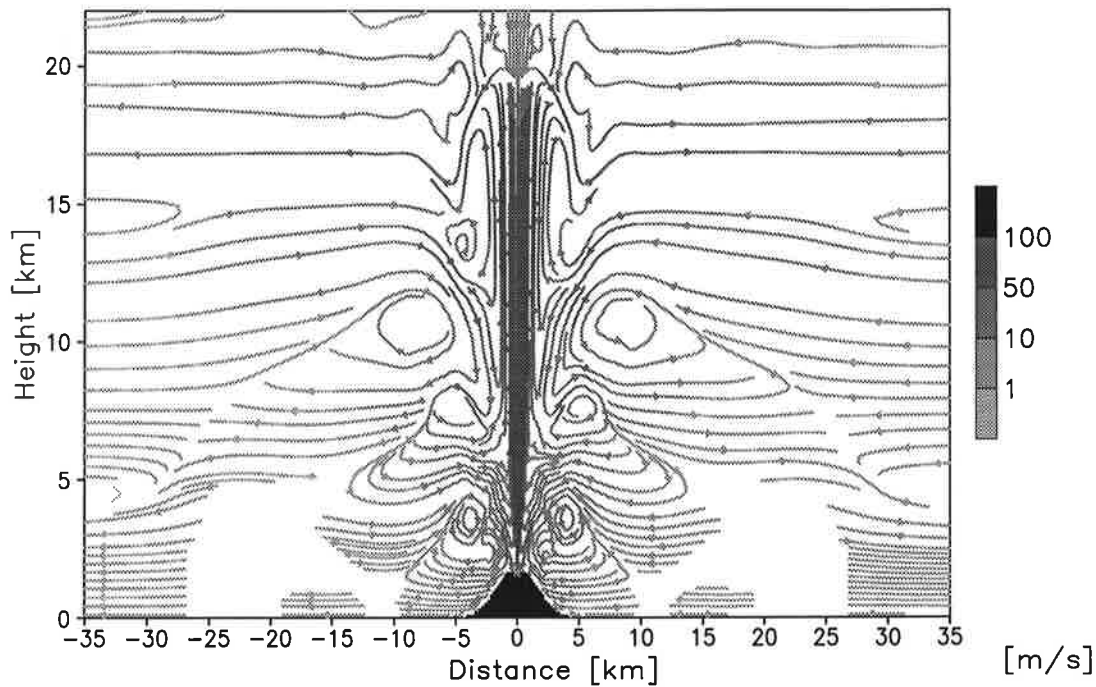


Figure 15: Streamlines of wind [m/s] after 30 min of eruption in the reference experiment REF. Velocities smaller than 0.1 m/s are not shown.

The atmospheric currents during the eruption are illustrated in Fig. (15). High vertical velocities between 50 and 100 m/s occur in the central rising zone, up to 20 km height. This induces horizontal movement of ambient air towards the eruption column. Sedimentation of volcanic particles results in an extensive subsidence of the gas-particle-mixture at about 15 km, inducing the turbulent structure of the current: at the sides of the plume, eddies can be seen which cause efficient entrainment of ambient air. Particles that precipitate from the umbrella region might be reentrained into the ascent zone and rise again.

When interpreting the results presented here, one must keep in mind that the simulation has been performed in cylindrical coordinates. Hence, effects of a mean lateral wind have been neglected, the resulting flow pattern in the atmosphere is only influenced by currents induced by the volcanic eruption. The circulation is not disturbed by background winds and might be quite artificial. However, the results from our experiments are suitable to investigate the principal features of an explosive volcanic event.

Fig. (16) illustrates the time dependent development of the fractions⁶ of tephra

⁶ In the context of this study, the terms ‘fraction’ or ‘portion’ are always in relation to the mass of the quantity under consideration.

and the inert volcanic gas, which are injected into the stratosphere or deposited to the ground, in relation to the total mass erupted at the vent. The gas plume

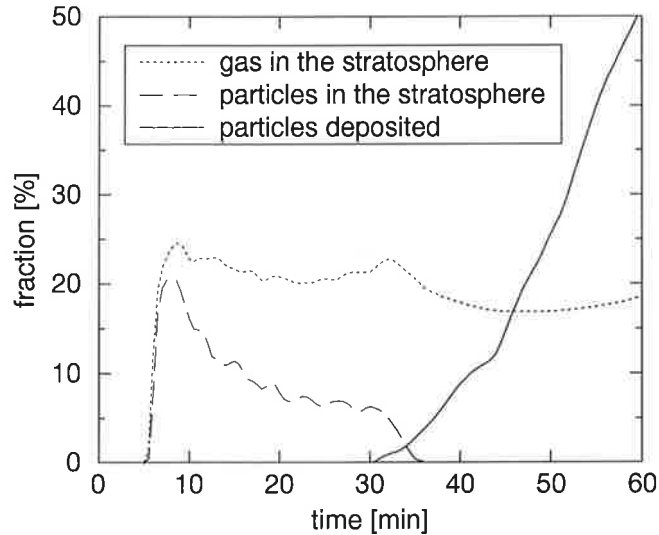


Figure 16: Temporal development of the fraction of volcanic gas and particles injected into the stratosphere or deposited to the ground in [%] of total mass erupted at the vent in the reference experiment REF.

spreads horizontally mainly at the tropopause level. After an initial peak with a maximum value of 25 % at about 10 min of the eruption, a relatively constant fraction of about 20 % is distributed in the stratosphere during the whole simulation. On the other hand, most of the volcanic ash remains in the troposphere. An initial maximum ratio of ~ 20 % of the total tephra erupted at the vent is situated above the tropopause 10 min after the eruption started. Volcanic ash reaching the stratosphere caused by the strong buoyancy in the plume is quickly removed from high altitudes. Particle growth leads to sedimentation, removing ash from the stratosphere: at the end of the one hour simulation, the tephra fraction in the stratosphere is about $4 \cdot 10^{-5}$ of the total erupted mass, leading to an injection rate of about 1000 tons per hour continuous eruption. Considering the enormous amounts of ash erupted during a volcanic explosion, this is a large quantity. At the end of the eruption, particles begin to reach the ground because the plume begins to collapse completely. In addition, this is about the time, which particles need to fall from the plume top to the ground, see Sect. (6.2.4). At the end of our simulation period, another 30 min later, about 50 % of the total emitted ash is already deposited at the ground level.

6.2.2 Hydrometeors

Fig. (17) displays the relative humidity with respect to ice after the calculation of microphysical processes in the model. The fast vertical transport of water vapour in the plume leads to relative humidities greater than 150% in the central ascent zone. This huge supersaturation can neither be completely removed by condensation or deposition of water vapour on preexisting particles nor by nucleation of cloud drops or ice crystals.

Most of the background atmosphere below the umbrella cloud is undersaturated with respect to water or ice, see Fig. (8). Thus, precipitation will evaporate in these regions in the troposphere before reaching the ground. At the lateral edge of the rising plume below the umbrella cloud, the atmosphere is highly undersaturated. This is a result of the subsidence of dry air from higher levels - illustrated in Fig. (15) - which leads to entrainment of relative dry air. In Fig. (18), the specific mass content of water vapour shows minima in the same region: near the central rising zone, the water vapour content is lower than the ambient value at the same height. On the other hand, the core of the plume is characterised by a higher water vapour content resulting from the volcanic source and from the lifting of humid air, which had been entrained in the lower part of the eruption column. The total amount of water (vapour and hydrometeors) in the plume is about 2.4 times that erupted by the volcano, after 30 min of eruption. Between 15 and 20 km in the umbrella cloud, the water vapour pressure fluctuates around its saturation value over ice. Ice particle growth by deposition occurs in supersaturated regions. Above 20 km, the relative humidity becomes lower than 100 % resulting in reevaporation of ice particles. The volcanic injection of water vapour into the stratosphere is clearly visible in Fig. (18). The total injection of water in our simulations is 30 000 tons per hour, where cloud ice contributes about 80 % of the total input. Enhanced water vapour concentration in the stratosphere was observed by *Murcray et al.* (1981) who found evidence that a large amount of water vapour was injected into the stratosphere by the 1980 eruption of Mt. St. Helens: the water vapour mixing ratio in the stratospheric plume four days after the main eruption was a factor of two to ten times above the background value. *Burnett and Burnett* (1984) reported by 30 % enhanced column abundances of OH radicals in the summer following the El Chichón eruption in 1982 above the central United States. The authors suggested that this increase was due to the injection of water vapour into the stratosphere. The specific mass content of hydrometeors and the related vertical profiles of each hydrometeor class are shown in Fig. (19) and Fig. (20), 30 min after the onset of the eruption. The hydrometeor plume also penetrates the tropopause, injection of frozen hydrometeors in the stratosphere is exhibited. The highest mass content occurs in the central ascent region due to the high supersaturation of water vapour. Water vapour starts to condense on ash particles above the

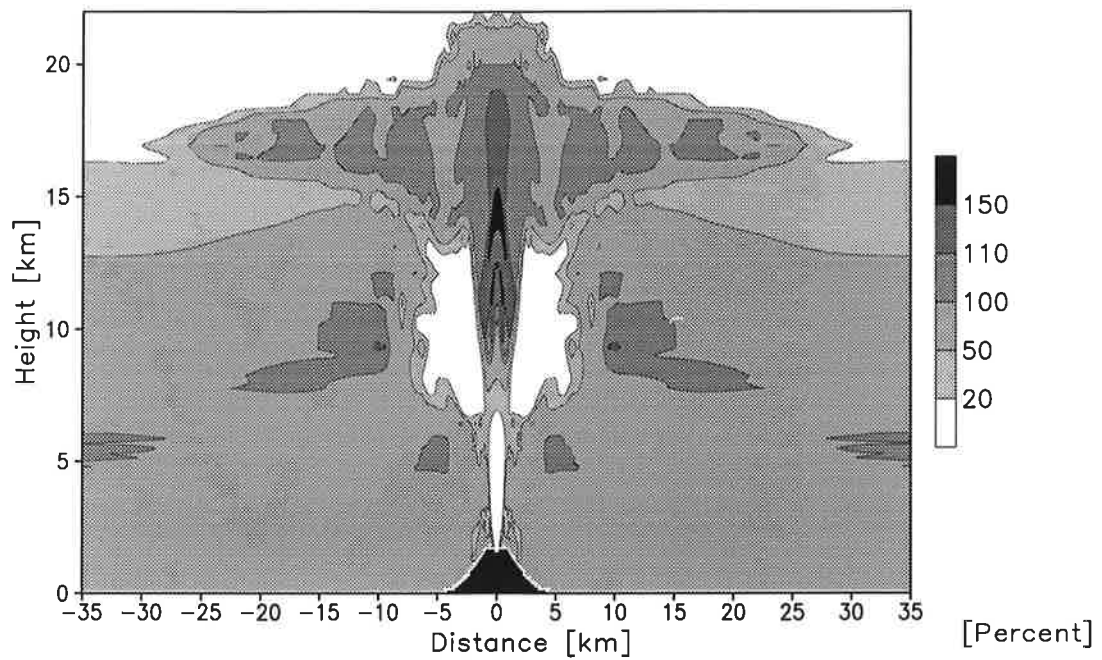


Figure 17: Relative humidity with respect to ice after 30 min of eruption in the reference experiment REF.

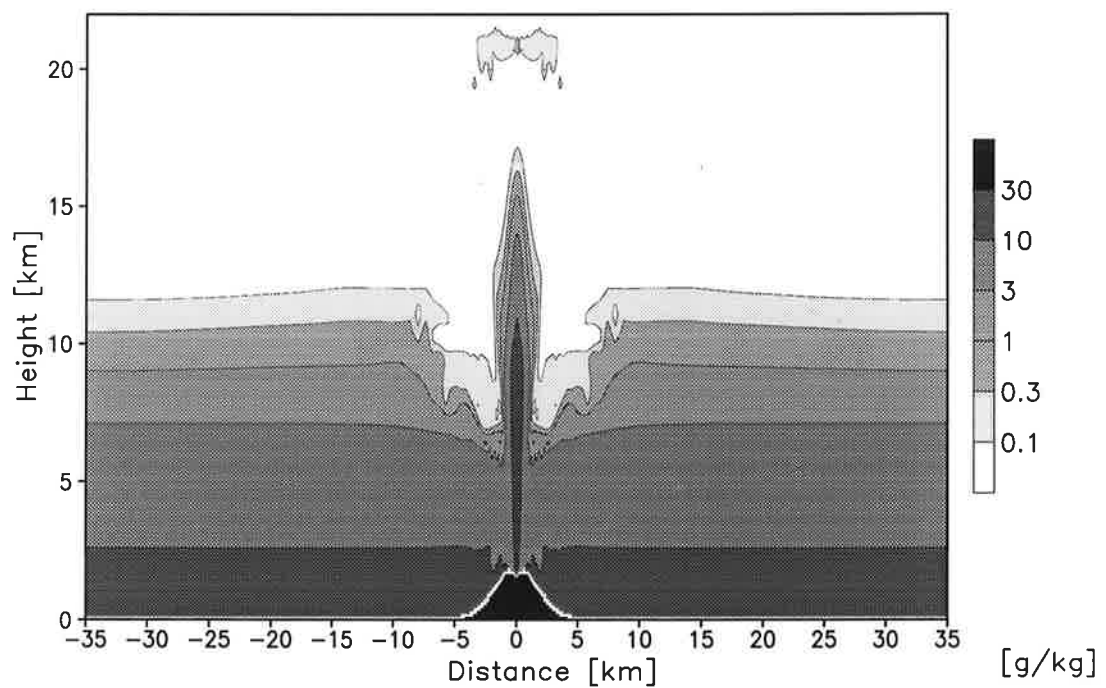


Figure 18: Specific content of water vapour after 30 min of eruption in the reference experiment REF.

crater at about 8 km forming liquid water droplets. The high ascent rate of the plume rapidly lifts these droplets to heights too cold for even supercooled water to exist. The simulations performed with the plume model ATHAM revealed that a large fraction ($\sim 98\%$) of the hydrometeors in the plume froze to ice particles. The existence of ice in volcanic plumes was confirmed by observations of the eruption columns of Redoubt in 1989-90 (*Schneider and Rose, 1993*), Rabaul in 1994 (*Rose et al., 1995*) and Soufriere Hills Volcano, Montserrat in 1998-99 (*Rose, 1999*). Small ice particles - possibly containing ash - quickly grow to larger graupel-like aggregates in our simulation. The highest fraction of condensed water is contained in the graupel-category. At the tropopause level, an ice cloud with a great horizontal extent of up to 40 km occurs. It is composed of particles with radii of about $5\ \mu\text{m}$ that tend to spread horizontally rather than to precipitate like the larger graupel-like aggregates.

After the end of the eruption, the plume of graupel-like particles is completely situated in the troposphere, see Fig. (20) right panel. The melting of precipitating graupel produces liquid water below 5 km, however, as previously mentioned, it reevaporates at about 3 km, before it reaches the ground. Hence, only a negligible amount of the aggregate-fallout reaching the ground consists of condensed hydrometeors. The ice cloud has lifted above the tropopause due to the updraft mentioned before in Sect. (6.2.1). The stratospheric ice content has increased due to accumulation and deposition of water vapour.

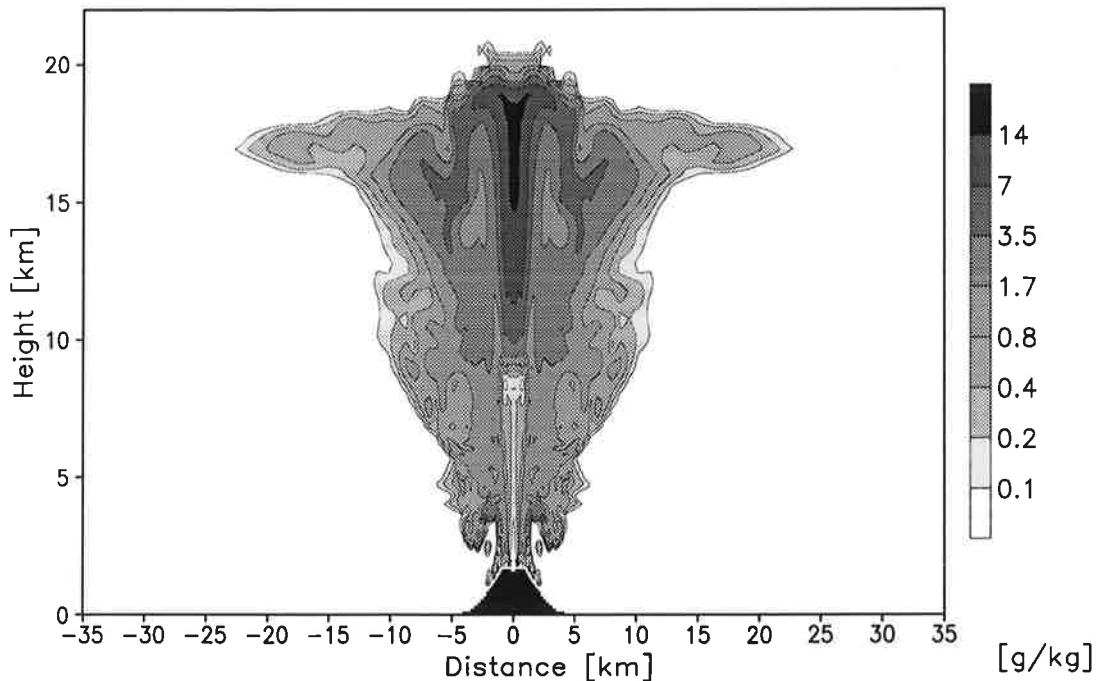


Figure 19: Specific mass content of hydrometeors [$\text{g}/\text{kg}_{\text{totalmass}}$] after 30 min of eruption in the reference experiment REF.

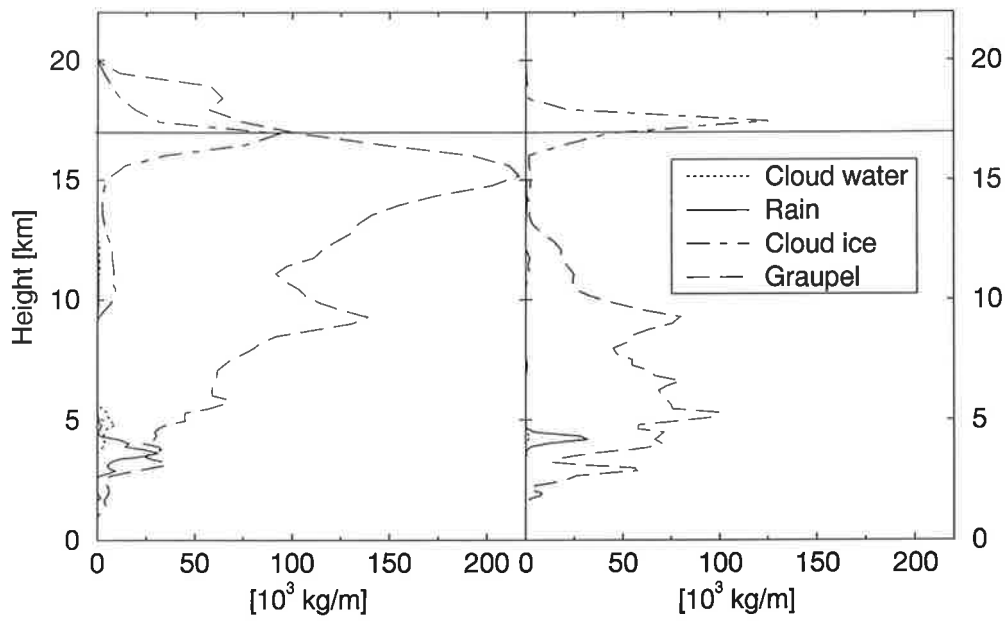


Figure 20: Vertical distributions of hydrometeors in [10^3 kg per m height] at 30 min of the eruption (left panel) and 30 min after the eruption ended (right panel) in the reference experiment REF. The tropopause at 17 km is indicated by the thin horizontal line.

6.2.3 Number Concentration

Fig. (21) displays the number concentration of all the particles in the plume after 30 min of eruption. This number refers to the sum of all classes of pure hydrometeors, ash and aggregates. The number of particles is determined by the volcanic

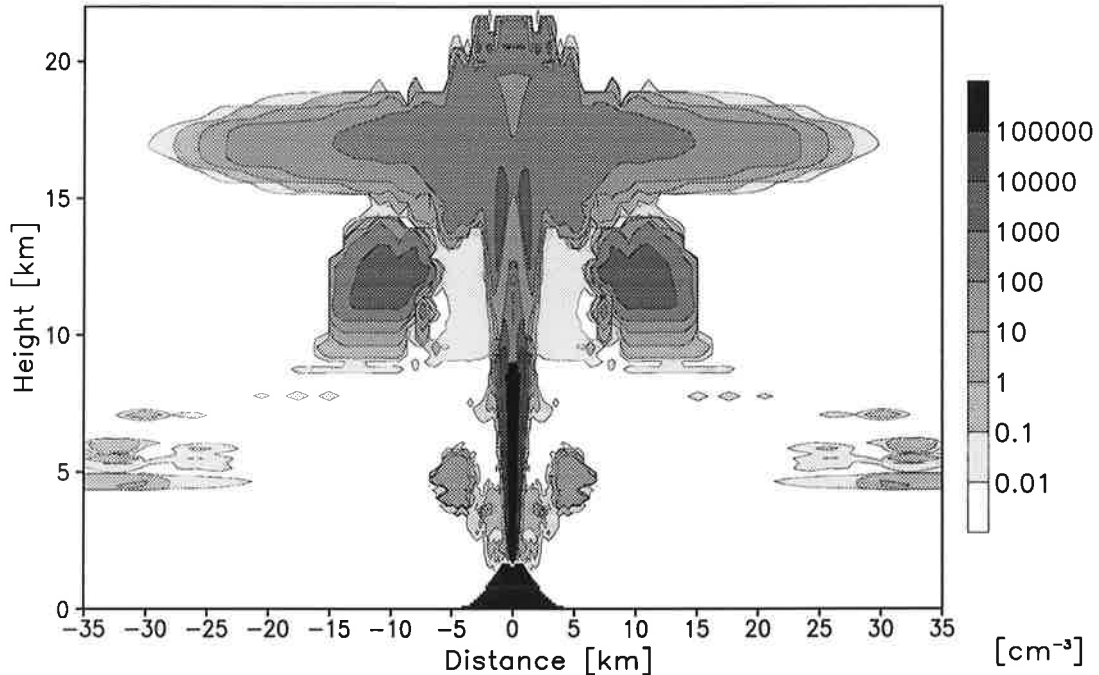


Figure 21: Number concentration of all particles in the plume in $[\text{cm}^{-3}]$ after 30 min of eruption in the reference experiment REF.

forcing in the lower part of the plume. The number concentration of ash particles injected into the atmosphere by the volcano is about $2.5 \cdot 10^6 \text{ cm}^{-3}$ in the small class and 460 cm^{-3} in the large class, respectively. It is decreasing with height due to plume dilution and particle coagulation. The number concentration of the smaller particles in the cloud-aggregate category is in the order of 100 to 1000 particles per cm^3 in the umbrella region of the cloud. The highest concentration occurs in the central rising zone, where diffusional growth results in quick transfer of small particles to the larger graupel-class. In addition, the large supersaturation, see Fig. (17), leads to the nucleation of new particles. This process is represented by rather simple approaches in our parameterisation, see Sect. (3.6), however, the results obtained in this study look quite reasonable. Observations in storm clouds have shown that the number concentration of frozen hydrometeors decreases with increasing particle size. The concentration of graupel has been reported to range from 10^{-3} to 1 cm^{-3} for radii between 250 and $2500 \mu\text{m}$ (Pruppacher and Klett, 1997). Our simulations revealed number concentrations between 10^{-2} and 1 cm^{-3} in the upper plume. This result and the particle radii

shown in Fig. (23) derived from the mass content and the number concentration are well within the concentration range, which was observed in natural storm clouds. Observational data about the particle concentrations inside the plume are not available at the moment, however, their knowledge and that about aggregate qualities are essential for the retrieval of information from remote sensing data.

6.2.4 Aggregate Qualities

The hydrometeor-ash aggregates in the plume are mostly composed of volcanic ash: the ash fraction in the mixed particles displayed in Fig. (22) is typically greater than 80 % of the particle mass due to the surplus of volcanic ash compared to condensed hydrometeors. The total mass of tephra in the model domain

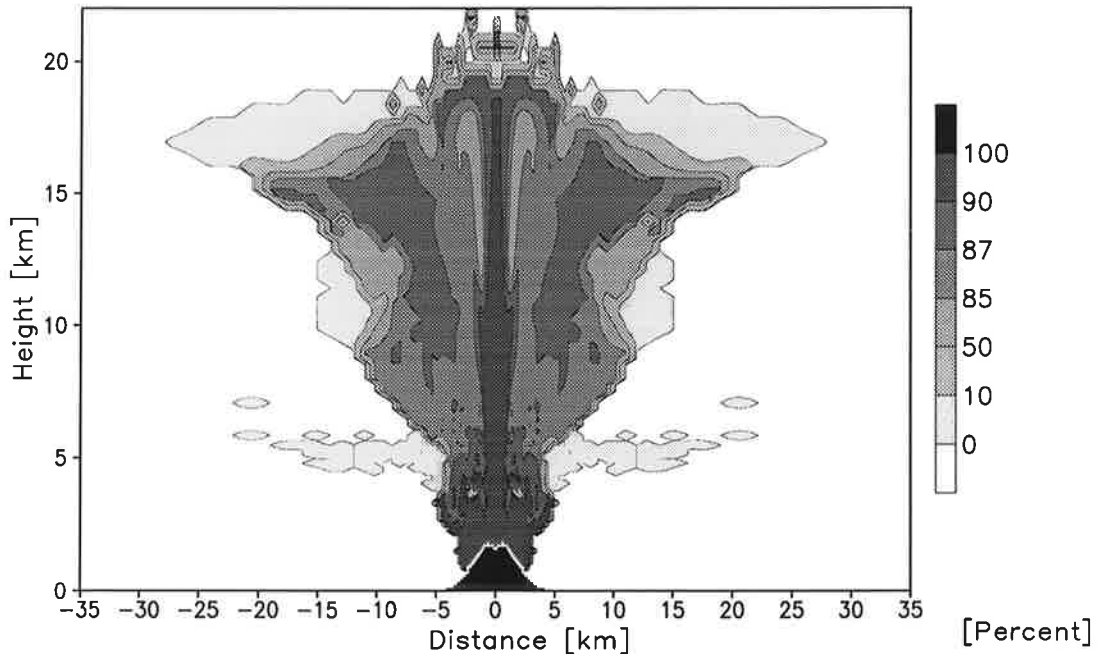


Figure 22: Volcanic particle fraction in mixed aggregates in relation to the total aggregate mass content in [%] after 30 min of eruption in the reference experiment REF.

after 30 min of eruption is about 100 times that of hydrometeors. Hence, our simulations revealed the development of quite dry ash aggregates or accretionary lapilli, rather than mud rain. Only the ice cloud in the umbrella region at the tropopause level consists of quite pure ice crystals, since it evolves mainly from nucleation of new ice particles rather than from deposition of water vapour on preexisting tephra. This is because the ash content is rather low at larger horizontal distances from the crater due to particle sedimentation of aggregates near

to the vent. The aggregates which finally reach the ground are even drier due to hydrometeor evaporation at lower heights, as previously mentioned.

Fig. (23) displays the radii of the aggregates in the large mode of frozen particles which is the most important category after 30 min eruption. In our model

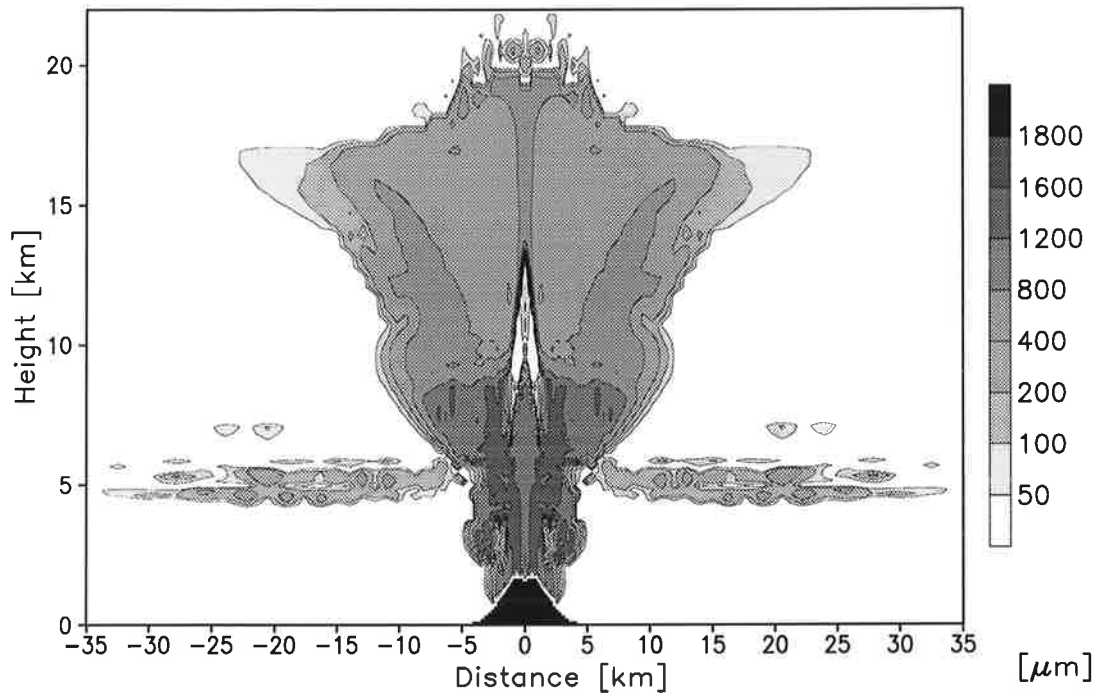


Figure 23: Radius of large cold aggregates
30 min of the eruption in the reference experiment REF.

formulation, it is not possible for hydrometeors and ash particles to coexist in the same place: hence, the displayed radius refers to particles consisting of either pure graupel, pure volcanic ash or mixed graupel-ash aggregates. Particle growth is highest in the central rising zone directly above the crater due to the high particle concentration and the strong supersaturation of water vapour, see Fig. (17), the biggest particles are found in this region. The radii of aggregates are between 2.5 and 30 μm in the small class and between 200 and 1500 μm in the large class. This agrees quite well with the observed sizes of deposited volcanic aggregates with radii in the millimeter range as reported in *Sparks et al.* (1997).

Our parameterisation of tephra particle growth does not include breakup processes. However, the fraction of water in the mixed particles is in most places lower than 20%. The evaporation of water in the lower part of the plume leads to additional drying, this way possibly disconnecting some aggregates. Larger aggregates may be destroyed due to hydrodynamic instabilities during precipitation or collision with other particles, similar to the breakup of large rain drops. In

addition, the uncertainties concerning the collection coefficient $E_{xy,agg}$ – discussed in Sect. (3.9) – could result in an overestimation of particle growth. Hence, the results obtained in this study may represent an upper limit on aggregate sizes.

The terminal fall velocities of the particles in the large ash category shown in Fig. (24) are about 10 m/s in the troposphere and about 12 m/s at 20 km height due to the decrease of friction at greater altitudes. With an average fall velocity of 10 m/s the aggregates need about half an hour to fall from the top of the plume to the ground. The particles have been assumed to be solid spheres. The effect of particle shape on the fall velocity is only considered by applying a drag coefficient as explained in Sect. (3.5). These simplifications might lead to an overestimation of the fall speed, however, they seem to be justified compared to the general lack of information about the particle's shape and size distribution in the plume.

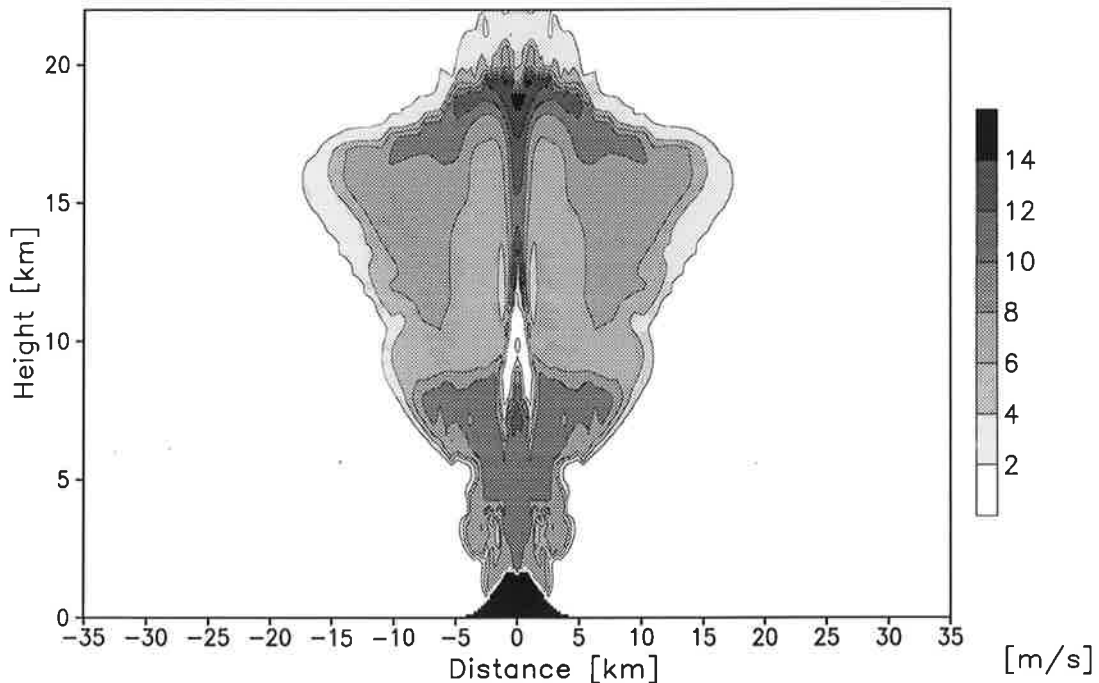


Figure 24: Fall velocity of large cold aggregates
30 min of the eruption in the reference experiment REF.

6.3 Microphysical Sensitivity Studies

In this section the effect of the interaction between volcanic particles and hydrometeors is analysed in the experiment DRY⁷. In addition, we investigate the influence of different volcanic particle sizes in the erupting mixture (experiments NAR⁸ and ASH⁹). Tab. (2) gives the initial parameters used in the reference study (REF) outlined in the previous Sect. (6.2) and the sensitivity experiments that are described in the following section.

	REF	DRY	ASH	NAR
q_{ac} [wt. %]	40	40	100	40
q_{ar} [wt. %]	60	60	0	60
r_{ac} [μm]	2.5	2.5	2.5	2.5
r_{ar} [μm]	50	50	–	50
ν_{ac}	1	1	1	10
ν_{ar}	1	1	–	10
ash - hydrometeor interactions	+	–	+	+

Table 2: Sensitivity Studies: microphysics and volcanic particles.

r is the mean volume radius, q the specific mass and ν the width parameter of the size distribution. The indices ac and ar refer to the small and the large ash mode, respectively.

6.3.1 Particle-Hydrometeor Interactions

The experiment DRY was performed with the same conditions as the reference experiment REF. However, the interaction of volcanic particles and hydrometeors was neglected. Hence, volcanic ash is always dry, ash growth by water vapour deposition or coagulation of tephra particles and accretion of ash by hydrometeors is not considered. Volcanic ash is transported in the model, but does not take part

⁷ DRY: dry ash, no hydrometeor-ash interactions

⁸ NAR: narrow ash size distributions

⁹ ASH: small ash mode only

in any microphysical process, the parameterisations presented in Chap. (3) are applied for pure hydrometeors. This sensitivity study investigates the importance of considering ash particle growth in a volcanic plume. On the other hand, the experiment corresponds to an eruption taking place in an arid climatic zone with a smaller amount of condensed water available in the plume.

The shape of the resulting plume after half an hour of the eruption looks completely different from the ash plume in the reference experiment REF in Fig. (10). Instead, it is similar to the gas plume in Fig. (11) with an umbrella cloud of large horizontal extension. Fig. (25) illustrates the vertical profiles of tephra particles after 30 min of eruption and 30 min later, after the end of the eruption. See also Fig. (14) for comparison with the experiment REF. In the experiment DRY, the entire mass of volcanic ash is present in the atmosphere after one hour simulation, the deposition of particles does not occur. The fall velocity of the dry tephra particles is rather small compared to the wet, coagulated, larger aggregates in the reference experiment REF. For the $50\ \mu\text{m}$ ash particles in the large mode it is of the order of $1\ \text{m/s}$, the small ash particles with $2.5\ \mu\text{m}$ radius are quasi-suspended in the air.

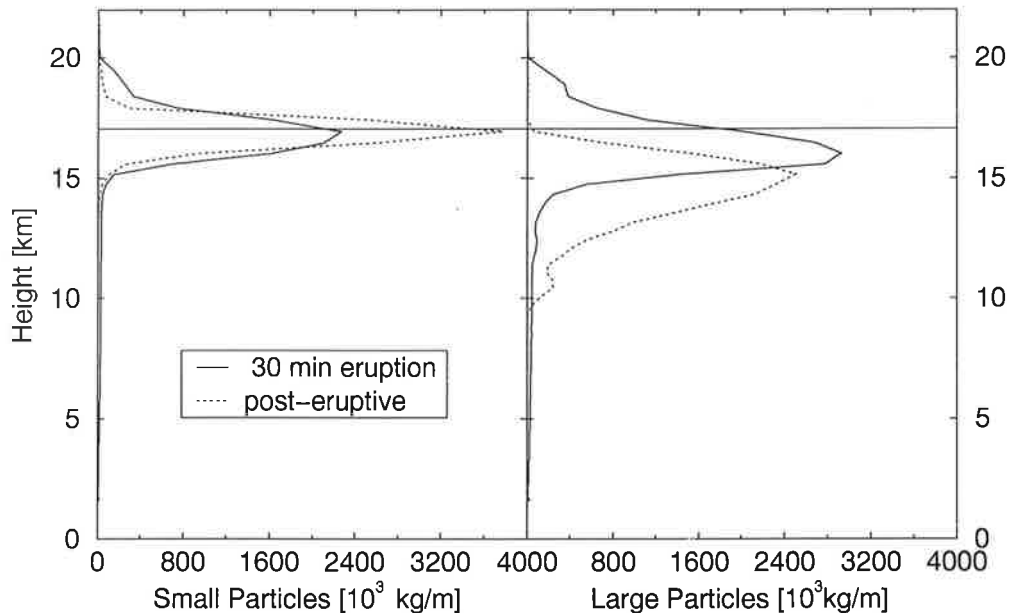


Figure 25: Vertical distributions of volcanic particles in [10^3kg per m height] in the small category (left panel) and volcanic particles in the large category (right panel) at 30 min of the eruption and 30 min after the end in the experiment DRY without particle-hydrometeor interactions. The tropopause at 17 km is indicated by the thin horizontal line.

During the eruption, the maximum ash plume height in the experiment DRY is ~ 22 km, only slightly higher than in the reference experiment. After the eruption ended, the particle plume in REF has already collapsed, while the ash in the experiment DRY stays almost at its eruption altitude, the lower edge of the fallout just reaches 10 km height. The mean heights of the ash plumes shown in Fig. (26) – each level has been weighted by its relative mass content – are quite different during the eruption. The fallout of large aggregates in REF shifts the main ash portion to lower altitudes compared to the ash in DRY that does not noticeably sink. Gas-particle separation which occurs in the experiment REF causes the remaining mixture to have a slightly lower density than in DRY. This results in a slightly higher mean height of the gas plume in REF. However, the umbrella regions of the gases are located at the tropopause level and only have small vertical extensions, so the small difference in plume height leads to considerably different gas injections into the stratosphere as illustrated below. Neglecting the hydrometeor-particle interactions causes the overestimation of ash

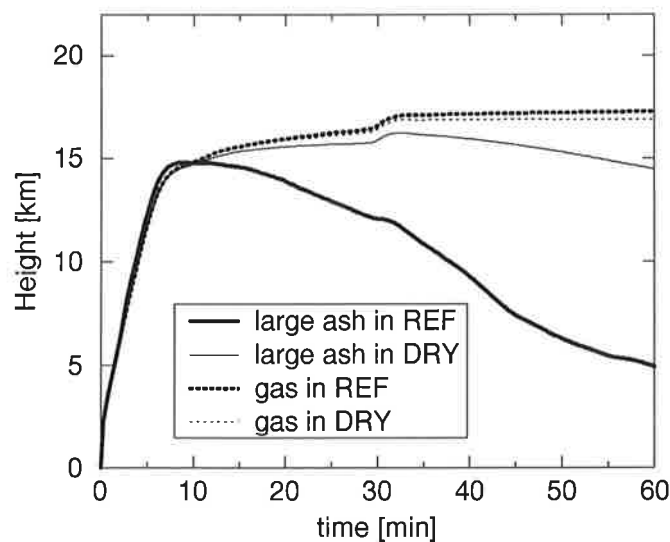


Figure 26: Temporal development of the mean plume height of an inert volcanic gas and the large ash class, in the reference experiment REF and in the experiment DRY without particle-hydrometeor interactions.

particle injection and the underestimation of gas injection into the stratosphere. For comparison of the time dependent fractions in REF and DRY see Fig. (16) and Fig. (27), respectively. After about 5 min, the plumes in REF as well as in DRY reach the tropopause. The stratospheric injection in DRY is almost 25 % of the total erupted ash mass, which is by 5 % higher than in REF. If growth of volcanic particles is not considered, about 2 % of the erupted mass remain in the stratosphere after the end of our simulation, resulting in an input of 500 000 tons

per hour for a continuous eruption. This is about 500 times more than in the experiment which included aggregation, see Sect. (6.2).

The portion of total emitted ash in the stratosphere has not yet been determined exactly for real explosive volcanic events. During the eruption, the opaque plume prevents from obtaining detailed data. Observations by remote sensing (e.g. AVHRR) are restricted to a certain grain size and possibly do not cover the total ash mass (*Schneider et al.*, 1999, among others). In addition, it is difficult to distinguish volcanic ash from sulphate aerosol of the same size that forms from the oxidation of SO_2 and H_2S . *Schneider et al.* (1999) and *Yu and Rose* (1999) estimated that less than 1% of the total mass in the small mode reached the stratosphere during the eruption of El Chichón.

Gas-particle separation leads to greatly enhanced gas injection: In the experiment REF about 20% of the inert gas erupted at the vent is present in the stratosphere. Only a quarter of this amount reaches the stratosphere during the DRY simulation, without particle growth. This difference is also relevant when considering the fate of volcanic gases in the plume, that influence the stratospheric chemistry and the global climate. The injection of volcanic sulphur gases and HCl into the stratosphere will be examined in Sect. (6.4).

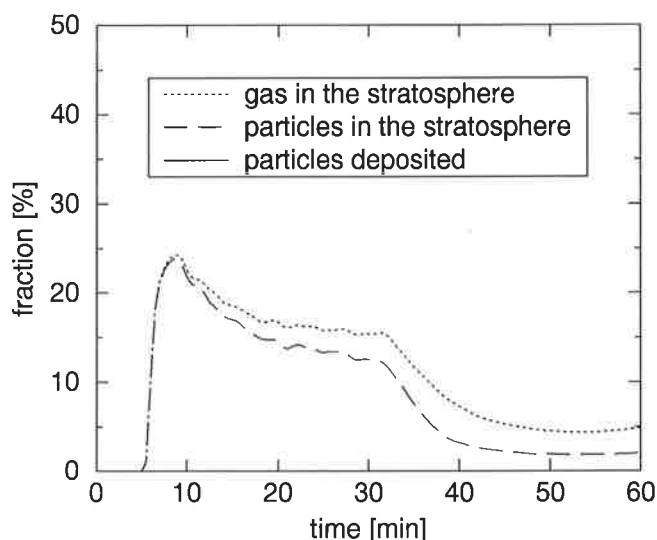


Figure 27: Temporal development of the fractions of an inert volcanic gas and particles injected into the stratosphere or deposited to the ground in [%] of total mass erupted at the vent, in the experiment without particle-hydrometeor interactions, DRY.

The lack of particle sedimentation in the DRY simulation at the sides of the plume reduces primarily the removal of particles from the atmosphere, but also induces a completely different stream pattern, as can be seen in Fig. (28). The vertical

eddy structure along the entire vertical axis of the eruption column noticed in the reference experiment REF, see Fig. (15), is not visible. On the contrary, up to an altitude of about 10 km the flow towards the eruption column is almost purely horizontal. Thus, the humidity of air entrained into the eruption column is determined by the water vapour content at the respective height, there is no undersaturation lateral to the ascent zone. However, due to the low specific humidity at about 10 km, the increase of the total amount of condensed water ranges between only 1 and 5 % during the eruption.

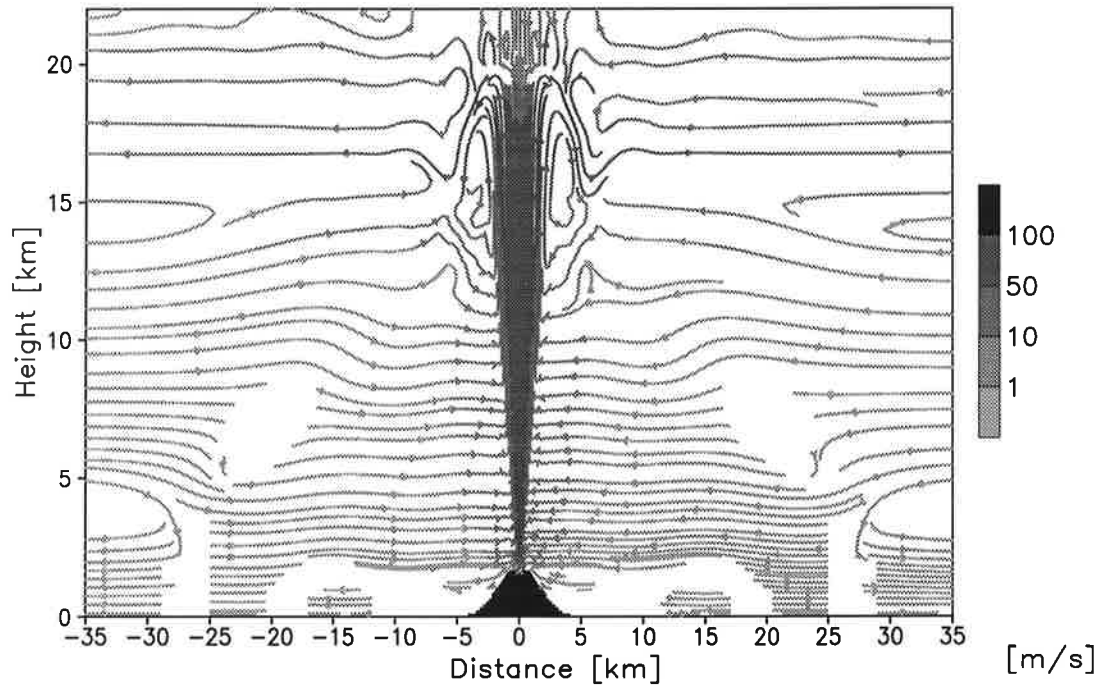


Figure 28: Streamlines of wind [m/s] after 30 min of the eruption in the experiment without particle-hydrometeor interactions DRY. Velocities smaller than 0.1 m/s are not shown.

Fig. (29) displays the vertical profiles of hydrometeors after 30 min of the eruption and another 30 min later, after the eruption ended. For comparison with the reference experiment see Fig. (20). During the eruption, most of the hydrometeors are solid with graupel being the most important category. Cloud ice is more common compared to the reference experiment. The radius of graupel in the umbrella cloud ranges from 100-500 μm leading to rather small fall velocities between 1 and 2 m/s and the vertical extension of the graupel plume is smaller than in the experiment REF. (This is also due to the relatively low density of 300 kg/m^3 assumed in our simulations for pure graupel.) At the end of our simulation period, the main portion of graupel is still situated above 10 km height.

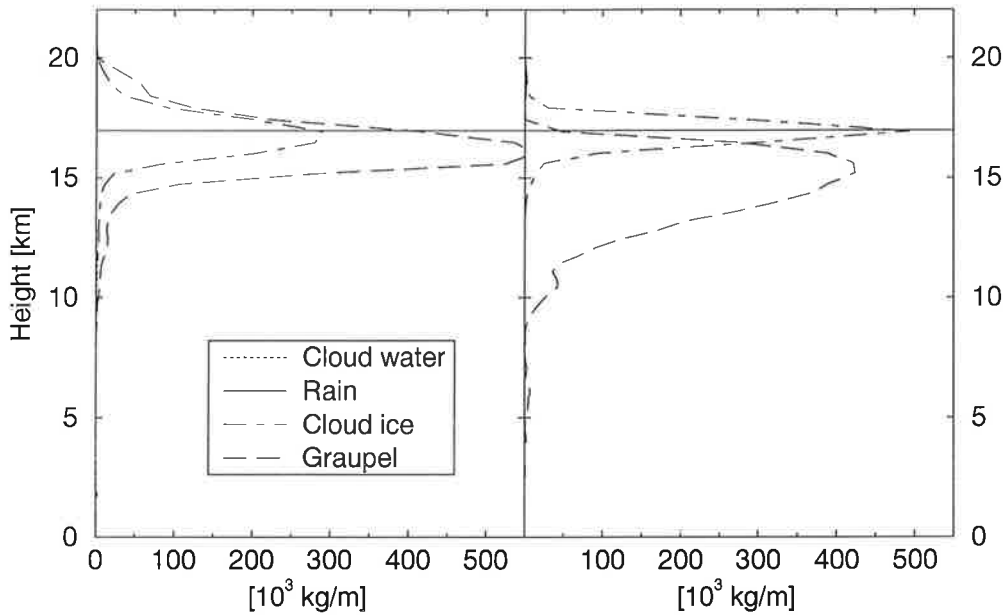


Figure 29: Vertical distributions of hydrometeors in [10^3 kg per m height] at 30 min of the eruption (left panel) and 30 min after the eruption ended in the experiment without particle-hydrometeor interactions DRY (right panel). The tropopause at 17 km is indicated by the thin horizontal line.

6.3.2 Size Distributions of Volcanic Particles

Two types of silicate particles are considered in our simulations. The mean volume radius of the particles erupted at the vent and the width parameter ν of the related size distributions are the subject of the sensitivity studies presented in this section. The parameters used in the simulations are displayed at the beginning of this chapter in Tab. (2).

The size distribution employed in the reference experiment has been fitted to the observational data obtained by *Carey and Sigurdsson (1982)*. This data might also include particle aggregates, which developed during the eruption inside the plume or post-eruptive, see Sect. (2.3). In the experiment ASH, only the small ash mode with $2.5 \mu\text{m}$ mean volume radius is erupted at the vent, with the same total mass eruption rate as in the reference experiment REF. In the experiment NAR, two particle classes with the same mean volume radius as in the experiment REF have been included. In REF, each mode was characterised by an exponential distribution with respect to the number concentrations ($\nu = 1$). In the experiment NAR, we assume a width parameter of $\nu = 10$ resulting in narrower size distributions. The initial size distributions of both experiments are illustrated in Fig. (30).

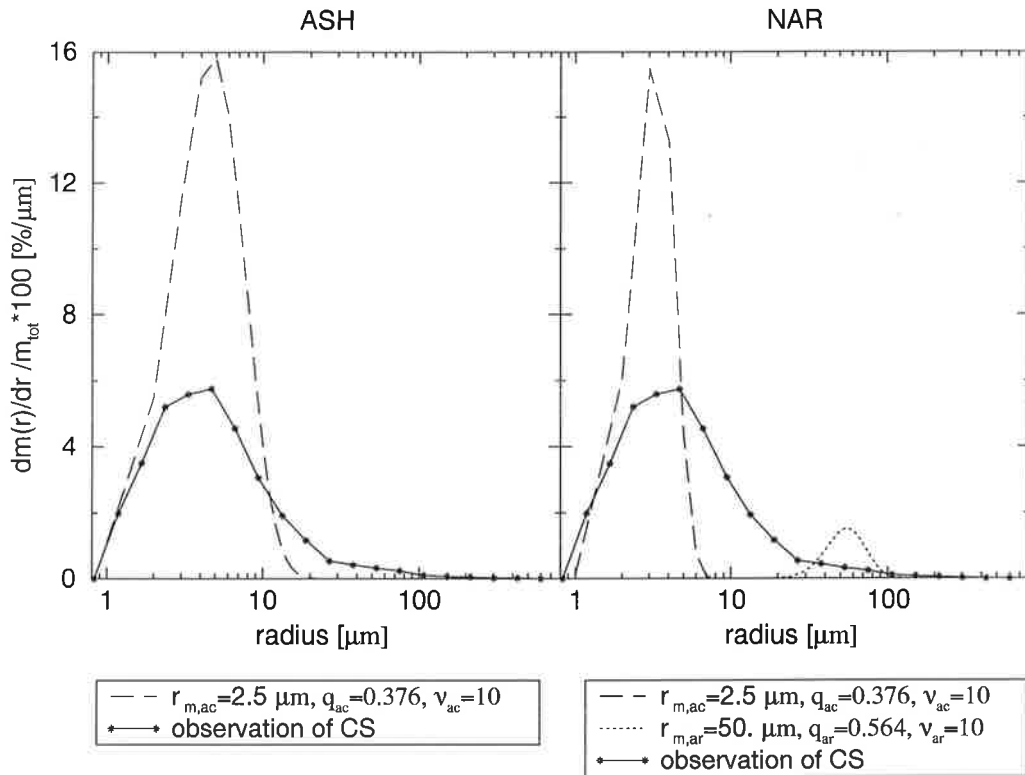


Figure 30: Initial mass distribution of volcanic particles: observations of *Carey and Sigurdsson* (1982) (CS) and the fitted distributions in the experiment ASH (left panel) and in the experiment NAR (right panel). Legend: r_m is the mean volume radius, q the specific mass and ν the width parameter of the size distribution. The indices *ac* and *cr* refer to the small and the large ash mode, respectively.

One would expect that the initialisation of a single small ash mode delays the evolution of larger aggregates since accretion processes are more effective for particles of different size. However, our simulation revealed that the particle radii are similar in the experiments REF and ASH. The huge supersaturation in the ascent zone leads to efficient condensation of water vapour: when reaching the umbrella region of the plume the aggregate sizes are already virtually identical in both experiments. The difference of the tropospheric graupel-like aggregate sizes shows an irregular pattern on the order of $\pm 500\mu\text{m}$. The plume shapes of hydrometeors and tephra look quite similar, and the time dependent fraction of volcanic gases and particles injected into the stratosphere or deposited at the ground level are like the pattern in the REF experiment that is illustrated in Fig. (16).

The experiment NAR, with narrower initial ash size distributions, also does not show any remarkable effect on the plume development. Fig. (31) displays the

vertical distributions of total ash for all the experiments considered in this study. The plume shapes and heights of the experiments ASH and NAR look quite similar to that of the reference experiment REF. Particle growth is so efficient, as argued for the experiment ASH, that neither the size difference between the two ash modes nor the different widths of the initial particle distributions have any effect on the plume shape in our simulations. The small initial differences are overwhelmed by the quick development of large aggregates in the eruption column.

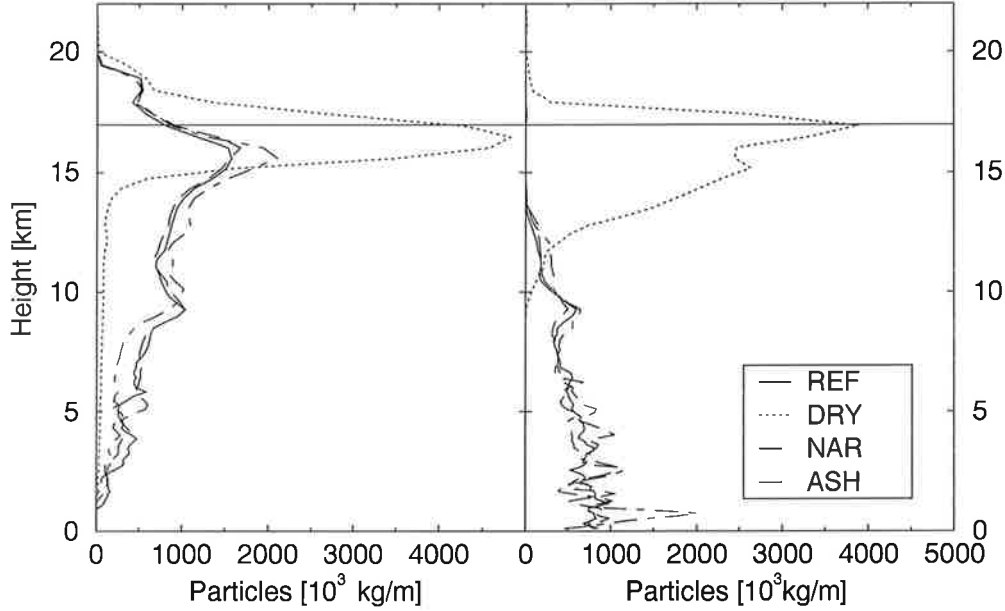


Figure 31: Vertical distributions of volcanic particles in [10^3 kg per m height] after 30 min of the eruption (left panel) and 30 min after the eruption ended (right panel) for all experiments. The tropopause at 17 km is indicated by the thin horizontal line.

The initial size distribution of volcanic ash erupted at the vent can not be directly observed. Instead, it has to be estimated from ash deposit data or remote sensing, as outlined in Sect. (2.3). The particles simulated in the framework of this research are rather fine grained, they do not include the concentrations of both the smallest and the largest ash. However, the information about the initial properties of ash is in general rather limited. Laboratory and field experiments could greatly improve the present knowledge about this topic.

A clear effect on the plume shape is only obtained from the experiment DRY, see Fig. (31). The consideration of particle-hydrometeor interactions is crucial for the simulation of volcanic eruption columns. Larger aggregates exhibit larger fall velocities than the initial individual ash particles, resulting in a completely different stratospheric injection and deposition fan.

The experiment REF, which includes the particle-hydrometeor interaction, is probably the more realistic experiment. Due to uncertainties concerning the formation and the stability of aggregates, the results obtained in this study may represent an upper limit of aggregate sizes as argued in Sect. (6.2.4). However, the parameterisation we applied is a first approach to describe ash particle growth processes in a volcanic plume and shows the general relevance of hydrometeor-ash interactions.

6.4 Scavenging of Volcanic Gases in the Plume

The fate of volcanic gases in the plume is the subject of this section. We focus on the three most important magmatic gases, HCl, SO₂ and H₂S. The chemical species are initialised in concentrations typical for a plinian eruption. In reality, the concentration of the sulphurous species is often higher than that of HCl, but we choose similar values for the volatiles in order to investigate their different behaviour in the plume. The gas ratios of HCl, SO₂ and H₂S are 0.01 mol/kg_{tot.mass}, i.e., about 1 wt.% of the gas fraction, respectively.

To begin with, we will introduce the behaviour of volcanic gases in the plume by describing the experiment REFS¹⁰, which is carried out under the conditions of the reference experiment REF, see Sect. (6.2). The occurrence of dissolved gases in hydrometeors leads to a depression of the water vapour saturation pressure and of the freezing point as explained in Sect. (3.12). The effect of salinity on the plume microphysics is shown in the second part of this chapter, when we compare the experiments REF and REFS. This feedback of gas scavenging on the microphysics is considered in all the experiments performed in this chapter. Particle coagulation due to hydrometeor-ash interaction influences the distribution of volcanic gases in the atmosphere. We examine this effect by comparing the experiment REFS with an experiment called DRYS,¹¹ using the parameters of DRY given in Sect. (6.3.1) plus salinity effects. The impact of incorporating volcanic gases into frozen particles on the scavenging ratio is analysed through a simulation, NOINC¹², not taking this process into account. The experiments concerning the scavenging of volcanic gases in the plume are listed in Tab. (3).

	REF	REFS	DRYS	NOINC
salinity effect	-	+	+	+
particle - hydrometeor interaction	+	+	-	+
incorporation of gases in ice	-	+	+	-

Table 3: Scavenging of volcanic gases in the plume:
Parameters for sensitivity studies.

¹⁰ REFS: experiment REFerence for gas Scavenging.

¹¹ DRYS: experiment DRY for gas Scavenging.

¹² NOINC: NO direct INCorporation of gases into ice.

6.4.1 Behaviour of Volcanic Gases in the Plume

The experiment REFS is carried out under the same conditions as the reference experiment REF described in Sect. (6.2). The salinity effect is included as well as the incorporation of volcanic gases in frozen hydrometeors as described in Sect. (4.2).

Plume Shapes and Vertical Profiles

The plumes of total HCl and SO₂ after 30 min of the eruption are illustrated in Fig. (32) and Fig. (33). Both plumes penetrate into the stratosphere – overshooting their stationary heights at the tropopause level – however, they show a rather different shape. The HCl plume looks similar to that of ash or hydrometeors, see Fig. (10) and Fig. (19). It has a comparatively large horizontal extension along the entire vertical axis of the eruption column, because the highest portion of HCl is scavenged by falling particles due to its large water solubility. The plume of SO₂ is similar to the inert gas plume, see Fig. (11): most of the SO₂ remains in the gaseous phase and spreads horizontally in the tropopause region. The behaviour of the sulphurous species SO₂ and H₂S in the plume is very similar since both species are only slightly soluble in liquid water. The difference of the scavenging ratio is therefore only dependent on the respective efficiency of incorporation into ice. The efficiency factors of the sulphur gases are similar, see Eq. (87). Hence, we show results only for SO₂ here.

The vertical distributions of HCl and SO₂ after 30 min of eruption, shown in Fig. (34), highlight the different behaviour of HCl and SO₂ in the plume. Significant amounts of gaseous HCl occur only in the central rising zone of the plume with temperatures too high for liquid water to condense. The amount of HCl in liquid water drops is lower than expected from its high water solubility, because of the fast plume rise to regions with temperatures too low for liquid droplets to exist. The highest portion of hydrometeors occurs in frozen categories as shown in Sect. (6.2.2). Hence, the largest portion of HCl is contained in graupel-aggregates and precipitates towards lower heights. The HCl content in cloud ice, which nucleates in the umbrella region, is rather low since HCl is no longer present in the gas phase but has already been scavenged at lower altitudes. The main part of the sulphurous species stays in the gas phase being suspended in the umbrella region. SO₂ is not removed from the gas phase by liquid drops in the lower plume areas because of its lower water solubility. Instead, it is incorporated into cloud ice and graupel by direct gas transfer during diffusional ice growth in higher plume regions. In contrast to HCl, scavenging of SO₂ by cloud ice and graupel is of similar importance.

The increased gaseous concentrations between 2 and 12 km in Fig. (34) indicate the degassing from falling hydrometeors next to the ascent zone, especially in the case of HCl. The sedimentation and subsequent melting of contaminated graupel below 5 km leads to the occurrence of highly concentrated rain droplets at the sides of the plume, where the concentrations of volcanic species in the gas phase are lower than inside the plume. This leads to revolatilisation of gases according to Henry's law. Moreover, the capacity of drops to retain dissolved gases decreases exponentially with increasing temperature according to Eq. (73). Transport of contaminated hydrometeors to regions that are undersaturated with respect to water vapour, see Fig. (17), leads to their evaporation, thus completely releasing volcanic species, that have been scavenged in upper parts of the plume back to the atmosphere.

The post-eruptive vertical distributions of HCl and SO₂ half an hour after the eruption ended are displayed in Fig. (35). The HCl-plume collapsed, now exhibiting the highest content in the lower troposphere. Contrarily, SO₂ has continued its lateral expansion, only a minor portion of sulphur containing gases can be found below 15 km. Both species are mainly present in the gas phase, though at different altitudes. The highest portion of HCl now occurs in the lower troposphere: dissolved HCl has been transported by falling aggregates to lower altitudes where it is released into the gas phase and accumulates during our simulation, as mentioned previously. A smaller fraction of HCl remains in graupel. Liquid cloud and rain water occurring below 5 km height is far away from the crater region: due to the low HCl-gas content in these areas the liquid water contamination with HCl is rather small. A little peak of HCl in the gas as well as in the ice cloud occurs at the tropopause region: as mentioned before in Sect. (6.2), gas-particle separation leads to a stable cloud of volcanic material suspended in the air after the eruption ended. The main portion of SO₂ stays at tropopause height, because the scavenging of sulphurous species, which would result in transfer to lower levels is comparatively inefficient. The updraft in the central plume region leads to post-eruptive stratospheric injection of volcanic species. The SO₂-gas peak at about 5 km is due to revolatilisation from falling hydrometeors, as described above for the HCl plume.

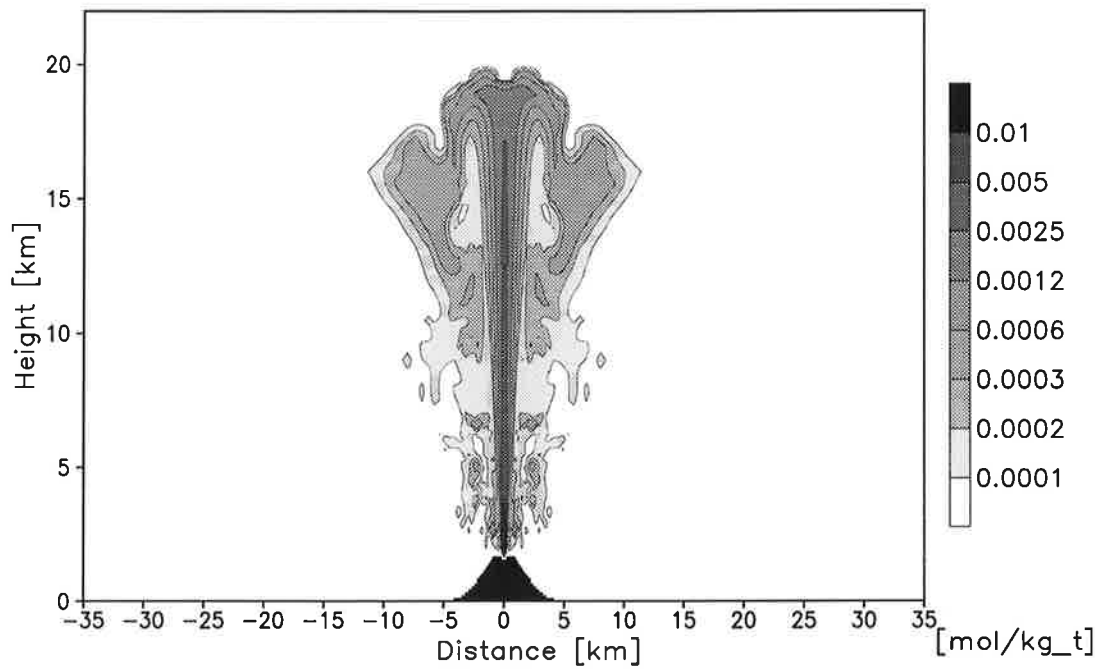


Figure 32: Plume of total HCl in $[\text{mol}/\text{kg}_{\text{totalmass}}]$ at 30 min of the eruption in the experiment REFS.

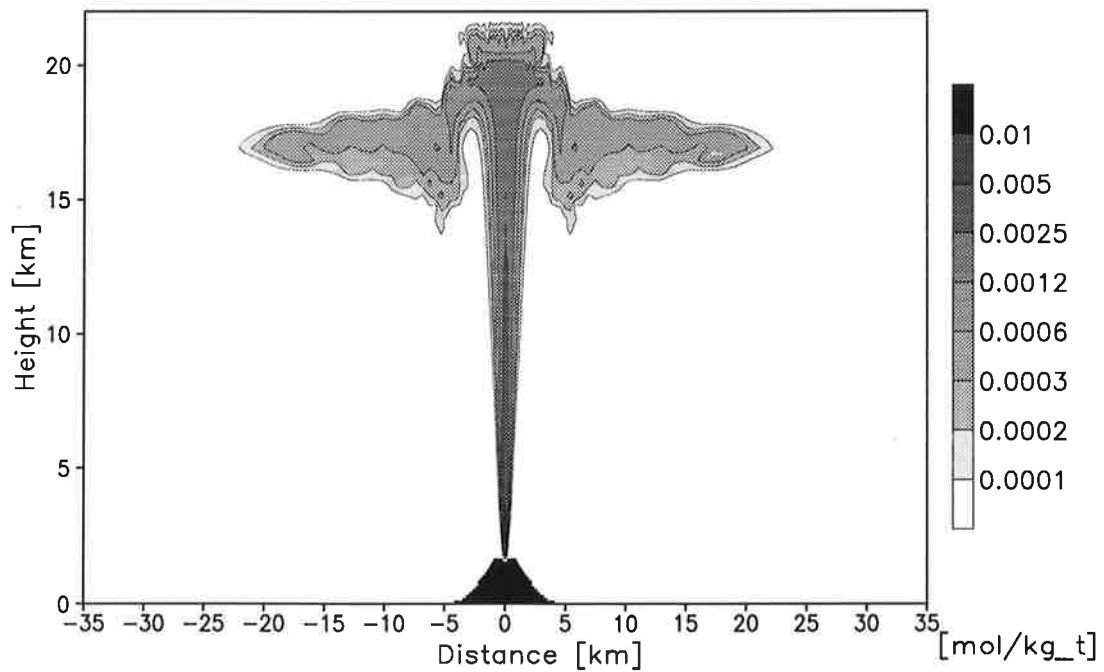


Figure 33: Plume of total SO_2 in $[\text{mol}/\text{kg}_{\text{totalmass}}]$ at 30 min of the eruption in the experiment REFS.

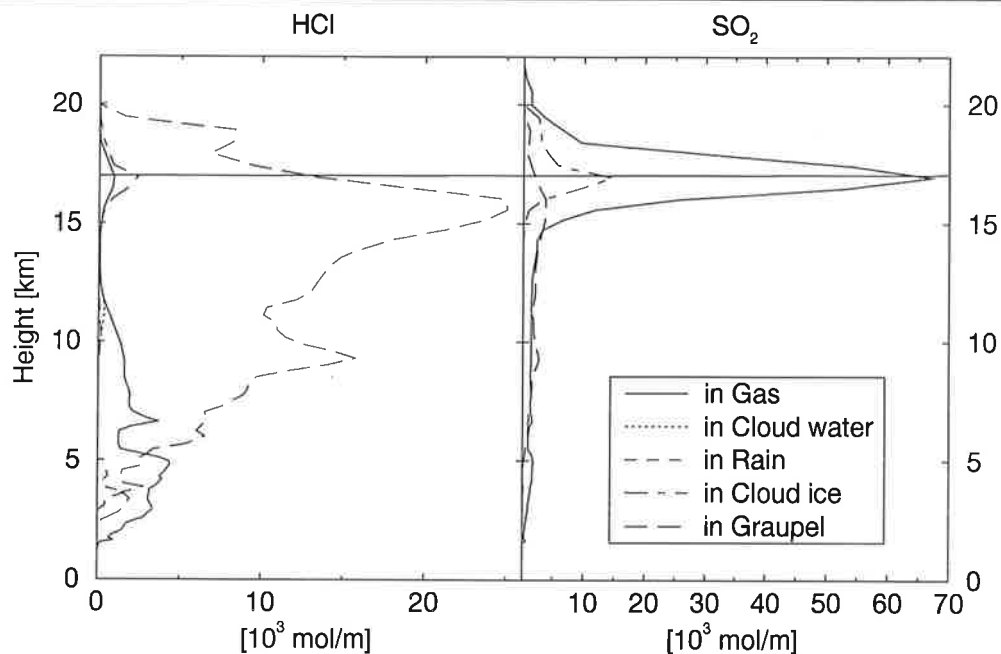


Figure 34: Vertical distributions of volcanic species in [10^3 mol per m height] at 30 min of the eruption in the experiment REFS for HCl (left panel) and SO_2 (right panel). The tropopause at 17 km is indicated by the thin horizontal line.

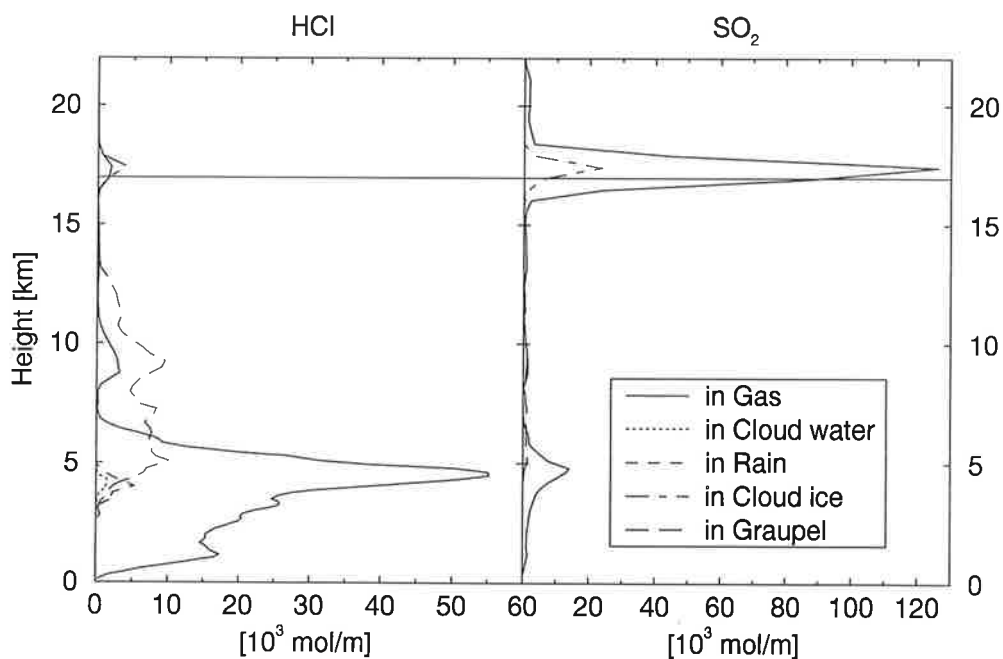


Figure 35: Vertical distributions of volcanic species in [10^3 mol per m height] 30 min after the end of the eruption in the experiment REFS for HCl (left panel) and SO_2 (right panel). The tropopause at 17 km is indicated by the thin horizontal line.

Concentration of Volcanic Species in Different Hydrometeors

The concentration of volcanic gases in different hydrometeor types is discussed in this section. The volcanic emission of magmatic volatiles at the vent leads to extremely high gas concentrations in the central rising zone, ranging between 50 and 100 ppmv¹³. Condensation of liquid water above 10 km height reduces the gaseous concentration of HCl in the central plume zone by about three orders of magnitude. Consequently, the liquid water is highly contaminated with HCl: its concentration in cloud water varies between 0.01 and 1 mol/l resulting in a pH-value between 0 and 2 as shown in Fig. (36).¹⁴ The sulphurous gases are hardly scavenged by water, their concentration in cloud and rain drops ranges only between 10^{-5} and 10^{-3} mol/l, and the concentrations of SO₂ and H₂S in the gas phase are not considerably reduced.

Fig. (37) to Fig. (40) show the concentrations of HCl and SO₂ in cloud ice and graupel¹⁴ after 30 min of the eruption. The most striking feature is the high concentration of HCl in graupel in the central plume (Fig. (37)), that cannot be found in the corresponding figure for SO₂ (Fig. (38)). On the contrary, cloud ice in the central rising zone is contaminated with SO₂ but not with HCl, see Fig. (40) and Fig. (39). The presence of volcanic gases in solid hydrometeors can be caused by dissolution in liquid droplets which freeze subsequently, or by direct gas uptake during ice particle growth. Direct gas uptake would lead to a sulphur-content in graupel that is 3 to 4 times lower than that of HCl due to the ratios of the uptake efficiency factors $f_{inc,c}$ for the different species given in Eq. (87). However, the HCl-content in graupel is much higher than could be expected from direct gas uptake. Thus, HCl seems to be efficiently scavenged by liquid droplets at temperatures above the freezing point in the central ascent zone at about 10 km. These drops freeze to ice and grow to highly HCl-contaminated graupel-aggregates during the ascent of the plume. Directly above the freezing height in the central plume, HCl is so efficiently removed from the gas phase by scavenging in liquid drops that cloud ice forming in this region does not contain HCl. However, SO₂ (and H₂S which is not shown here) is incorporated in the cloud ice by direct transfer from the gas phase depositing simultaneously with water vapour. The highest SO₂ concentration occurs at the top of the

¹³ parts-per-million by volume.

¹⁴ The species concentration inside a hydrometeor is derived from the ratio of the species content and the hydrometeor content:

$$mol/kg_{hydrometeor} = \frac{mol/kg_{tot.mass}}{kg_{hydrometeor}/kg_{tot.mass}} \quad (91)$$

Hydrometeor contents smaller than $q = 10^{-5} g/kg_{tot.mass}$ are not relevant and the concentration of chemicals contained is not plotted. A relatively high species concentration in these little amounts of water or ice leads to the angular structure of the resulting plots.

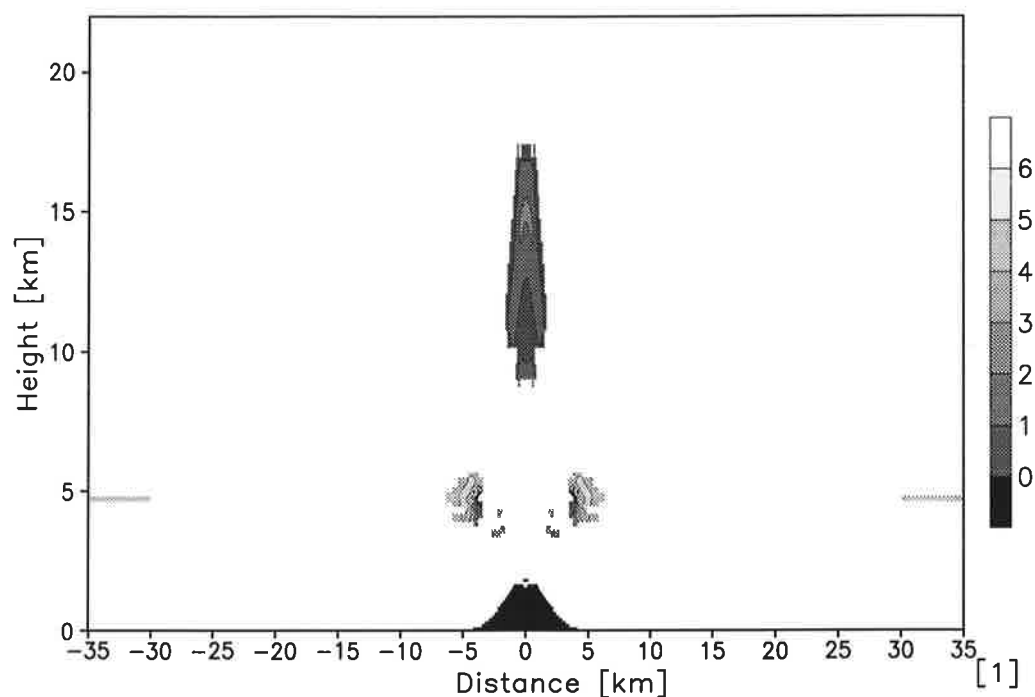


Figure 36: pH-value in cloud water
at 30 min of the eruption in the experiment REFS.

plume resulting from strong diffusional growth in the central ascent zone. In the umbrella region and in the lateral branches of the graupel plume, the HCl concentration is slightly higher suggesting that graupel was also formed by water vapour growth.

The different scavenging mechanisms for the volcanic gases deliver additional information about the development of frozen hydrometeors. High HCl and low sulphur contamination indicates development via the liquid phase, whereas high sulphur concentration implies diffusional growth. In the central rising zone and in the umbrella region, diffusional growth is likely due to high relative humidity, see Fig. (17). This is confirmed by the high sulphur loadings of cloud ice within these regions. On the other hand, graupel in the central rising zone results predominantly from freezing of droplets that developed at about 10 km height.

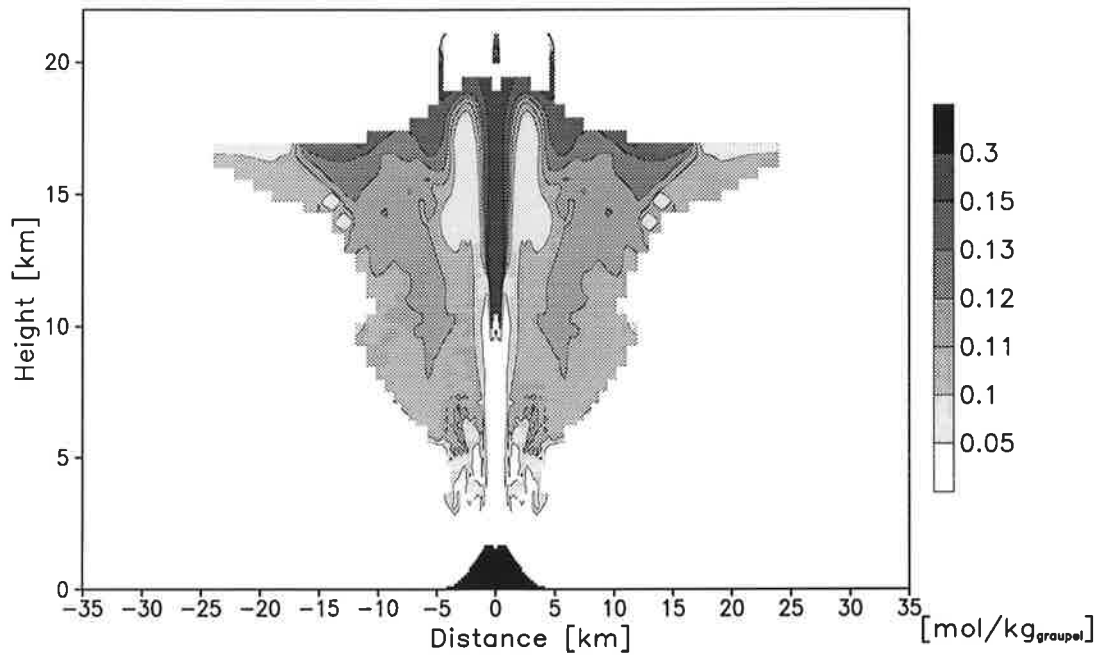


Figure 37: Concentration of HCl in graupel in $[\text{mol}/\text{kg}_{\text{graupel}}]$ at 30 min of the eruption in the experiment REFS.

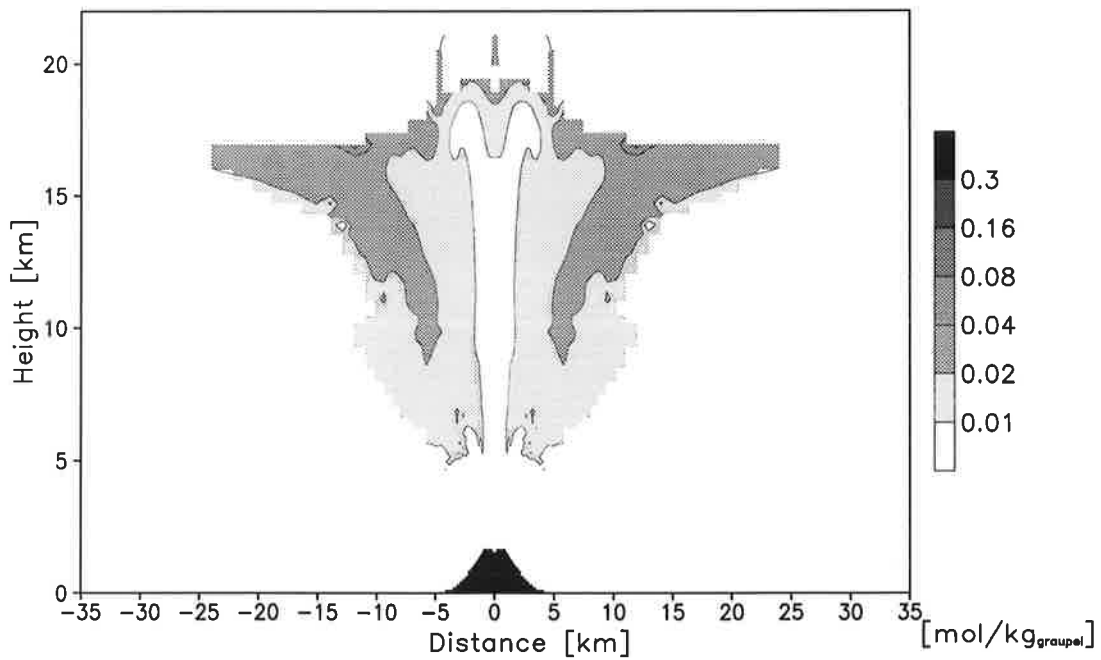


Figure 38: Concentration of SO_2 in graupel in $[\text{mol}/\text{kg}_{\text{graupel}}]$ at 30 min of the eruption in the experiment REFS.

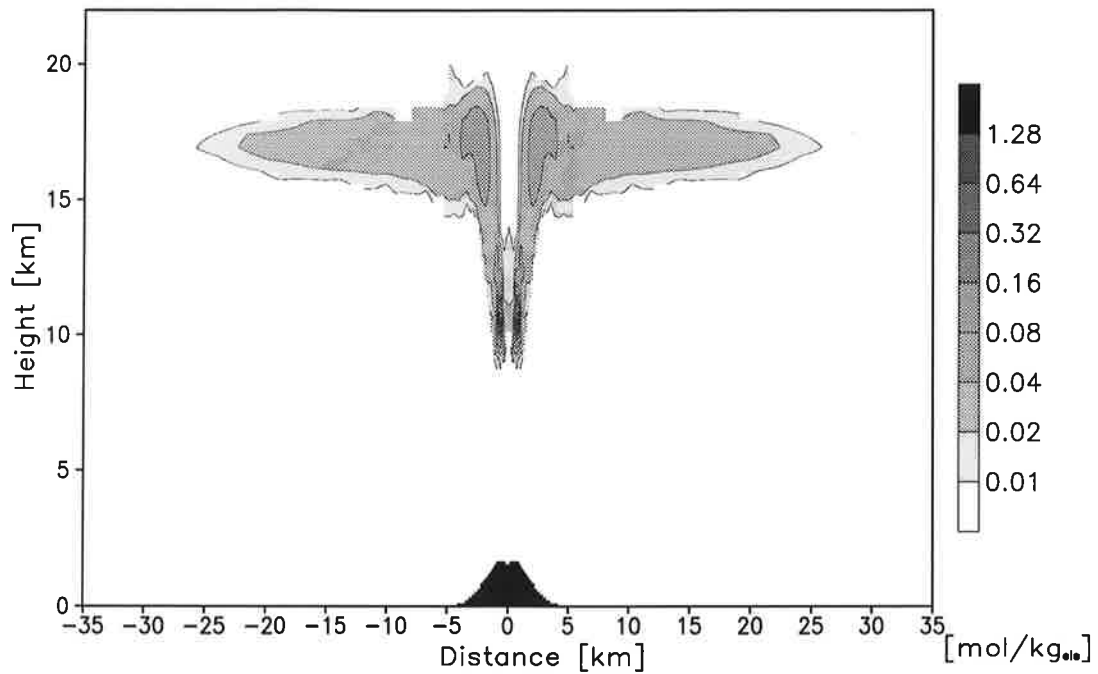


Figure 39: Concentration of HCl in cloud ice
in $[\text{mol}/\text{kg}_{\text{ice}}]$ at 30 min of the eruption in the experiment REFS.

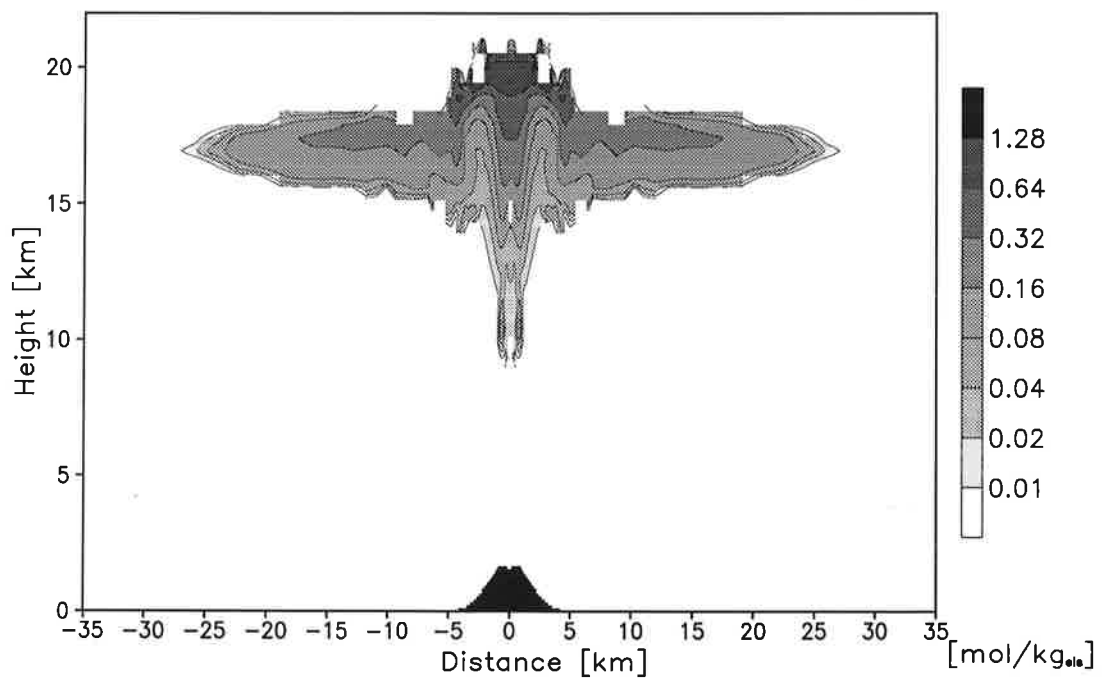


Figure 40: Concentration of SO_2 in cloud ice
in $[\text{mol}/\text{kg}_{\text{ice}}]$ at 30 min of the eruption in the experiment REFS.

Temporal Development

Fig. (41) displays the temporal development of the fraction of volcanic volatiles in the gas phase and in the different types of hydrometeors, summing up the species content in the whole model domain. The gaseous concentration of HCl

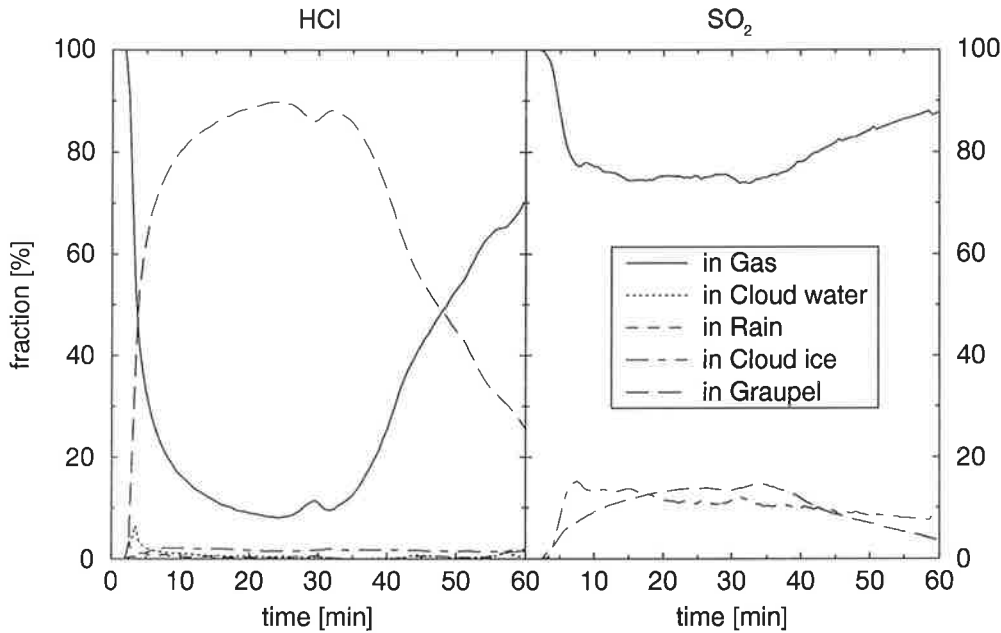


Figure 41: Temporal development of the fraction of volcanic species in different phases, in [%] of total species amount in the whole model domain. HCl (left panel) and SO₂ (right panel) in the experiment REFS.

(left panel) originally erupted at the vent is diminished to $\sim 40\%$ of all the HCl in the plume after 5 min of the eruption. It is partly dissolved in liquid droplets, which evolve above the crater region as indicated by the small peak in the cloud water fraction. At the same time, solid hydrometeors develop from drop freezing and from water vapour deposition on ash particles, most of them occurring in the larger graupel-aggregate mode. Freezing transfers the HCl contained in drops into the respective frozen category. The ratio of total HCl in graupel quickly increases to about 90% diminishing the gaseous HCl fraction to about 10% of the total amount. The HCl fraction in the other hydrometeor classes is relatively insignificant contributing less than 5% HCl. After ~ 25 min of eruption time, the graupel-aggregates have fallen down to sufficiently low altitudes, that the revolatilisation of HCl in the troposphere caused by melting and evaporation begins. By the end of our simulation time, half an hour after the eruption stopped, about 70% HCl has returned to the gas phase, whereas its fraction in graupel has decreased to about 30% of the total amount of HCl in the plume.

The sulphur containing species show a different image. Gaseous SO_2 is barely reduced by the occurrence of liquid water. Instead, it is directly incorporated into solid hydrometeors, both cloud ice and graupel. The SO_2 fraction in cloud ice and graupel is about 15 % each. This leads to a cutback of the gaseous sulphur species to approximately 70 % of all the SO_2 in the plume. After the eruption ends, revolatilisation of some of the SO_2 in graupel leads to an increase of the gaseous fraction of up to 90 % of the total SO_2 in the model domain. These results indicate that the scavenging by (supercooled) liquid droplets is not the only mechanism that removes volcanic volatiles from the gas phase. Our study reveals that the incorporation of volcanic species in frozen hydrometeors is also of considerable significance, especially for the sulphur species.

The fraction of volcanic HCl , SO_2 and H_2S in the stratosphere is illustrated in Fig. (42). For comparison, the stratospheric fraction of an inert gas, which does not interact with hydrometeors but is passively transported with the mean flow, has been included in this figure. Species once scavenged by hydrometeors tend to

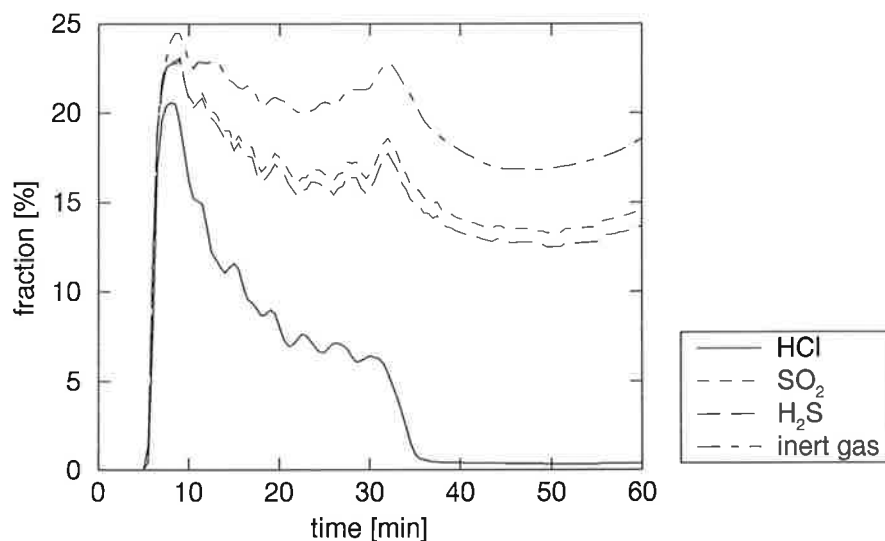


Figure 42: Temporal development of the fraction of volcanic species injected into the stratosphere in [%] of total mass erupted at the vent in the experiment REFS.

sink and will stay in the troposphere. Transport of contaminated hydrometeors to lower altitudes leads to the release of volcanic gases back to the atmosphere as described at the beginning of this section. The stratospheric injection of the volcanic species under consideration starts about 5 min after the eruption's onset and reaches its maximum fraction of 20 to 25 % with higher values for the inert gas and the sulphurous species at ~ 10 min. The evolution of hydrometeors results in scavenging processes efficiently removing HCl from the stratosphere. Fig. (43) shows that by far the highest portion of HCl in the stratosphere is contained

in graupel. Shortly after the eruption ends, only 0.3% of the total HCl emitted remains in the stratosphere. This is equivalent to an input of ~ 80 tons per hour for a continuous eruption.

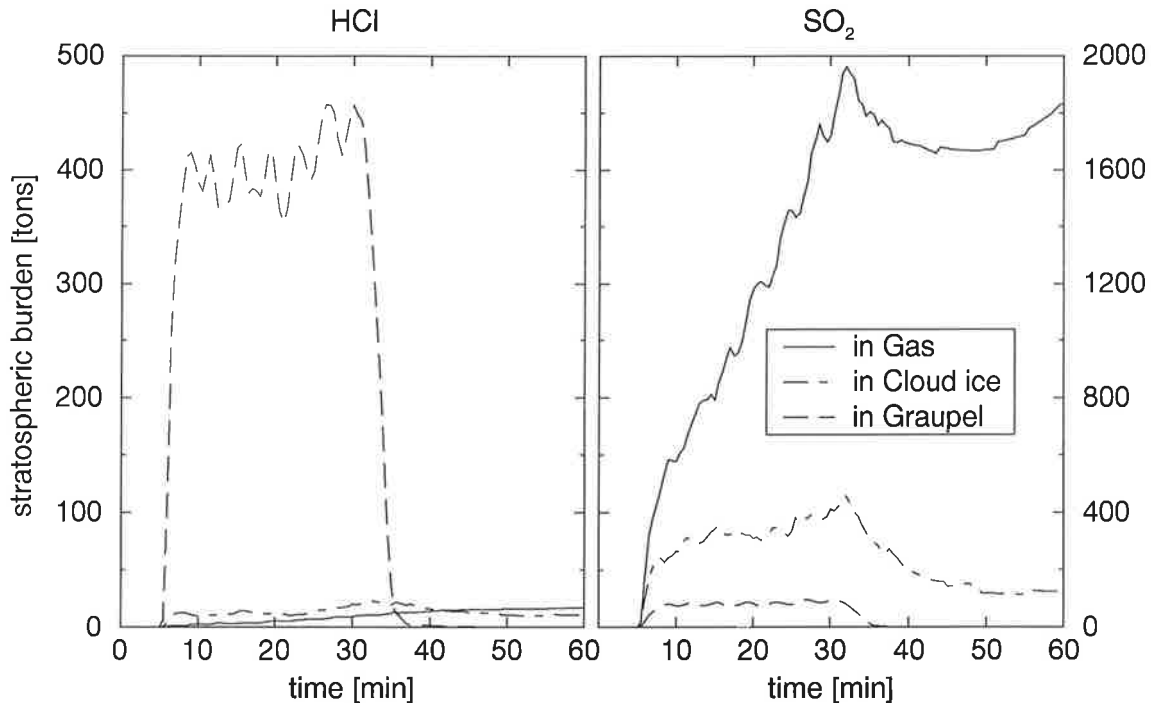


Figure 43: Temporal development of stratospheric burden of volcanic species in [tons] for HCl (left panel) and SO₂ (right panel) in the experiment REFS.

On the other hand, the initial stratospheric fractions of SO₂ and H₂S in the stratosphere are not considerably reduced: the gas phase is the dominant phase of stratospheric sulphur species as illustrated in Fig. (43). During the eruption, about 25 % and less than 10 % of the stratospheric sulphur is incorporated into cloud ice and graupel, respectively. After the eruption ended, graupel sediments towards the troposphere also removing a minor portion of included sulphur species from the stratosphere, see Fig. (42). The gaseous fraction in the stratosphere increases further at the expense of the ice phase. At the end of our simulation, about 15 % of the total sulphur gases emitted at the vent remain in the stratosphere. We obtain a stratospheric injection of ~ 8000 and ~ 4400 tons per hour for SO₂ and H₂S, for a continuous eruption. The stratospheric input of the inert gas is ~ 20 % of its total emitted mass at the end of our simulation period. Hence, scavenging processes almost prevent the stratospheric injection of HCl, and they also reduce the input of sulphur species, which are diminished by about one quarter of the potential amount given by the injection of the inert gas.

6.4.2 Salinity Effect

Fig. (44) shows the temporal development of hydrometeors integrated over the whole model domain without and with consideration of the salinity effect in the experiments REF and REFS. The importance of the different hydrometeor classes during our simulation is very similar in both experiments: by far the highest portion of hydrometeors is frozen to ice particles due to the fast ascent of the plume. This means, that the impact of dissolved species on the hydrometeor content in a volcanic plume is only of minor importance. In most parts of the eruption column, the species concentrations in hydrometeors is below $1 \text{ mol/kg}_{\text{hydrometeor}}$, i.e., a mole fraction of about $2 \cdot 10^{-2}$. This leads to a depression of the water vapour saturation pressure and to a lowering the freezing point of about 1-2 %, see Eq. (68) and Eq. (69). The species concentration inside the hydrometeors is too low to cause considerable depression of the water vapour pressure and the freezing point.

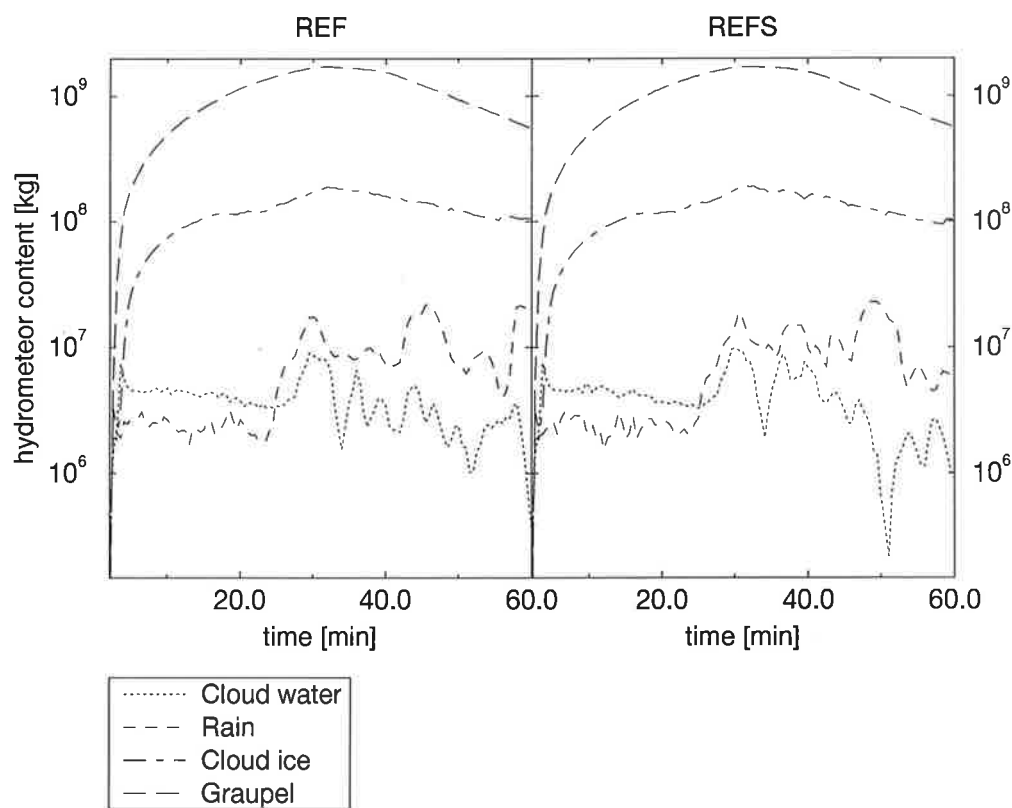


Figure 44: Temporal development of the hydrometeor content integrated over the whole model domain without salinity effect in the reference experiment REF (left panel) and with salinity effect in the experiment REFS (right panel).

The effects of salinity obtained cannot be seen as quantitatively exact, because of the assumption of ideal behaviour. For example, the freezing point depression in an HCl solution in water is stronger than expected from the ideal linear dependence on the concentration of HCl in water (*Dominé and Thibert, 1997*). The droplets in a volcanic plume, however, do not consist of single electrolyte solutions, they contain a variety of non-quantified species that may act synergistically in a non predictable way on the activity coefficients, i.e., on the salinity effects as explained in Sect. (3.12). The simulated volcanic eruption takes place in a rather humid environment in the tropics, resulting in a relatively high amount of condensed hydrometeors. Therefore, the solution concentration, and along with that the salinity effects, are not very significant. However, in an arid climatic zone and for an erupting mixture with low water vapour and higher species content, this it may be more important.

6.4.3 Effect of Ash Particle Growth on the Scavenging Ratio

This section deals with the effect of particle-hydrometeor interactions on the scavenging ratio. We compare the experiment REFS with the experiment DRYS in which particle-hydrometeor interactions are not taken into account. The experimental conditions and results of the corresponding experiments REF and DRY are described in Sect. (6.2) and Sect. (6.3.1).

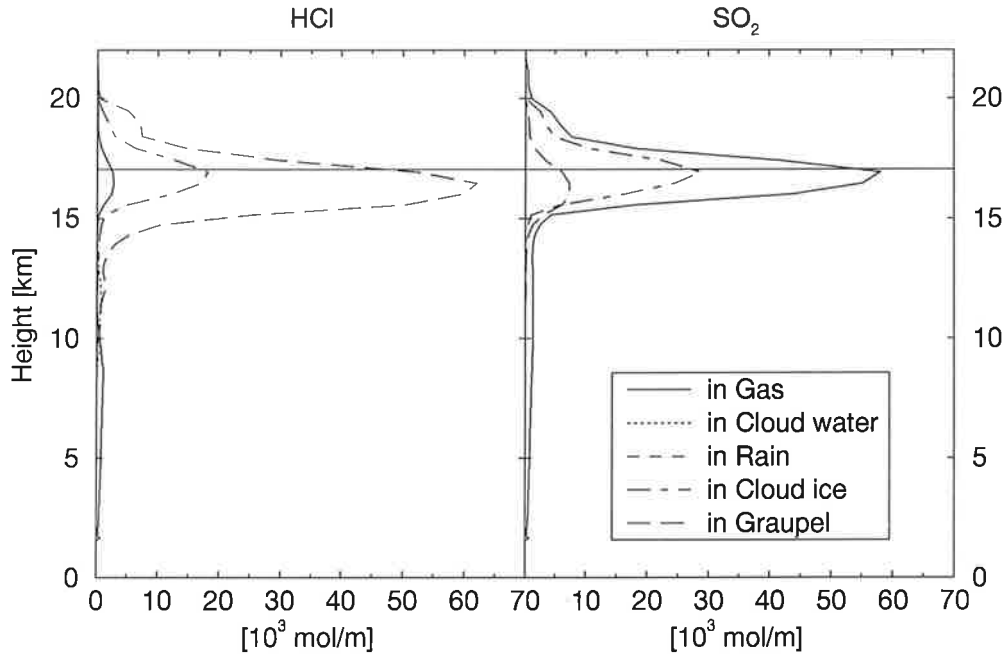


Figure 45: Vertical distributions of volcanic species in [10^3 mol per m height] at 30 min of the eruption in the experiment DRYS for HCl (left panel) and SO_2 (right panel). The tropopause at 17 km is indicated by the thin horizontal line.

The vertical distributions of HCl and SO_2 after half an hour of eruption in the experiment DRYS are depicted in Fig. (45). In correspondence to the related hydrometeor distributions shown in the left panel of Fig. (29), which exhibits very few falling hydrometeors, a great portion of all chemical species, including HCl, reaches high altitudes. Revolatilisation in the troposphere does not occur during our simulation time since the hydrometeors stay mostly above the 10 km height.

The fraction of volcanic species in different phases as a function of time is illustrated in Fig. (46). The HCl scavenging is of similar efficiency, whereas the removal of sulphurous species from the gas phase increases as compared to the experiment REFS, see Fig. (41). At the beginning of our simulation, 5 min after the eruption has begun, the scavenging of HCl in cloud water contributes

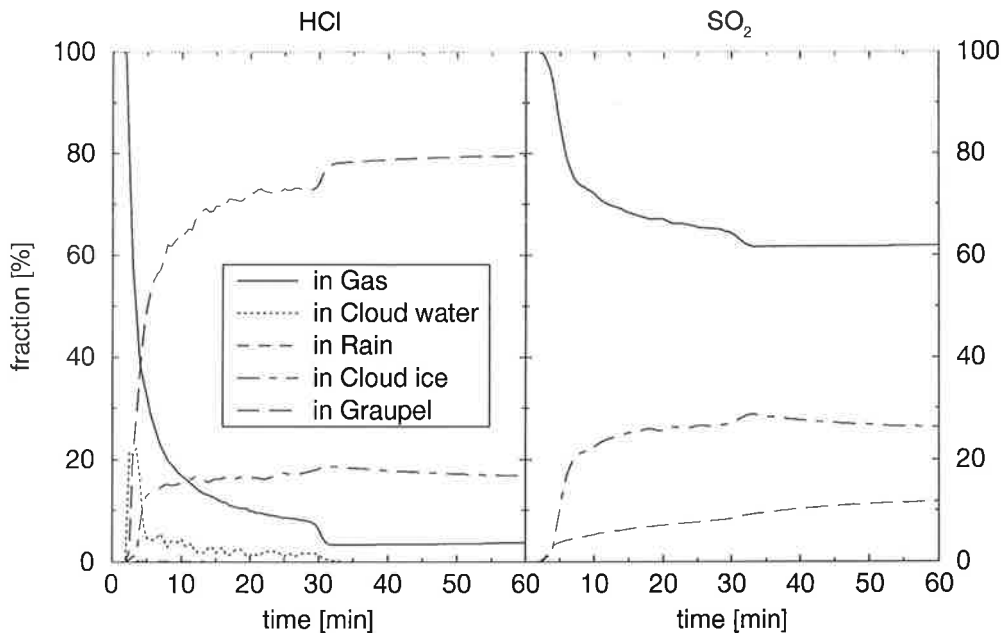


Figure 46: Temporal development of the fraction of volcanic species in different phases, in [%] of total species amount in the whole model domain. HCl (left panel) and SO₂ (right panel) in the experiment DRYS.

up to 20% to the total amount in the plume. This is twice as much as in the experiment REFS, although the amount of liquid water has not significantly increased. In the experiment DRYS the formation of raindrops is initially limited to autoconversion of newly formed cloud drops. This is in contrast to the experiment REFS, where condensation of water vapour on the two ash classes results in simultaneous evolution of cloud and rain drops. The smaller drop size in the experiment DRYS might lead to a higher phase transfer rate which results in the higher efficiency of HCl dissolution. Freezing of cloud water and rain causes the production of cloud ice and graupel, again with more hydrometeors in the smaller category. Consequently, cloud ice has a greater importance with respect to scavenging processes, but the overall removal of HCl from the gas phase is similar to that in the experiment REFS.

The direct incorporation of chemicals from the gas phase into frozen hydrometeors is enhanced when compared to the experiment REFS. The flow pattern in the experiment DRYS, shown in Fig. (28), leads to the entrainment of ambient air that is characterised by a relatively higher specific humidity; this is caused by the lack of subsidence at the sides of the plume we saw in the experiment REFS, see Fig. (15). Increased supersaturation in the central rising zone above 10 km causes increased deposition of water vapour on ice particles. In addition, the smaller particles in DRYS have a relatively larger surface also preferring dif-

fusional growth. This is most significant for the sulphur species: their fraction in the gas phase decreases to $\sim 60\%$ (REFS – 10%) of the total amount in the model domain.

Fig. (47) illustrates the fraction of volcanic species injected into the stratosphere during the experiment DRYS. The stratospheric injection of HCl has increased by five times as compared to the experiment REFS, because of the decreased sedimentation of hydrometeors. The stratospheric injection is now 1.5% of the total HCl emission, or ~ 400 tons per hour. Neglecting the interactions between hydrometeors and ash particles leads to a reduction in the sulphur input. The reason for this is the decreased gas-particle separation in DRYS as discussed for the inert gas in Sect. (6.3.1), which results in a reduced upwards motion of the gas plume thus reducing the stratospheric gas injection. The increased scavenging by hydrometeors has no additional effect, because the ice particles are quasi suspended in the air, the sulphur input equals that of the inert gas. The stratospheric injection has decreased by about two thirds to 5% of the total amount of sulphur in the model, i.e., an injection of ~ 2700 tons per hour SO_2 and ~ 1400 tons per hour H_2S .

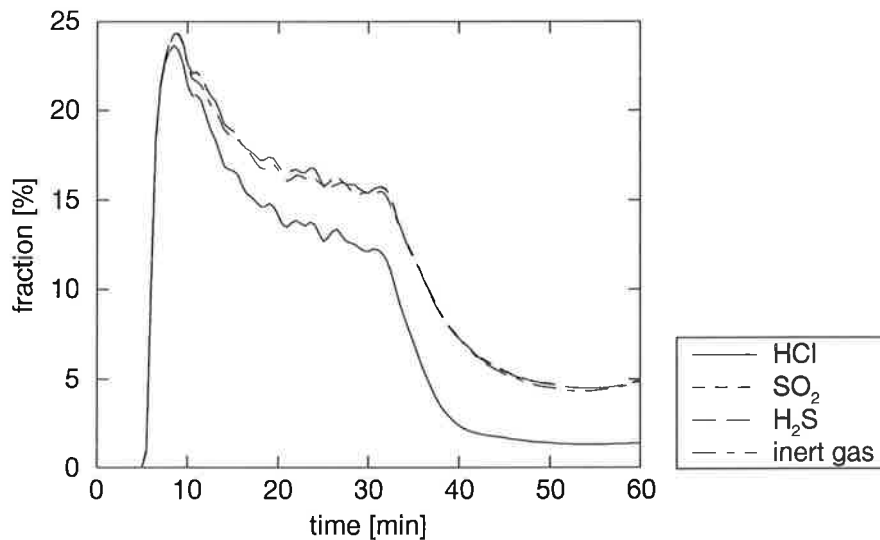


Figure 47: Temporal development of the fraction of volcanic species injected into the stratosphere in [%] of total amount erupted at the vent in the experiment DRYS.

6.4.4 Incorporation of Volcanic Gases into Ice

The consequences of considering the direct transfer of volcanic volatiles from the gas phase into ice particles is examined in this section by comparing the experiments REFS and NOINC. Eliminating gas incorporation does not considerably change the situation for HCl as depicted in Fig. (48) which shows the vertical distributions of HCl and SO₂, after 30 min of eruption. The concentration of HCl in graupel – the most important reservoir for this species – is very similar in both experiments, see also Fig. (34) for comparison with the experiment REFS. This result confirms the statement in the previous section: HCl is mainly scavenged by liquid water drops in the central rising zone, and subsequent freezing of these drops transfers it into graupel-aggregates. Cloud ice at the tropopause level is somewhat less polluted with HCl compared to the experiment REFS, hence, slightly more HCl remains in the gas phase (REFS: ~ 11 % and DRYS: ~ 12 % of the total amount). On the other hand, neglecting direct incorporation of volcanic volatiles has a clear effect on the distribution of sulphur species. Since they are practically insoluble in liquid water, they stay almost completely in the gas phase.

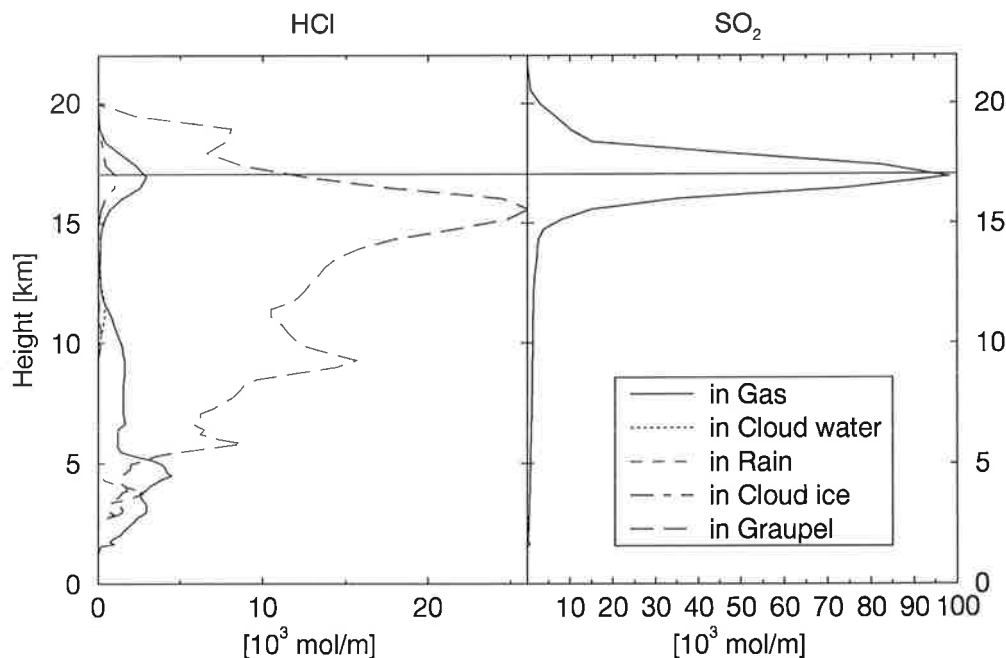


Figure 48: Vertical distributions of volcanic species in [10^3 mol per m height] at 30 min of the eruption in the experiment NOINC for HCl (left panel) and SO₂ (right panel). The tropopause at 17 km is indicated by the thin horizontal line.

The fraction of volcanic species in relation to the total amount erupted at the vent, that has been injected into the stratosphere during our simulation is shown in Fig. (49). Neglecting direct transfer of HCl into ice particles increases its stratospheric injection by a factor of two, its input in the experiment NOINC is about 0.6% of the total emitted HCl, i.e., ~ 160 tons per hour. Without direct incorporation of SO_2 and H_2S into growing ice crystals these species exhibit stratospheric injections like the inert gas. The input of sulphurous species increases by about one third to $\sim 20\%$ of the total amount of sulphur compounds ejected by the volcano. In terms of mass injection, the rate in tons per hour is $\sim 10\,700$ for SO_2 and $\sim 5\,700$ for H_2S .

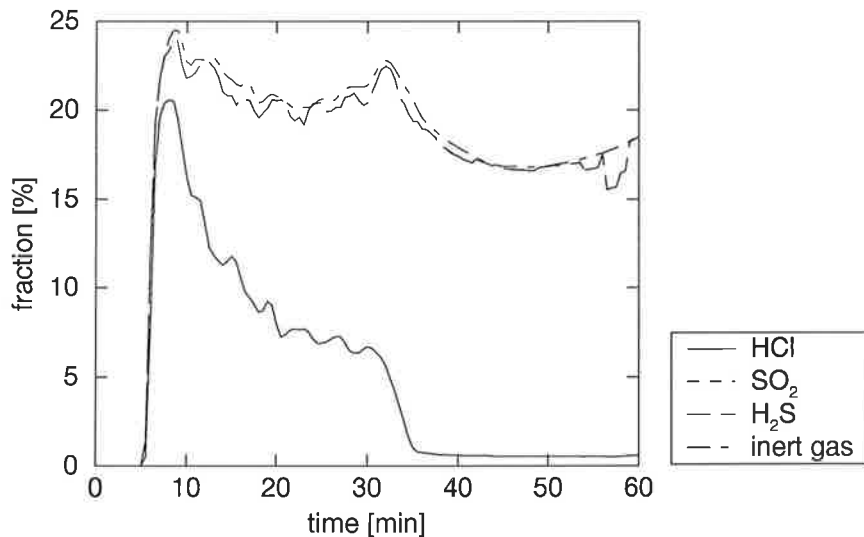


Figure 49: Temporal development of the fraction of volcanic species injected into the stratosphere as a function of time in [%] of total mass erupted at the vent in the experiment NOINC.

Observational data support the proposed mechanism of gas scavenging by growing ice particles in a volcanic plume. The eruptions of Rabaul in 1994 and Soufriere Hills Volcano, Montserrat in 1998/99 were characterised by extremely high water contents in the eruption cloud due to the interaction with sea water. In the plumes of these eruptions, remote sensing images revealed both high ice contents and unusually low SO_2 concentration (*Rose, 1999*) thus indicating gas scavenging by incorporation into ice particles.

The parameterisation of gas scavenging by ice particles is assumed to be ruled by condensation kinetics in our simulations. Its significance depends then on the sticking probability α of gas molecules to the ice particle's surface, see Sect. (4.2). The knowledge of gas incorporation into ice is in general quite limited. Especially, the applied values for α are based on rather poor observational data. However, our

simulations point out the general importance of the gas trapping in ice particles in an explosive volcanic eruption column.

6.4.5 Résumé: Scavenging of Volcanic Gases in the Plume

The stationary height of the eruption column in our simulation was situated at the tropopause level. Hence, small differences in the plume height have a significant effect on the stratospheric injection of volcanic material. The fractions of volcanic species injected into the stratosphere in relation to the total emission at the crater obtained in the three sensitivity studies are summarized in Tab. (4), for the conditions of the experiments see Tab. (3).

	REFS	DRYS	NOINC
HCl	0.3	1.5	0.6
S-species	15	5	20
inert gas	20	5	20

Table 4: Fraction of volcanic species injected into the stratosphere in [%] of the total emission: results from the sensitivity studies.

The scavenging ratio of volcanic gases in the plume is very sensitive to interactions between hydrometeors and volcanic ash, which strongly influence the efficiency of sedimentation in the plume. The injection of HCl increases in the experiment DRYS in comparison to the experiment REFS due to the reduced removal of HCl-containing graupel from the stratosphere. On the other hand, the injection of sulphur species decreases due to the diminished gas-particle separation leading to less injection of gases into the stratosphere. The increased scavenging of sulphur species by direct incorporation into ice crystals due to enhanced diffusional growth – caused by the changed flow pattern – has no additional effect. Neglecting direct incorporation of volcanic gases into growing ice (NOINC) leads to an increase of the stratospheric injection of sulphur gases. Due to the low water solubility, these gases are only scavenged by frozen hydrometeors. HCl – being highly soluble in liquid water – is almost completely scavenged by liquid water in lower parts of the plume, where condensation of water drops occurs for the first time. Thus, neglecting scavenging by ice increases the stratospheric input by a factor of two, but the overall HCl-injection is rather small anyway.

The eruption of Mt. St. Helens penetrated the tropopause for at least 9 h and injected about 1 Mt SO₂ into the stratosphere (*Holasek and Self, 1995*). We

obtain a stratospheric injection of 5 000 to 20 000 tons per hour for the sum of SO₂ and H₂S expressed as SO₂-mass. Projection of this result on Mt. St. Helens conditions (also taking into account the different eruption rates and sulphur gas fractions) reveals a stratospheric injection which is in the range of the observed input. For HCl the simulated stratospheric injections was 80 to 400 tons per hour, detailed observational data on the direct input of HCl into the stratosphere are not available.

Volcanic sulfate and ash particles contribute about the same amount to the total aerosol mass in the stratosphere resulting from the eruption simulated in this study. However, the content of sulfur gases in the erupting mixture at the crater was by factor of 1000 lower than that of volcanic ash. Precipitation of aggregated particles prevent most of the erupted ash from reaching the stratosphere, whereas the scavenging of sulfur gases is much less efficient. These results are confirmed by observations of the composition of El Chichón ejecta in the stratosphere compared to the composition of the erupted material (*Schneider et al.*, 1999; *Yu and Rose*, 1999).

The conclusions gained in this study are of qualitative relevance, they show the principal significance of hydrometeor-ash-interactions and of direct gas incorporation into growing ice for the scavenging ratio of volcanic gases in the plume. Gases, which have once been injected into the stratosphere, could be scavenged in later phases of the eruption, or the sublimation of contaminated hydrometeors might release chemicals to the gas phase. These processes are not considered in the framework of this research, but they should be taken into account when discussing the climatic impact of explosive volcanic eruptions.

7 Conclusions and Outlook

The scavenging of gases and particles in an explosive volcanic plume has been studied by numerical simulations with the plume model ATHAM. We identified relevant factors that determine the fraction of volcanic material eventually being injected into the stratosphere. An extended version of the microphysics has been formulated: based on a two-moment scheme it describes the interactions of hydrometeors and volcanic ash in the plume, which leads to particle growth and efficient sedimentation. In addition, we developed a module for the calculation of volcanic gas scavenging by liquid and solid hydrometeors in the plume. The simulations have been performed in a two dimensional model version in cylindrical coordinates without cross wind effects, hence, they do not exactly reflect the real atmospheric behaviour during a volcanic eruption. This survey should be understood as a qualitative process study, it does not aim to give quantitative results. However, it provides new information about the evolution of microphysical processes, which influence the scavenging ratio of gases and particles in the plume.

The simulation time in this study was one hour: the eruption lasted 30 min, the post-eruptive evolution of the plume was studied during another 30 min. Our simulations took place in the tropics with the tropopause at 17 km. The plume top penetrated into the stratosphere up to ~ 22 km, but the stationary height was at the tropopause level. Hence, the degree of injection of volcanic material into the stratosphere is highly sensitive to small changes in the plume height.

7.1 Particles and Hydrometeors in the Plume

This study reveals the dominant role of hydrometeors in controlling many processes in the plume. The coating of volcanic ash with liquid water or ice results in highly efficient growth of particles. The initial particle sizes in the micrometer range (2.5 and 50 μm) quickly increase by about one order of magnitude. Coagulation greatly enhances the fallout of ash: millimeter sized hydrometeor-ash aggregates exhibit a much larger fall velocity than the initial fine grained ash. Half an hour after the eruption ended, the ash remains chiefly in the troposphere and 50 % of the total erupted particles are already deposited at the ground. A final fraction of only $4 \cdot 10^{-5}$ of the total ash mass is situated in the stratosphere, in our study. However, having in mind the huge amounts of ash erupted during a volcanic explosion, this is a significant quantity. Precipitation of aggregates results in efficient gas-particle separation: the plume of an inert gas, which is passively transported with the mean flow stays completely at the height of the tropopause. The stratospheric injection of the inert gas is about 20 % of the total gas eruption at the end of our simulation time.

Our simulations revealed that the plume shape is considerably different, when the interaction between particles and hydrometeors is neglected. This sensitivity study corresponded to an eruption taking place in an arid climatic zone with a smaller amount of condensed water available in the plume. Particle growth primarily results in much larger fall velocities and in increased precipitation rates, but it also has a secondary effect on the stream pattern. Falling aggregates induce an eddy structure and lead to a strongly enhanced subsidence of cold, dry air, which in turn influences the microphysics in the plume by lowering the supersaturation in the ascent zone. Without particle growth, fine ash is quasi suspended in the air at the stationary plume height. This results in an increase of the stratospheric ash injection by a factor of 500, however, the injection of gas decreases by 75 % due to the lack of gas-particle separation.

The information about the properties of volcanic ash in the plume is rather limited at the moment. The particle distribution employed in our simulations might not reflect, what had initially been erupted at the vent. However, a sensitivity study with different initial ash particle size distributions in the micrometer range did not show any effect: particle growth is so efficient that small changes of the initial size distribution are negligible. The particles erupted at the vent in this study were rather fine grained. The eruption of Fuego volcano in 1974, for example, exhibited much coarser ash in the millimeter range (*Self et al.*, 1999). Further sensitivity studies with ash of this size will be performed. The parameterisation of the interaction between ash and hydrometeors applied in this study is based on the assumption that volcanic particles are always active as condensation nuclei for liquid water and ice. This is reasonable, since ash particles are often coated with – sometimes hygroscopic – salts, but it has not yet been proven by observations. In addition, the parameters applied for the coagulation efficiency of aggregates might overestimate particle growth and should be improved by observational data, which are not yet available. We did not consider breakup processes of aggregates, and particles are assumed to be solid spheres in our parameterisation so far. These topics will be investigated in more detail in the future, laboratory or field studies of ash properties could greatly improve the parameterisation of particle growth and fall velocities. The results obtained in this study might reflect an upper limit on the sizes and fall velocities of aggregates in an explosive volcanic eruption column.

Our results show that by far the highest portion of condensed water freezes to ice in the eruption column. The fast plume rise to regions, which are too cold for even supercooled liquid water to exist causes most particles to occur as ice-ash aggregates. The total mass of tephra in the model domain is about 100 times that of condensed water during the eruption. Hence, the hydrometeor-ash aggregates are rather dry, with an ash fraction in the aggregates usually higher than 80 wt.%. The small relative humidity in the lower troposphere in our scenario leads to total

evaporation of condensed water or ice and results in the deposition of completely dry aggregates. No traces of ice or water, would be observed in the fallout of the simulated eruption, although it has played a significant role during the transport in the plume. Similar little evidence could be found for the history of ice by remote sensing, because it needs an extremely high ice content to distinguish its signals from that of silicate particles in the plume (*Rose, 1999*).

An injection of water into the stratosphere ($\sim 30\,000$ tons per hour) is indicated by the simulations presented here. A significant increase in stratospheric water concentration might also lead to an increase of OH and HO₂ (*Coffey, 1996*). These highly reactive radicals are key species in stratospheric chemistry. Additional water vapour could reduce the lifetime of SO₂ and H₂S and it could change the composition of the volcanic sulphate aerosol in the stratosphere.

7.2 Scavenging of Volcanic Gases in the Plume

We examined the scavenging of the most important volcanic gases, HCl, SO₂ and H₂S, by liquid and solid hydrometeors and by aggregates in the plume. The scavenging efficiency is determined by the amount of condensed water or ice. Particle growth due to hydrometeor-ash interactions leads to larger aggregates with larger fall velocity eventually removing volcanic volatiles from the atmosphere.

HCl is almost completely removed from the gas phase by dissolution in liquid water occurring in the lower central plume. These ash-containing drops quickly freeze to graupel aggregates in the rising plume, in this way transferring dissolved HCl: the highest fraction of HCl is found in graupel-ash aggregates that precipitate efficiently, thus also removing HCl from higher altitudes. The stratospheric injection of HCl is only about 0.3 % of the total mass erupted by the volcano.

The fate of sulphur gases in the plume is completely different from that of HCl: A large extent of SO₂ and H₂S stays at high levels in the umbrella region. The sulphur species are only slightly soluble in liquid water, hence, they are not removed by cloud and rain drops at lower heights. However, they are scavenged by frozen hydrometeors via direct gas incorporation during diffusional growth of ice: about 30 % of the total mass of SO₂ and H₂S in the plume was removed from the gas phase. At the end of our simulation about 15 % of the total volcanic sulphur is injected into the stratosphere. This causes a reduction by $\sim 25\%$ of the potential input of an inert volcanic gas, indicating the great relevance of gas trapping in ice within a volcanic plume. Observational evidence for the proposed mechanism has been found in the eruption clouds of Rabaul in 1994 and Soufriere Hills Volcano, Montserrat, in 1998/99 that were characterized by extremely high amounts of ice accompanied by unusually low SO₂ concentrations (*Rose, 1999*). The exact amount of the scavenging ratio for the individual species is sensitive

to the sticking probabilities of gas molecules at the ice particle's surface. These are based on a poor data basis, which should be improved. The influence of the sticking probabilities on the scavenging ratio will be the subject of future sensitivity studies.

Neglecting hydrometeor-ash interactions leads to an increased stratospheric injection of HCl. HCl – most of it contained in graupel – is not transported towards the ground, because pure graupel exhibits a greatly decreased fall velocity when compared to grown graupel-ash-aggregates. The stratospheric chlorine injection increases by 500 % due to the lack of sedimentation, but it is still rather small: only 1.5 % of the total volcanic emission. On the other hand, the input of SO₂ and H₂S into the stratosphere decreases. These species are mainly suspended in the air, whether they stay in the gas phase or are incorporated into floating ice particles. The lack of gas-particle separation reduces the input of gases in general, because of the reduction in plume height, thus also reducing the sulphur gas injection into the stratosphere to about 5 % of the total volcanic emission.

At the moment, only one paper has been published dealing with the scavenging of volcanic gases in the plume (*Tabazadeh and Turco, 1993*). The authors revealed a total removal of HCl from the gaseous phase by supercooled liquid droplets. On the other hand, SO₂ was found to be completely injected into the stratosphere. These statements are in general agreement with our results. Their simulations were based on the quite simple one dimensional model of *Woods (1988)*. The model used a crude description of the dynamics, where the mixing of surrounding air into the plume was described by an arbitrary entrainment parameter. This led to much higher temperatures in the eruption column, thus preventing the evolution of ice, which has been found to be the dominant phase in the more complex simulations with ATHAM. In addition, the Woods-model considered only the condensation of water vapour, it did not include a detailed microphysical parameterisation and did not account for particle growth or sedimentation processes in the plume. Hence, the survey of *Tabazadeh and Turco (1993)* provided a principal estimate of volcanic gas injections into the stratosphere, but it was not suitable to examine the parameters, which determine the scavenging efficiency in the plume.

Low relative humidity in the troposphere in our simulations caused precipitation to reevaporate before it could reach the ground. As a consequence, degassing of volcanic volatiles being scavenged in upper parts of the plume occurred at lower heights. Gases were prevented from the injection into the stratosphere, however, they were not deposited at the ground. No evidence of gas scavenging, such as ash particles coated with acid solutions or even acid rain, could be found in the fallout of the eruption simulated here, although it occurred to a significant degree in upper parts of the plume.

The consideration of the salinity effects did not show any significant effect on the amount of liquid water in the plume, because the concentration of dissolved species was too small ($< 1 \text{ mol/kg}_{\text{hydrometeor}}$). This may not be true for an eruption with higher gas emissions, or an eruption occurring in a dry environment with less condensed water, which leads to higher solution concentrations. In addition, we treated the droplets in the volcanic plume as ideal solutions, neglecting the complex interactions of ions with each other and with water molecules. Especially in higher concentrated solutions, these interactions might lead to increased effective concentrations, this way influencing the salinity effect, but also the solubility of gases in liquid drops.

7.3 Future Plans

All simulations in this study were performed under the same volcanological and environmental conditions. Model runs under various atmospheric conditions must still be carried out, e.g. with entrainment of ambient clouds, which would strongly enhance the amount of water in the plume. It would be interesting to run simulations with different volcanic forcing, e.g. a pulsating eruption. The gas emissions of Mt. Pinatubo and El Chichón were characterised by significantly different gas compositions: El Chichón erupted considerable amounts of HCl whereas no HCl was found in the Mt. Pinatubo plume. The initialisation of less volcanic HCl at the vent might show an effect on the scavenging ratio of sulphur gases: decreased acidity of the drops due to smaller HCl concentration increases the solubility of SO_2 and H_2S in liquid droplets. Furthermore, we plan to perform simulations erupting NaCl particles at the crater, since these were found in the stratosphere after the eruption of El Chichón (*Woods et al.*, 1985).

The two-moment scheme for the microphysics in our parameterisation has an intermediate complexity between simple Kessler-type formulations and detailed spectral microphysics; but it has the advantage of being relatively efficient in terms of computing time and memory. This study revealed an enormous supersaturation in the central rising zone of the plume. Some microphysical parameterisations we employed might not be suitable for this situation, especially the nucleation and diffusional growth processes. Validation of our results is not possible for a volcanic cloud, only plausibility studies can be performed. Further sensitivity studies to test the two-moment scheme under regular atmospheric conditions will be carried out in order to compare the simulated microphysics with observations. The modular structure of ATHAM facilitates the connection of alternative modules with higher complexity: we will implement the detailed spectral microphysics of the Hebrew University, Jerusalem (*Khain and Sednev*, 1995, 1996) and compare the results with those of the simpler but much faster two-moment scheme developed in the framework of this survey.

The adsorption of gases on dry volcanic particles was not taken into account so far, since no data on the surface area of ashes and the sticking probabilities of gases at particles are available. However, our simulations indicated that the amount of totally dry ash in the plume is rather irrelevant. Sensitivity studies will be performed in order to estimate the importance of this additional sink for gaseous volcanic substances.

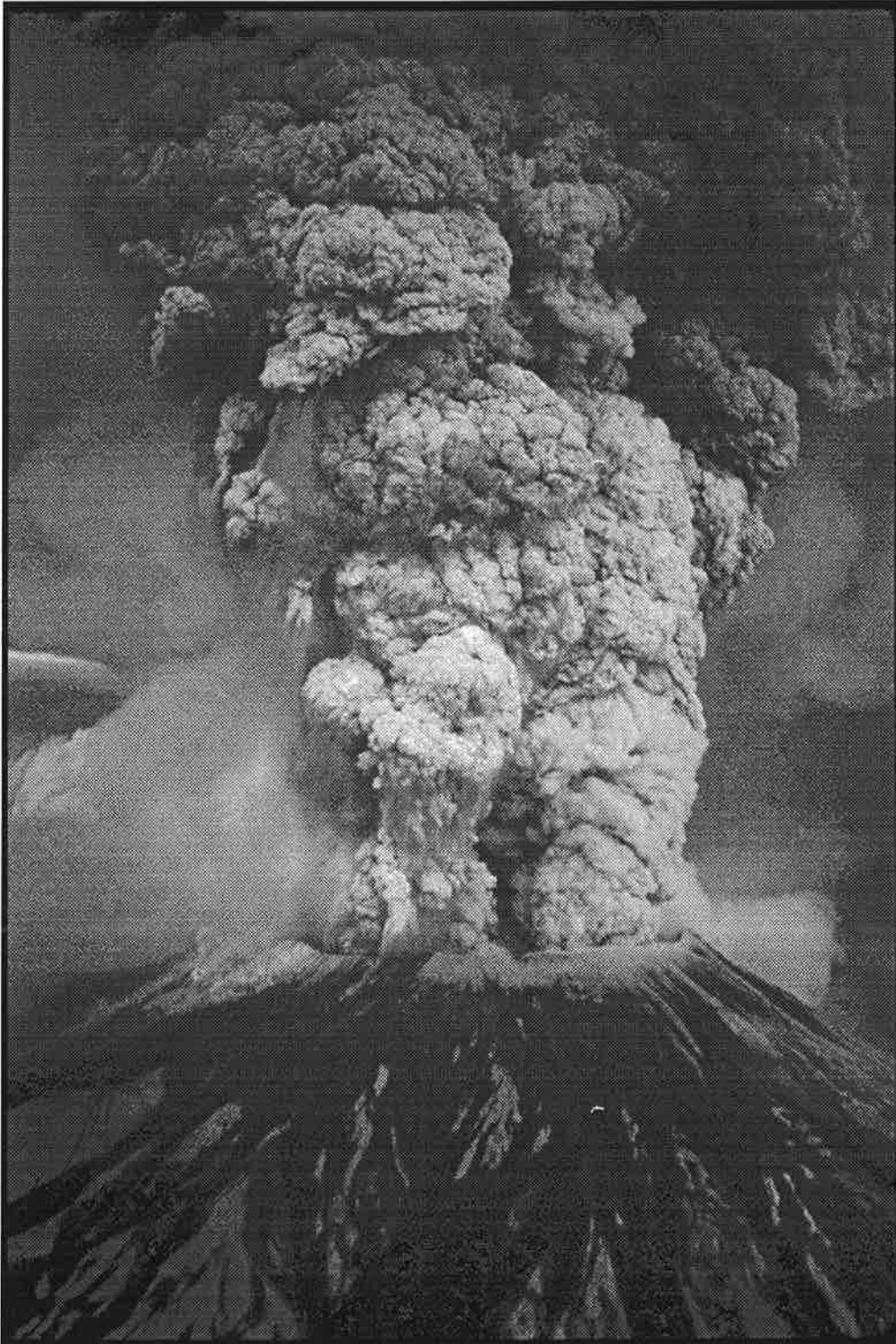
Another topic of interest is the investigation of the chemical processes inside the rising plume. The simultaneous calculation of the dynamic plume development including turbulence, microphysical processes and complete chemistry in ATHAM is far too costly in terms of computing time and memory. Hence, we will perform off-line simulations of the chemistry in the plume along several trajectories determined by the plume model ATHAM. The trajectories starting at different locations in the crater will be calculated after the plume has reached its stationary height. The respective data for temperature, relative humidity and liquid water content along the trajectory will be taken from ATHAM simulations. In this way, we will derive more detailed information about the chemical alterations, which a certain air parcel erupted by the volcano experiences during its rise from the lithosphere to the stratosphere.

More realistic representations of an explosive volcanic event must certainly be performed in a three dimensional model. A parallel version of ATHAM is being developed in cooperation with the University of Michigan (*Herzog, 1999*); it will significantly decrease the time needed for such model runs. ATHAM will be employed in the three dimensional version to simulate the 1992 eruption of Crater Peak at Mt. Spurr volcano in Alaska. In addition, ATHAM is being reclassified to simulate wild fires. The modules developed in the framework of this study will be employed for the examination of processes in biomass burning plumes. A module representing the chemical processes occurring in a biomass burning plume near to the source is being developed at the Max-Planck-Institut for Chemistry in Mainz (*Trentmann, 1999*) that will be connected to ATHAM. The interaction of chemistry and microphysics will be included. Furthermore, ATHAM will be applied for the simulation of convective clouds to examine the effect of (anthropogenic) aerosols on microphysical processes that determine the precipitation efficiency.

This work contributes to the general understanding of processes occurring in explosive volcanic eruption clouds. The modules which have been accomplished in the framework of this study allow for the examination of the scavenging gases and particles under different conditions. ATHAM is an excellent tool to describe the processes in high energy plumes and will be used for a wide range of applications in the future.

Plume of Mt. St. Helens, May 18, 1980 Eruption

Photo taken by Austin Pott





8 Appendix

Sources and Sinks of Tracers due to Microphysical Processes

The tendencies of hydrometeor and ash mass content and the tendencies of number concentrations are summarized.

$$\frac{\partial}{\partial t} q_v = -CEC - CER - SDH - SDI - CEMH - NC - NI \quad (92)$$

$$\begin{aligned} \frac{\partial}{\partial t} q_c &= NCq + CEC \\ &+ f_i MIq - f_c (FRCq + AUCq + ACRCq + ACHCq) \end{aligned} \quad (93)$$

$$\frac{\partial}{\partial t} q_{ac} = f_{ai} MIq - f_{ac} (FRCq + AUCq + ACRCq + ACHCq) \quad (94)$$

$$\frac{\partial}{\partial t} N_{pc} = NCn + Min - FRCn - AUCnc - ACRCn - ACHCn \quad (95)$$

$$\begin{aligned} \frac{\partial}{\partial t} q_r &= CER + Max(0., CEMH) \\ &+ f_i (ACRIq(T < T_0)) \\ &+ f_h XMHq + f_c (AUCq + ACRCq + ACHC(T > T_0)) \\ &- f_r (ACIRq + ACHRq(T < T_0) - FRRq) \end{aligned} \quad (96)$$

$$\begin{aligned} \frac{\partial}{\partial t} q_{ar} &= f_{ai} (ACRIq(T < T_0)) \\ &+ f_{ah} XMHq + f_{ac} (AUCq + ACRCq + ACHC(T > T_0)) \\ &- f_{ar} (ACIRq + ACHRq(T < T_0) + FRRq) \end{aligned} \quad (97)$$

$$\begin{aligned} \frac{\partial}{\partial t} N_{pr} &= XMHn + AUCnr + ACHC(T > T_0) \\ &- ACIRn - ACHRn(T < T_0) - FRRn \end{aligned} \quad (98)$$

$$\begin{aligned} \frac{\partial}{\partial t} q_i &= NIq + SDI \\ &+ f_c FRCq - f_i (MIq + AUIq + ACRIq + ACHIq) \end{aligned} \quad (99)$$

$$\frac{\partial}{\partial t} q_{ai} = f_{ac} FRCq - f_{ai} (MIq + AUIq + ACRIq + ACHIq) \quad (100)$$

$$\frac{\partial}{\partial t} N_{pi} = NIn + FRCn - MIn - AUI n - ACRI n - ACHI n \quad (101)$$

$$\begin{aligned} \frac{\partial}{\partial t} q_h &= SDH + MIN(0., CEMH) \quad (102) \\ &+ f_c ACHCq(T < T_0) + f_r (FRRq + ACIRq + ACHRq(T < T_0)) \\ &+ f_i AUIq + ACRIq + ACHIq \\ &- f_h MHq \end{aligned}$$

$$\begin{aligned} \frac{\partial}{\partial t} q_{ah} &= f_{ac} ACHCq(T < T_0) \quad (103) \\ &+ f_{ar} (FRRq + ACIRq + ACHRq(T < T_0)) \\ &+ f_{ai} (AUIq + ACRIq + ACHIq) - f_{ah} (MHq) \end{aligned}$$

$$\frac{\partial}{\partial t} N_{ph} = FRRn + AUI n + ACRI n - MHn \quad (104)$$

References

- Ahn, M.-H., New SO₂ retrieval algorithm and its application to the El Chichón and Mt. Pinatubo volcanic eruption cloud, <http://metosrv2.umd.edu/mhahn/SO2ALG/newalg.html>, 1997.
- Armienti, P., A numerical model for simulation of tephra transport and deposition: applications to May 18, 1980, Mount St. Helens eruption, *Journal of Geophysical Research*, *93*(B6), 64638–6476, 1988.
- Barklie, R. H. D., Nucleation measurements on rain and melted hail, Sci. Rep. MW-30, Stormy Weather Research Group, McGill University, 1959.
- Barrie, L. A., An improved model of reversible SO₂ washout by rain, *Atmospheric Environment*, *12*, 407–412, 1978.
- Beheng, K. D., and G. Doms, A general formulation of collection rates of cloud and raindrops using the kinetic equation and comparison with parameterizations, *Beiträge zur Physik der Atmosphäre*, *59*(1), 66–84, 1990.
- Berry, E. X., and R. L. Reinhardt, An analysis of cloud drop growth by collection: Part IV: A new parameterization, *Journal of the Atmospheric Sciences*, *31*, 2127–2135, 1974.
- Bigg, E. K., The supercooling of water, *Proc. Phys. Soc. London*, *B66*, 688–694, 1953.
- Bluth, G. J. S., S. D. Doiron, C. C. Schnetzler, A. J. Krueger, and L. S. Walter, Global tracking of the SO₂ cloud from the June, 1991 Mount Pinatubo eruptions, *Geophysical Research Letters*, *19*(2), 151–154, 1992.
- Burnett, C. R., and E. B. Burnett, Observational results on the vertical column abundance of atmospheric hydroxyl: Description of its seasonal behavior 1977-1982 and of the 1982 El Chichon perturbation, *Journal of Geophysical Research*, *89*, 9603–9611, 1984.
- Byers, H. R., *Elements of cloud physics*, The University of Chicago Press, 1965.
- Carey, S., and H. Sigurdsson, Influence from particle aggregation on deposition of distal tephra from the May 18, 1980, eruption of Mount St. Helens volcano, *Journal of Geophysical Research*, *87*(B8), 7061–7072, 1982.
- Carey, S., and R. S. J. Sparks, Quantitative models of the fallout and dispersal of tephra from volcanic eruption columns, *Bulletin of Volcanology*, *48*, 109–125, 1986.

References

- Carslaw, K. S., T. Peter, and S. L. Clegg, Modeling the composition of liquid stratospheric aerosols, *Review of Geophysics*, 35(2), 125–154, 1997.
- Chen, J.-P., and P. J. . Crutzen, Solute effect on the evaporation of ice particles, *Journal of Geophysical Research*, 99(D9), 18847–18859, 1994.
- Chuan, R. L., Dispersal of volcano-derived particles from Mt. Erebus in the Antarctic atmosphere, Antarctic Research Series, 1994.
- Coffey, M. T., Observations of the impact of volcanic activity on stratospheric chemistry, *Journal of Geophysical Research*, 101, 6767–6780, 1996.
- Conklin, M. H., R. A. Sommerfeld, S. K. Layrd, and J. E. Vilinski, Sulfur dioxide reaction on ice surfaces: implications for dry deposition to snow, *Atmospheric Environment*, 27(A), 159–166, 1993.
- Delmas, R. J., Antarctic precipitation chemistry, in *Chemistry of Multiphase Atmospheric Systems*, edited by W. Jaeschke, vol. G6 of *NATO Adv. Study Inst. Ser.*, pp. 249–266, Springer-Verlag, New York, 1986.
- DeMore, W. B., S. P. Sander, D. M. Golden, R. F. Hampson, M. J. Kurylo, D. J. Howard, A. R. Ravishankara, C. E. Kolb, and M. J. Molina, *Chemical Kinetics and Photochemical Data for Use in Stratospheric Modeling*, no. 12 in JPL Publication 92-20, Jet Propulsion Laboratory, Pasadena, California, 1997.
- Diehl, K., Eine theoretische und experimentelle Untersuchung über die Zirkulation in Wolkentropfen und Regentropfen, Master's thesis, University of Mainz, Germany, 1989.
- Diehl, K., Eine experimentelle Untersuchung zur Aufnahme von Schadstoffgasen durch Schneekristalle, Ph.D. thesis, University of Mainz, 1995.
- Diehl, K., S. K. Mitra, and H. R. Pruppacher, A laboratory study on the uptake of HNO₃ and HCl vapor by snow crystals and ice spheres at temperatures between 0 and - 40 ° C, *Atmospheric Environment*, 29(9), 975–981, 1995.
- Diehl, K., S. K. Mitra, and H. R. Pruppacher, A laboratory study on the uptake of HCl, HNO₃ and SO₂ gas by ice crystals and the effect of these gases on the evaporaton rate of the crystals, *Atmospheric Environment*, 47-48, 235–244, 1998.
- Dobran, F., and A. Neri, Numerical simulation of collapsing volcanic columns, *Journal of Geophysical Research*, 98, 4231–4259, 1993.
- Dominé, F., and E. Thibert, Mechanisms of incorporation of trace gases in ice grown from the gas phase, *Geophysical Research Letters*, 101(24), 3627–3630, 1996.

- Dominé, F., and E. Thibert, Thermodynamic and kinetics of the solid solutions of HCl in ice, *Journal of Physical Chemistry*, 101(18), 3552–3565, 1997.
- Dominé, F., E. Thibert, E. Silvente, M. Legrand, and J. Jaffrezo, Determining past atmospheric HCl mixing ratios from ice core analysis, *Journal of Atmospheric Chemistry*, 21, 1653–186, 1995.
- Faraday, M., On regulation, and on observation of force, *Philos. Mag.*, 17, 1859.
- Fichtenholz, G. M., *Differential- und Integralrechnung II*, VEB Deutscher Verlag der Wissenschaften, 1964.
- Fisher, R. V., Volcanic topics, <http://magic.geol.ucsb.edu/fisher/>, 1999.
- Flatau, P. J., G. J. Tripoli, V. F., and W. R. Cotton, The CSU-RAMS cloud microphysical module: General theory and code documentation, *Atm. Sci. Pap.*, 451, 88 pp, 1989.
- Fletcher, N. H., *The Physics of Rainclouds*, Cambridge University Press, 1962.
- Gerlach, T. M., and T. Casadevall, Fumarole emissions at Mount St. Helens Volcano, June 1980 to October 1981: Degassing of a magma-hydrothermal system, *Journal of Volcanology and Geothermal Research*, 28, 141–160, 1986.
- Glaze, L. S., and S. M. Baloga, Sensitivity of buoyant plume heights to ambient atmospheric conditions: Implications for volcanic eruption columns, *Journal of Geophysical Research*, 101(D1), 1529–1540, 1996.
- Glaze, L. S., S. M. Baloga, and L. Wilson, Transport of atmospheric water vapor by volcanic eruption columns, *Journal of Geophysical Research*, 102(D5), 6099–6108, 1997.
- Gmelin, L., and E. Pietsch, *Gmelins Handbuch der anorganischen Chemie, F CL BR I*, Verlag Chemie, Leipzig, 8th edn., 1926.
- Graf, H.-F., M. Herzog, J. M. Oberhuber, and C. Textor, The effect of environmental conditions on volcanic plume rise, *accepted at Journal of Geophysical Research*, 1999.
- Gravenhorst, G., T. Janssen-Schmidt, D. H. Erhalt, and E. P. Röth, the influence of clouds and rain on the vertical distribution of sulfur dioxide in a one-dimensional steady state model, *Atmospheric Environment*, 12, 691–698, 1978.
- Gunn, R., and G. D. Kinzer, The terminal velocity of fall for water drops in stagnant air, *Journal of Meteorology*, 6, 243–248, 1949.

References

- Hannemann, A., S. K. Mitra, and H. R. Pruppacher, On the scavenging of gaseous nitrogen compounds by large and small raindrops I. A wind tunnel and theoretical study of the uptake and the desorption of NH_3 in the presence of CO_2 , *Journal of Atmospheric Chemistry*, *21*, 293–307, 1995.
- Harrington, J. Y., M. P. Meyers, R. L. Walko, and W. R. Cotton, Parameterization of ice crystal conversion processes in cirrus clouds using double-moment basis functions. Part I: Basic formulation and one-dimensional tests, *Journal of the Atmospheric Sciences*, *52*, 4344–4366, 1995.
- Harris, D. M., and W. I. Rose, Estimating particle size, concentrations, and total mass of ash in volcanic columns using weather radar, *Journal of Geophysical Research*, *88*(C15), 1983.
- Harris, D. M., J. W. I. Rose, R. Roe, and M. R. Thompson, Radar observations of ash eruptions at Mount St. Helens volcano, Washington, *U.S. Geol. Surv. Prof. Pap.*, *1250*, 1981.
- Herzog, M., Simulation der Dynamik eines Multikomponentensystems am Beispiel vulkanischer Eruptionswolken, Ph.D. thesis, University of Hamburg, 1998.
- Herzog, M., 1999, personal communication.
- Herzog, M., H.-F. Graf, C. Textor, and J. M. Oberhuber, The effect of phase changes of water on the development of volcanic plumes, *Journal of Volcanology and Geothermal Research*, *87*, 55–74, 1999.
- Hobbs, P. V., J. P. Tuell, D. A. Hegg, L. F. Radke, and M. W. Eltgroth, Particles and gases from the 1980-1981 volcanic eruptions of Mount St. Helens, *Journal of Geophysical Research*, *87*, 11062–11086, 1982.
- Hofmann, D. J., and S. Solomon, Ozone destruction through heterogeneous chemistry following the eruption of El Chichón, *Journal of Geophysical Research*, *94*, 5029–5041, 1989.
- Holasek, R. E., and S. Self, GOES weather satellite observations and measurements of the May 18, 1980, Mount St. Helens eruption, *Journal of Geophysical Research*, *100*, 8469–8487, 1995.
- Holdsworth, G., H. R. Krouse, and E. Peake, Relationship between volcanic emission peaks and the oxygen isotope signature in an ice core from the Yukon territory, Canada (abstract), *Eos. Trans. AGU*, *67*, 883, 1986.
- Hudson, R., 1996, personal communication.

- Iribarne, J. V., and T. Pyshnov, The effect of freezing on the compositions of supercooled droplets - I. retention of HCl, NH₃ and H₂O₂, *Atmospheric Environment*, 24A(2), 383–387, 1990.
- Iribarne, J. V., T. Pyshnov, and B. Naik, The effect of freezing on the compositions of supercooled droplets - II. Retention of S(IV), *Atmospheric Environment*, 24A(2), 389–398, 1990.
- Kessler, E., On the distribution and continuity of water substance in atmospheric circulation, *Met. Monographs*, 10, 84, 1969.
- Khain, A. P., personal communication, 1999.
- Khain, A. P., and I. Sednev, Simulation of hydrometeor size spectra evolution by water-water, ice-water and ice-ice interactions, *Atmospheric Research*, 1995.
- Khain, A. P., and I. Sednev, Simulation of precipitation formation in the eastern mediteranean coastal zone using a spectral microphysics cloud ensemble model, *Atmospheric Research*, 43, 77–110, 1996.
- Kim, Y. P., and J. H. Seinfeld, Atmospheric gas-aerosol equilibrium. I.: thermodynamic model, atmospheric gas-aerosol equilibrium. II.: analysis of common approximations and activity calculation methods, *Aerosol Science and Technology*, 19, 157–198, 1993.
- Kotra, J. D., W. Zoller, M. Hart, and J. Moyers, El Chichón composition of plume gases and particles, *Science*, 222, 1018–1021, 1993.
- Kronig, R., and J. C. Brink, On the theory of extraction from falling drops, *J. Appl. Sci. Res.*, A2, 142–154, 1950.
- Krueger, A. J., L. S. Walter, P. K. Bhartia, C. C. Schnetzler, N. A. Krotkov, I. Sprod, and G. J. S. Bluth, Volcanic sulfur dioxide measurements from the total ozone mapping spectrometer instruments, *Journal of Geophysical Research*, 100, 14057–14076, 1995.
- Laube, M., and H. Höller, Meteorology: Physical and chemical properties of the air: Cloud physics, in *Landolt-Börnstein*, edited by G. Fischer, vol. 4b, chap. 5, Springer-Verlag, 1987.
- LeClair, B. P., A. E. Hamielec, H. R. Pruppacher, and W. D. Hall, A theoretical and experimental study of the internal circulation in water drops falling at terminal velocity in air, *Journal of the Atmospheric Sciences*, 29, 728–740, 1972.
- Levine, I. N., *Physical Chemistry*, Mc Graw-Hill, Inc., 4th edn., 1995.

References

- Lin, Y., R. D. Farley, and H. D. Orville, Bulk parametrization of the snow field in a cloud model, *Journal of Climate and Applied Meteorology*, *22*, 1065–1092, 1983.
- Luhr, J. F., I. S. E. Carmichael, and J. C. Varekamp, The 1982 eruptions of El Chichón volcano, Chiapas, Mexico: Mineralogy and petrology of the anhydrite-bearing pumices, *Journal of Volcanology and Geothermal Research*, *23*, 69–108, 1984.
- Lüpkes, C., *Untersuchungen zur Parametrisierung von Koagulationsprozessen von niederschlagsbildenden Tropfen*, Verlag Dr. Kovac, Hamburg, 1991.
- Mackinnon, I. D. R., J. L. Gooding, D. S. McKay, and U. S. Clanton, The El Chichón stratospheric cloud: solid particulates and settling rates, *Journal of Volcanology and Geothermal Research*, 1984.
- Mankin, W. G., and M. T. Coffey, Increased stratospheric hydrogen chloride in the El Chichón cloud, *Science*, *226*, 170–172, 1984.
- Mankin, W. G., M. T. Coffey, and A. Goldman, Airborne observations of SO₂, HCl, and O₃ in the stratospheric plume of the Pinatubo Volcano in July 1991, *Geophysical Research Letters*, *19*(2), 179–182, 1992.
- Marshall, J. S., and W. K. Palmer, The distribution of rain drop size, *Journal of Meteorology*, *5*, 165–166, 1948.
- Mason, B. J., On the melting of hailstones, *Quarterly Journal of the Royal Meteorological Society*, *82*, 209–216, 1956.
- McCormick, M. P., L. W. Thomason, and C. R. Trepte, Atmospheric effects of the Mt. Pinatubo eruption, *Nature*, *373*(2), 399–404, 1995.
- McKeen, S. A., S. C. Liu, and C. S. Kiang, On the chemistry of stratospheric SO₂ from volcanic eruptions, *Journal of Geophysical Research*, *89*(D3), 4873–4881, 1984.
- Meyers, M. P., P. J. DeMott, and W. R. Cotton, New primary ice nucleation in an explicit cloud model, *Journal of Applied Meteorology*, *31*, 708–721, 1992.
- Meyers, M. P., R. L. Walko, J. Y. Harrington, and W. R. Cotton, New RAMS cloud microphysics parameterization. Part II: The two moment scheme, *Atmospheric Research*, *45*, 3–39, 1997.
- Michelangeli, D. V., M. Allen, and Y. L. Yung, El Chichón volcanic aerosol: impact of radiative, thermal and chemical perturbations, *Journal of Geophysical Research*, *94*(D15), 18429–18443, 1989.

- Mitra, S. K., A. Waltrip, A. Flossman, and H. R. Pruppacher, A windtunnel and theoretical investigation to test various theories for the absorption of SO₂ by drops of pure water and water drops containing H₂O₂ and (NH₄)₂SO₄, in *Precipitation scavenging and atmospheric-surface exchange*, edited by S. E. Schwartz, and W. G. N. Slinn, vol. I of *The Georgii Volume: Precipitation scavenging processes*, pp. 123–141, Hemispheric Publishing Corporation, 1992.
- Müller, D., Untersuchung des Einflusses der nassen Deposition auf Vulkansedimente, Master's thesis, University of Hamburg, 1997.
- Murcray, D. G., F. J. Murcray, D. B. Barker, and H. J. Mastenbrook, Changes in the stratospheric water vapour associated with the eruption of Mount St. Helens, *Science*, *211*, 823–824, 1981.
- Neri, A., and G. Macedonio, Numerical simulation of collapsing volcanic columns with particles of two sizes, *Journal of Geophysical Research*, *101*, 8153–8174, 1996.
- Oberhuber, J. M., personal communication, 1996.
- Oberhuber, J. M., M. Herzog, H.-F. Graf, and K. Schwanke, Volcanic plume simulation on large scales, *J. Volcanol. Geotherm. Res.*, *87*, 29–53, 1999.
- Óskarsson, N., The interaction between volcanic gases and solid tephra - notes on fluorine adhering to tephra of the 1970 Hekla eruption, Rep. 7804, 39 pp., Nordic Volc. Inst. Univ. of Iceland, Reykjavík, 1978.
- Petrenko, V. F., The surface of ice, Special Report 94-22, USA Cold Regions Research and Engineering Laboratory, 1994.
- Pinto, J. P., R. P. Turco, and O. B. Toon, Self-limiting physical and chemical effects in volcanic eruption clouds, *Journal of Geophysical Research*, *94*, 11165–11174, 1989.
- Press, W. H., S. A. Teukolsky, W. T. Vetterling, and B. P. Flannery, *Numerical Recipes in FORTRAN, The Art of Scientific Computing*, Cambridge University Press, 2nd edn., 1992.
- Pruppacher, H. R., and K. V. Beard, A theoretical and experimental study of the internal circulation in water drops falling at terminal velocity in air, *Quarterly Journal of the Royal Meteorological Society*, *96*, 247–256, 1970.
- Pruppacher, H. R., and J. D. Klett, *Microphysics of Clouds and Precipitation*, Kluwer Academic Publishers, 2nd edn., 1997.

- Rasmussen, R. M., and A. J. Heymsfield, Melting and shedding of graupel and hail. Part III: investigation of the role of shed drops as hail embryos in the 1 August CCOPE severe storm, *Journal of the Atmospheric Sciences*, 44(19), 2783–2803, 1987.
- Rasmussen, R. M., V. Levizzani, and H. R. Pruppacher, A wind tunnel and theoretical study on the melting behaviour of atmospheric ice particles: experiment and theory for spherical ice particles of radius $< 500 \mu\text{m}$, *Journal of the Atmospheric Sciences*, 41(3), 381–388, 1984.
- Rogers, R. R., and M. K. Yau, *A Short Course on Cloud Physics*, Pergamon Press, Oxford, 3rd edn., 1989.
- Rose, W. I., personal communication, 1999.
- Rose, W. I., R. L. Chuan, and D. C. Woods, Small particles in the plumes of Mount St. Helens, *Journal of Geophysical Research*, 87(C7), 4956–4962, 1982.
- Rose, W. I., D. Delene, D. Schneider, G. Bluth, A. Krueger, I. Sprod, C. McKee, H. Davies, and G. Ernst, Ice in the 1994 Rabaul eruption cloud: implications for volcano hazard and atmospheric effects, *Nature*, 375, 477–479, 1995.
- Rutledge, S., and P. Hobbs, The mesoscale and microscale structure and organization of clouds and precipitation in midlatitude cyclones. VIII: a model for the 'seeder-feeder' process in warm-frontal rainbands, *Journal of the Atmospheric Sciences*, 40, 1185–1206, 1983.
- Rye, R. O., J. F. Luhr, and M. D. Wasserman, Sulfur and oxygen isotopic systematic of the 1982 eruptions of El Chichón volcano, Mexico, *Journal of Volcanology and Geothermal Research*, 23, 109–122, 1984.
- Sander, R., Modellierung von chemischen Vorgängen an und in Wolken, Ph.D. thesis, Johannes Gutenberg-Universität, Mainz, 1994.
- Santachiara, G., F. Prodi, R. Udisti, and A. Prodi, Scavenging of SO_2 and NH_3 during growth of ice, *Atmospheric Research*, 47–48(9), 209–217, 1998.
- Schmincke, H.-U., Transfer von festen, flüssigen und gasförmigen Stoffen aus Vulkanen in die Atmosphäre, *UWSF-Z. Umweltchem. Ökotox.*, 5, 27–44, 1993.
- Schneider, D. J., and W. I. Rose, Observations of the 1989-90 Redoubt Volcano eruption clouds using AVHRR satellite imagery, vol. 2047, U. S. Geol. Surv. Bull., 1993.
- Schneider, D. J., W. I. Rose, L. R. Coke, and G. J. S. Bluth, Early evolution of a stratospheric volcanic eruption cloud as observed with TOMS and AVHRR, *Journal of Geophysical Research*, 104(D4), 4037–4050, 1999.

- Schumacher, R., A reappraisal of Mount St. Helens ash clusters - depositional model from experimental observation, *Journal of Volcanology and Geothermal Research*, 59, 253–260, 1994.
- Schwartz, S. E., Mass-transport consideration pertinent to aqueous phase reactions of gases in liquid water clouds, in *Chemistry of Multiphase Atmospheric Systems*, edited by W. Jaeschke, vol. G6 of *NATO Adv. Study Inst. Ser.*, pp. 415–471, Springer-Verlag, New York, 1986.
- Self, S., W. I. Rose, P. J. Murrow, and G. G. J. Ernst, Pyroclastic fall deposit from the October 14, 1974, eruption of Fuego, Guatemala, *submitted at Bulletin of Volcanology*, 1999.
- Seyfried, R., 1999, personal communication.
- Simkin, T., Terrestrial volcanism in space and time, *Annu. Rev. Earth Planet Sci.*, 21, 427–452, 1993.
- Smith, B. D., R. A. Zielinski, W. I. Rose, and B. J. Huebert, Water-soluble material on aerosols collected within volcanic eruption clouds, *Journal of Geophysical Research*, 87(C7), 4963–4972, 1982.
- Solomon, S., R. W. Sanders, R. R. Garcia, and J. G. Keys, Increased stratospheric chlorine dioxide over Antarctica caused by volcanic aerosols from Mount Pinatubo, *Nature*, 336, 245–248, 1993.
- Sorem, R. K., Volcanic ash clusters: Tephra rafts and scavengers, *Journal of Volcanology and Geothermal Research*, 13, 63–71, 1982.
- Sparks, R. S. J., M. I. Bursik, S. N. Carey, J. S. Gilbert, L. Glaze, H. Sigurdsson, and A. W. Woods, *Volcanic Plumes*, Wiley and Sons, New York, 1997.
- Symonds, R. B., W. I. Rose, and M. H. Reed, Contribution of Cl- and F-bearing gases to the atmosphere by volcanoes, *Nature*, 334, 415–418, 1988.
- Symonds, R. B., W. I. Rose, G. J. S. Bluth, and T. M. Gerlach, Volcanic gas studies: methods, results and applications, in *Volatiles in Magma*, edited by M. R. Carroll, and J. R. Holloway, vol. 30 of *Reviews in Mineralogy*, pp. 1–66, Mineral Society of America, 1994.
- Tabazadeh, A., and R. P. Turco, Stratospheric chlorine injection by volcanic eruptions: HCl scavenging and implications for ozone, *Science*, 260, 1082–1086, 1993.
- Thibert, E., and F. Dominé, Thermodynamics and kinetics of the solid solution of HCl in ice, *Journal of Physical Chemistry*, 101, 3554–3565, 1997.

References

- Toohey, D. W., L. M. Avallone, L. R. Lait, P. A. Neuman, M. R. Schoeberl, D. W. Fahey, E. L. Woodbridge, and J. G. Anderson, The seasonal evolution of reactive chlorine in the northern hemisphere stratosphere, *Science*, *261*, 1134–1136, 1993.
- Trentmann, J., personal communication, 1999.
- Twomey, S., and Wojciechowski, *J. de Rech. Atmos.*, *4*, 179, 1969.
- Valdez, M. P., and G. A. Dawson, Sulfur dioxide incorporation into ice depositing from the vapor, *Journal of Geophysical Research*, *94*(D1), 1095–1103, 1989.
- Valentine, G. A., and K. H. Wohletz, Numerical models of plinian columns and pyroclastic flows, *Journal of Geophysical Research*, *94*, 1867–1887, 1989.
- Varekamp, J. C., J. F. Luhr, and J. L. Prestegard, The 1982 eruptions of El Chichón Volcano (Ciapas Mexico): character of the ash-fall deposits and gas-phase, *Journal of Volcanology and Geothermal Research*, *23*, 39–68, 1984.
- Varekamp, J. C., E. Thomas, M. Germani, and P. R. Buseck, Particle geochemistry of volcanic plumes of Etna and Mount St. Helens, *Journal of Geophysical Research*, *91*(B12), 12233–12248, 1986.
- Verlinde, F., F. P. J., and C. W. R., Analytical solutions to the collection growth equation: Comparison with approximate methods and application to cloud microphysics parameterization schemes, *Journal of the Atmospheric Sciences*, *47*, 2871–2880, 1990.
- Walcek, C. J., H. R. Pruppacher, J. H. Topalian, and S. K. Mitra, On the scavenging of SO₂ by cloud and rain drops, II: An experimental study of SO₂ absorption and desorption for water drops in air, *Journal of Atmospheric Chemistry*, *1*, 291–306, 1984.
- Walker, G. P. L., L. Wilson, and E. L. G. Bowell, Explosive volcanic eruptions - I. The rate of fall of pyroclasts, *Geophys. J. R. astr. Soc.*, *22*, 377–383, 1971.
- Walko, R. L., W. R. Cotton, M. P. Meyers, and J. Y. Harrington, New RAMS cloud microphysics parameterization. Part I: The single moment scheme, *Atmospheric Research*, *38*, 29–62, 1995.
- Wallace, L., and W. Livingston, The effect of Pinatubo cloud on hydrogen chloride and hydrogen fluoride, *Geophysical Research Letters*, *19*(12), 1209, 1992.
- Waters, J. W., L. Froidvaux, W. G. Read, G. L. Manney, L. S. Elson, D. A. Flower, R. F. Jarnot, and R. S. Harwood, Stratospheric ClO and ozone from the Microwave Limb Sounder on the Upper Atmosphere Research Satellite, *Nature*, *362*, 597–602, 1993.

- Wedler, G., *Lehrbuch der physikalischen Chemie*, VCH Verlagsgesellschaft, Weinheim, Germany, 3rd edn., 1987.
- Wen, S., and W. I. Rose, Retrieval of sizes and total masses of particles in volcanic clouds using AVHRR bands 4 and 5, *Journal of Geophysical Research*, *99*(D3), 5421–5431, 1994.
- Westrich, H. R., and T. M. Gerlach, Magmatic gas source for the stratospheric SO₂ cloud from the June 15, 1991, Pinatubo, *Geology*, *20*, 867–870, 1992.
- Wiesner, M. G., Y. Wang, and L. Zheng, Fallout of volcanic ash to the deep South China Sea induced by the 1991 eruption of Mount Pinatubo (Philippines), *Geology*, *23*(10), 885–888, 1995.
- Willis, P., Functional fits to some observed drop size distributions and parameterization of rain, *Journal of the Atmospheric Sciences*, *41*(9), 1648–1661, 1984.
- Wilson, L., Explosive volcanic eruptions - III. Plinian eruption columns, *Geophys. J. R. astr. Soc.*, *45*, 543–556, 1976.
- Wilson, L., and T. C. Huang, The influence of shape on the atmospheric settling velocity of volcanic ash particles, *Earth and Planetary Science Letters*, *44*, 311–324, 1979.
- Wisner, C., H. D. Orville, and C. Myres, A numerical model of a hail-bearing cloud, *Journal of the Atmospheric Sciences*, *29*, 1160–1181, 1972.
- Wohletz, K. H., T. R. Getchin, M. T. Sanford, and E. M. Jones, Hydrodynamic aspects of caldera-forming eruptions: numerical models, *Journal of Geophysical Research*, *89*, 8269–8285, 1984.
- Woods, A. W., The fluid dynamics and thermodynamics of eruption columns, *Bulletin of Volcanology*, *50*, 169–193, 1988.
- Woods, A. W., Moist convection and the injection of volcanic ash into the atmosphere, *Journal of Geophysical Research*, *98*, 17627–17636, 1993.
- Woods, A. W., The dynamics of explosive volcanic eruptions, *Review of Geophysics*, *33*, 495–530, 1995.
- Woods, D. C., R. L. Chuan, and W. I. Rose, Halite particles injected into the stratosphere by the 1982 El Chichón eruption, *Science*, *230*, 170–172, 1985.
- Yu, T., and W. I. Rose, Retrieval of sulfate and silicate ash masses in young (1 to 4 days old) eruptions clouds using multiband infrared HIRS/2 Data, <http://www.geo.mtu.edu/tyu/old/lpaper/paper.html>, 1999.

Acknowledgements - Danksagung

Hans-F. Graf möchte ich für die interessante Aufgabenstellung danken. Sein Enthusiasmus und seine vielfältige Unterstützung waren sehr motivierend und haben zur Freude bei der Arbeit beigetragen.

Hartmut Graßl danke ich für sein Interesse und die Bereitschaft, diese Arbeit zu begutachten.

Allen, die an der Entwicklung von ATHAM mitgewirkt haben, gilt mein Dank: Hans-F. Graf, Michael Herzog, Dörthe Müller, Josef Oberhuber und Karsten Schwanke.

Michael Herzog möchte ich danken für seine Gesprächsbereitschaft. Die vielen Diskussionen und hilfreichen Kommentare haben sehr zum Gelingen dieser Arbeit beigetragen.

Meinen Kolleginnen und Kollegen vom Schlump danke ich für all die vielen Tips, wenn der Teufel im Rechner oder anderswo steckte. Ganz besonders danke ich Judith Perlwitz und Bärbel Langmann für ihre Hilfe, wenn's mal ganz arg kam.

Josef M. Oberhuber danke ich für seine Ideen bei der numerischen Verwirklichung der Scavenging Prozesse in ATHAM.

Daniel Taurat danke ich für seine Hilfe bei den ersten Kontakten mit der Welt des Fortrans.

I thank Alexander Khain for the intense discussions about cloud microphysics, which extremely improved my understanding of this topic.

I wish to thank Bill Rose for his comprehensive and very encouraging remarks on this thesis.

I thank Colleen Riley for her comments on the manuscript; Mario Antonelli has greatly helped to improve the grammar and spelling. Bruce Denby taught me some really important English words.

Vielen Dank fürs Lesen des Manuskriptes und die kritischen Kommentare an Bärbel Langmann, Sabine Wurzler, Ralf Seyfried und Karoline Diehl.

Sebastian Jung danke ich für seine Unterstützung während all der Zeit, die ich mit dieser Arbeit verbracht habe.

Mein sehr persönlicher Dank gilt meinen Eltern.

Meinen Freundinnen Swantje Middeldorff, Eva Henkel und Froschar Loewisch danke ich für Ihre Teilnahme und die besondere weibliche Einsicht in das Wesen der Dinge.

Heimo Fischer sage ich: Danke!

Diese Arbeit wurde von der Volkswagen Stiftung im Rahmen des Projektes EVA (Eintrag von Volatilen in die Atmosphäre) gefördert.